Study of Human Head Impact: Brain Tissue Constitutive Models

Toru Aida, B.S.M.E., M.S.M.E.

Dissertation Submitted to the
College of Engineering and Mineral Resources
at West Virginia University
in Partial Fulfillment of the Requirements
for the Degree of

Doctor of Philosophy
in
Mechanical Engineering

Dr. Victor H. Mucino, Chair
William O. Wray, Ph.D.
Ever Barbero, Ph.D.
Timothy L. Norman, Ph.D.
James E. Smith, Ph.D.
Charles F. Stanley, Ph.D.

Department of Mechanical and Aerospace Engineering

Morgantown, West Virginia

May 2000

Keywords: brain, constitutive, viscoelastic, finite element, head injury criteria
Copyright© 2000 Toru Aida

Abstract

Study of Human Head Impact: Brain Tissue Constitutive Models

Toru Aida

Finite element (FE) models of the human head have been used extensively to assess engineering response parameters (pressure, shear strain, etc.) that constitute the basis of various injury criteria including the Head Injury Criterion (HIC). There is a wide range of brain material properties reported in the literature, and linear elastic models are frequently used for the brain tissue which is viscoelastic in nature. The uncertainty around the properties of brain tissue affects the perceived importance of those response parameters under consideration.

In this research, the effect on head injury criteria of five reported viscoelastic brain models and their linear elastic alternatives is studied using both a simple spherical head model and a geometrically realistic head model. It is concluded that even the most proximate linear elastic model, which employs a Young's modulus equal to the short term modulus of the viscoelastic model, does not provide realistic representations of shear responses possibly associated with head injuries.

The calculated HIC value is found to be insensitive to the choice of brain material model, whether based on acceleration histories taken at the center of gravity or the side of the head, despite the fact that the shear strain histories in the brain vary drastically from model to model. Furthermore, on the basis of a hypothetical shear strain criterion for the threshold of tissue damage, the percentages of injured brain tissue predicted using different models vary greatly. The pressure response of all models is found to be virtually identical provided that the same bulk modulus (that of water) is employed. Parametric studies indicate that decreasing the bulk modulus leads to lower peak pressures and higher HIC values.

The fact that the widely varying internal responses associated with the various models considered in this study does not lead to variations in calculated HIC exposes the limitation of HIC. Therefore, HIC may not be a reliable indicator of actual internal dynamics and tissue damage. The FE method could be used to address this deficiency and provide guidance for the experimental determination of realistic constitutive models for brain tissue.

Acknowledgments

I would like to take this opportunity to express my sincere appreciation to my research advisor, Dr. Victor H. Mucino and supervisor at Los Alamos National Laboratory, Dr. William O. Wray for their support, motivation and most importantly, patience. Their guidance and encouragement is a large part in making all this possible.

I would also like to extend special appreciation to my committee members, Drs. Ever Barbero, Timothy L. Norman, James E. Smith and Charles F. Stanley. Not only have they been gracious enough to serve as my committee members, they also have been great supporters throughout my time as a student at West Virginia University.

Finally, my gratitude goes to my parents, Shiro and Masako Aida, for their enduring support in my academic pursuit.

The Visible Human Dataset™ is made available courtesy of the National Library of Medicine, Department of Health and Human Services.

Table of Contents

List of Figures

List of Tables

Chapter 1
Introduction

In the 1930s the crashworthiness of passenger vehicles was literally measured by how well vehicle structures could maintain their integrity under certain crash scenarios such as barrier impact and rollover. Today the focus of the passenger vehicle crashworthiness research has shifted from structural integrity to occupant mechanical responses. Injuries to the head and brain have received much attention due to their obvious importance and irreversible nature of injuries to the central nervous system, and attempts to quantify the injury potential to that particular region of a body have been extensive. Various postulations have been made to provide guidelines as to what type and level of external loads would produce head injuries. One criterion that is in wide-spread use today is the Head Injury Criterion (HIC) which is derived from the resultant acceleration history measured at the center of gravity of the head. Without regard to any other physical parameters, HIC's suitability as an injury potential indicator has been questioned by some. Still, HIC is accepted as one of the United States government's vehicle safety assessment criteria [61][1].

Meanwhile, various injury theories have been postulated in an attempt to associate observed head injuries to certain measurable parameters such as acceleration, pressure or shear strain in the brain. In order to gain better understandings of the internal dynamics of the human head under impact or impulse loading, mathematical models are often employed due to their ease of manipulability and data extraction. Particularly, the finite element method (FEM) has emerged as the most widely-used analysis tool. While FEM has been used in the area of structural analysis for years, it was not until the 1970s when the first finite element model of a human head was developed. Since then the complexity of the models in terms of geometry has progressively increased. However, material constitutive laws, especially that of the brain, has received less attention than it should have been. It is well regarded that all biological materials are assumed to be viscoelastic, or strain rate sensitive, but the majority of finite

[1]Numbers in square brackets indicate the references in Bibliography

element models developed so far employ linear elastic materials for the brain tissue. This is crucial since the rate-sensitive nature of those tissue materials most certainly affects the outcome from high-rate dynamic events such as automobile accidents.

1.1 Problem Statement

It is understandable that the linear elastic model is commonly used for the brain tissue since it is simple, easy to apply and familiar to most engineers. However, there are three main problems associated with this practice. First, the implications of such substitutions are not clear. It is widely-accepted knowledge that the brain tissue is a strain rate sensitive, or viscoelastic, material. It is not yet known whether or not using the linear elastic model for such a material is feasible, and if so, how such alternatives can be determined.

Second, even when a viscoelastic model is to be employed, there have been a number of brain material models published in the literature, and they differ greatly. They are undoubtedly different facets of the same material and correct in their own domains. It is naturally expected that different materials produce different results, but the clarification as to how different they are, and whether or not the differences in results are relevant, must be examined.

Third, with the material characteristics of the brain tissue still uncertain, there is a question as to how this uncertainty can affect head injury criteria. This is also part of a larger question of the applicability of the finite element method in the head injury research. When various dynamic events in the head are analyzed with a finite element model, the ability of the model to help predict head injury is, in turn, the ability to evaluate engineering parameters such as pressure and shear strain. Therefore, it must be known as to how the uncertainty in material properties can affect those output parameters, which injury criteria, including HIC, are affected more than others and which are insensitive to it.

1.2 Objectives

In order to examine of the applicability of the linear elastic model for a viscoelastic material, namely the brain tissue, first a review of viscoelasticity and literature survey on published viscoelastic brain models are conducted. As the same time, an implementation of a viscoelastic model in explicit nonlinear dynamics finite element code DYNA3D is validated.

A very simple model of a human head represented by a sphere is then tested with viscoelastic and possible linear elastic substitution models for the content (brain). Various responses such as pressure and shear strain are analyzed to make comparisons between different brain material models. The discrepancy or the lack thereof among those outcomes signifies the adequacy of such replacements.

Finally, a slightly more complex model of a human head is generated to examine various head injury criteria, including the Head Injury Criterion (HIC). The intent of this exercise is not to predict or make any assessment of head injury potentials. Rather, its main purpose is to study the sensitivity of the head injury criteria on brain material constitutive relations. This sensitivity study will suggest the degree of certainty in head injury criteria predicted by the current state of knowledge of the mechanical characteristics of the brain tissue. In particular, the effects on HIC, today's standard in head injury prediction measure, are studied.

1.3 Literature Review

1.3.1 Experiments

Studies on the material constitutive laws of mammalian brains first appeared in the 1950s, but some basic understanding of the brain tissue's characteristics such as high incompressibility was documented in the 1940s [33]. From the late 1960s to early 1970s a number of studies were conducted on the constitutive behavior of human brain tissue; one of the most comprehensive was performed at West Virginia University (WVU) [6]. On the basis of creep experiments Galford and McElhaney [19] reported the compressive compliance of human and monkey brains to be linear on semi-log scale. Their empirical expression for

compliance C in the human brain is $C = C_1 + C_2 \ln_e t$ (psi), $C_1 = 3.55 \times 10^{-1}$ and $C_2 = 2.60 \times 10^{-2}$. Additionally, relaxation experiments reported by Galford and McElhaney showed very rapid stress relaxation during the first 10 seconds after loading; the instantaneous relaxation for the human brain was determined to be approximately 0.95 pounds per square inch (psi) while the equilibrium relaxation modulus appeared to be nonzero. On the basis of axial free-vibration experiments, the dynamics modulus of the human brain was determined to be $9.68 + 3.80i$ (psi) at 34 Hertz (Hz). Shuck [75, 76] performed oscillatory shear experiments on cylindrical human brain samples up to 350 Hz. He found that the dynamic shear modulus varied with frequency, but yielding of the brain material appeared to have affected the results. Apparently, the onset of yielding in brain tissue is significantly affected by frequency or, equivalently, strain rate. It was difficult to determine from the data how much yielding had occurred in the material, especially in the high frequency range [75]. Shuck was able to conclude that there is little variation between gray and white matter in the brain, and that, for all practical purposes, the brain could be considered homogeneous. This point is reiterated by Estes [14], who reported only minor variation between samples that were predominantly white matter and those that were predominantly gray matter. His interpretation of the experimental data on the human brain in terms of the three-parameter viscoelastic solid model yielded the following parameters: $E_1 = 4.00$ psi, $E_2 = 1.89$ psi and $\eta_2 = 0.315$ lb.-sec./in^2, where the three-parameter solid was described as a combination of a Kelvin unit (E_2 and η_2), and a linear elastic unit (E_1) in series.

Non-human mammalian brains have been investigated by a number of researchers since [2, 5, 54, 73, 83], but only a handful of studies on the human brain or the central nervous system have been attempted. Bilston and Thibault [4] performed *in vitro* tension experiments on the human cervical spinal cord at various strain rates and fitted the data with a four-parameter viscoelastic models. The four parameter model is characterized by the following parameters: $E_1 = 0.65 \pm 0.36$ MPa, $E_2 = 10.6 \pm 8.2$ MPa, $\eta_1 = 119 \pm 49$ sec^{-1} and $\eta_2 = 15.0 \pm 13.1$ sec^{-1}. Donnelly and Medige [11], concerned that oscillatory experiments such as those done by Shuck [75] may damage the tissue, elected to conduct parallel-plate shear experiments on human brain tissue at different strain rates. Specimens were deformed to the maximum engineering strain of 1 (45 degrees deformation angle) by using an impact loading device. The data were fit with a three-parameter linear viscoelastic solid model: the associated model parameters are: $\alpha_1 = 550$ Pa, $\alpha_2 = 291$ Pa and $\xi = 9.4$ Pa-s for the brain in shear, where α_2

and ξ define the Kelvin unit and α_1, the linear elastic unit in series.

1.3.2 Finite Element Models

In the past fifty years numerous attempts have been made to mathematically model a human head, particularly using the finite element method. King and Chou [41] presented a review of mathematical models of the human head developed between 1966 and 1974, and more recent review was presented by Hardy *et al.* [31]. The models so far developed can be grouped in two basic categories; analytical and numerical. Analytical models tend to be simplified in order to obtain closed-form or exact solutions to the problem. Examples of analytical models include one dimensional models such as ones developed by Kopecky and Ripperger [43] where the main focus was to analyze pressure variation along the direction of impact, or fluid-filled spherical rigid/elastic shell models such as the ones by Engin [13] and Chan and Liu [7], or a spheroidal model such as the one proposed by Talhouni and DiMaggio [81]. However, as King and Chou [41] and Dawson *et al.* [9] pointed out, it is questionable that those overly simplified models have much relevance in solving head injury mechanism problems.

On the other hand, numerical models such as finite element models have advantages over analytical ones in terms of flexibility and expandability to accommodate complex geometry, though some of the early models have been quite simple. Kenner and Goldsmith [36] used a finite element model of an axisymmetric elastic shell filled with a compressible, inviscid fluid to compare the results from their analytical solution and experiments with good agreement. The model developed by Khalil *et al.* [38] was similar to the one in [36], but their axisymmetric model was used to analyze a head-helmet system, and the bone (skull) was modeled using a viscoelastic material. Once again the finite element solutions were compared against their experiments. Shugar and Katona [76] developed an axisymmetric, plane strain and three-dimensional models of a human head, the first two of which have been used to analyze dynamic responses for a time-varying pressure load. All models had distinctive three layers of the skull (outer/inner table and diploë). The brain was modeled as an inviscid compressible fluid, later replaced by linear elastic and viscoelastic materials. In the three dimensional model, the subarachnoidal space which was filled with cerebrospinal fluid (CSF) was explicitly modeled as well. Validation was made only for the axisymmetric

model by comparing a coup pressure history with finite difference solutions; no other attempts to verify other models were made. The intracranial pressure distribution, skull displacement and influences of difference material representations were analyzed. The three-dimensional model was prepared for discretization only. Another attempt to model a human head through axisymmetric representation was made by Khalil and Hubbard [39], who developed three different models; a spherical model with a single-layered skull, an oval model with two spherical caps with a single-layered skull and a spherical model with a three-layered skull. Materials used in the models were linear elastic, and the brain was simulated as a compressible inviscid fluid, with a density and bulk modulus of water. Head injuries were categorized in three different groups; scalp, skull and brain injuries. Skull injuries were interpreted as failure of the cranial bones, which corresponded to 0.5 percent strain in tension and 1.5 percent strain in compression. The cause of brain injuries was attributed to cavitation which was assumed to take place when the fluid pressure was reduced by 1 atmosphere.

Ward and Thompson [87] generated one of the first detailed three dimensional brain models based on the “actual” geometry of the head, which incorporated the cerebrum, cerebellum, dura (including falx cerebri, tentorium cerebelli), ventricles and brain stem. The cerebrum and cerebellum were modeled as elastic solid materials, while the dura, falx cerebri and tentorium cerebelli were modeled using membrane elements with linear elastic material properties. The lateral and third ventricles were approximated by reducing the elastic modulus of the surrounding areas (labeled as “composite material”), and the forth ventricle was simulated as a soft elastic solid. The last assumption was an attempt to simulate the release mechanism facilitated by the foramen magnum through which CSF escapes under pressure, even though CSF in vitro exhibits high incompressibility [34]. The skull was not included in their model; instead, special boundary elements were incorporated in order to simulate the interaction between the brain and skull. While only the static and modal analyses were performed on this model, subsequent revisions of this model by Nahum *et al.* [57] and Ward *et al.* [87] were used to analyze transient dynamic responses of the brain whose results, primarily in the form of intracranial pressure histories, were compared with those from experiments using human cadavers and primates. Nahum *et al.* found a high damping ratio of the brain and a correlation between maximum intracranial pressure and acceleration in the brain. Ward *et al.* proposed intracranial pressure as a brain injury criterion based on empirical observations which showed that intracranial pressure above 34 psi could

produce brain contusions. This magnitude of intracranial pressure was correlated to the magnitude and duration of an input acceleration pulse to the brain. By varying the pulse magnitude, the brain pressure tolerance (BPT) curves were generated. Comparisons of the BPT criterion against other injury criteria such as Wayne State Tolerance (WST) curve, Viena model injury criteria, maximum strain criterion (MSC) and head injury criterion (HIC) were made, which showed a relatively good agreement between the BPT and HIC.

Another model with similar complexity was developed by Hosey and Liu [34]. Their model contained the cerebrum, cerebellum, skull, dura, CSF layer, spinal cord, vertebrae and intervertebral disks. An effort was made to match the initial inertial characteristics of the brain with experimental data by adding point masses at various locations on the brain surface. Mid-sagittal symmetry was assumed, and the model was further simplified by utilizing thin shell elements in portions of the skull. Materials were presumably isotropic linear elastic, and the brain and CSF were assigned a Poisson's ratio of 0.499, thus simulating near incompressibility. An occipital pressure pulse was applied, and the resulting intracranial pressure histories were analyzed.

Ruan *et al.* [69] developed three models in order to investigate feasibility of the finite element method, to analyze influence of interior membranes (meninges) and variations in material properties. The first model was an axisymmetric, single-layered shell filled with an inviscid fluid in order to reproduce the results from Khalil and Hubbard [39] in an attempt to prove the feasibility of the finite element method. The second and third models were two-dimensional plane-strain bilaterally symmetric models in the coronal section, passing through 10 millimeters posterior to the auditory canal. The external geometry was taken from an actual anatomical data, and the skull was assumed to be a single-layered structure. The weight of this section was assumed to be 71 percent of the actual mass of an adult-size human head. The second model consisted of a single-layered skull and an inviscid fluid as the intracranial contents, while the third model included the CSF layer, falx cerebri and tentorium. The brain in the third model was also modeled an inviscid fluid. Tissue materials in all three models were assumed to be linear elastic, homogeneous and isotropic. Comparisons between the second and the third model revealed that the presence of the membranes affected the intracranial pressure distributions. Parametric study on material properties was performed using the second and third models, and their effects on pressure responses were analyzed. It was found that the Young's modulus of the membrane, bulk

modulus of fluid and the Young's modulus of the shell (skull) all had effects on intracranial pressure distribution and magnitudes.

Another plane strain model was developed by Chu *et al.* [8], which was a parasagittal section of a human head from anatomical and anthropometric data. The rationale for the selection of the parasagittal plane approximately 3.5 centimeters off the midsagittal plane was based on a clinical fact that cerebral contusions would not normally occur in the midsagittal plane. Most of features in the cranium were omitted, leaving only the skull and brain as explicit components. The elastic modulus of the brain, however, was chosen to be higher than the average to compensate the lack of the meninges in the model. The foramen magnum was modeled by detaching the brain from the skull near the bottom of the brain thus creating approximately 1.5 centimeters wide "opening" which contributed to a 15 percent reduction in the contracoup pressure. Though only the occipital pressure was used for validation of the model, their results and clinical observations seemed to indicate that cerebral contusions were caused by shear strain in the brain.

One of the most complex and detailed models of a human head was developed by Ruan *et al.* [70, 70, 71]. Their model had realistic exterior geometry which included a certain degree of facial representation in addition to the cranium. It also had explicit cerebral hemispheres and the falx cerebri separating each other, along with a dura mater surrounding the entire brain. This model was used to analyze coup, contracoup pressure, shear strain and acceleration under various impact conditions using an impactor at various speed, weight and location. The authors concluded that HIC was a reasonable indicator of impact severity, based on correlations between HIC and other engineering parameters such as coup pressure, maximum shear stress and von Mises stress in the skull.

1.3.3 Material Constitutive Characterizations

Investigators, in the course of developing finite element models of the head, have incorporated their own constitutive models based on what they considered to be reasonable assumptions and/or on data from the experimental studies reported in the preceding section. Khalil *et al.* [38] assumed the brain to be an inviscid fluid with a bulk modulus of 2.07×10^9 Pa. Khalil and Hubbard's axisymmetric models reported in 1977 [39] explicitly used water to represent the brain; the water was represented as an inviscid fluid with a bulk modulus of

2.19×10^9 Pa.

A model developed by Ward *et al.* [87, 87] employed a linear elastic material model for the brain whose properties were derived from [19] and Barber *et al.* [3]. Similarly, Hosey and Liu [34] adopted the material property values from McElhaney *et al.* [50] for their linear elastic brain model. These models all employ a linear elastic law that is defined by $E = 6.67 \times 10^4$ Pa and $\nu = 0.48$, the former of which is the storage modulus in the vibration experiment reported in [19] and [50]. The same material characterization was used in the models reported by Ruan *et al.* in 1991 [69].

Chu *et al.* [8] also elected to use the linear elastic model for the brain derived from Khalil and Viano [40] and Lee *et al.* [44]. Khalil and Viano's investigation on the brain material properties was done using $E = 66.7 \times 10^3$ Pa, the same value used by [34, 69, 87, 87], while the Poisson's ratio was varied from 0.45 to 0.49999. The model investigated by Lee *et al.* was that of the Rhesus monkey, and their complex shear modulus for the brain was reported to be $80 + 16i$ kPa with the Poisson's ratio of 0.49. The actual parameters used by Chu *et al.*, however, are $E = 25 \times 10^4$ Pa and $\nu = 0.49$.

Ruan *et al.* developed a three-dimensional head model in 1994 [71] that employed a linear elastic brain with material properties based on their own previous work [69]. Values for bulk and shear moduli (2.19×10^9 and 1.68×10^6 Pa, respectively) and Poisson's ratio (0.4996) are reported. Young's moduli calculated from bulk modulus and Poisson's ratio is 5.26×10^6 and from shear modulus and Poisson's ratio, 5.06×10^6 Pa, both of which are substantially higher than any models reported elsewhere.

Ruan *et al.* also reported a linear viscoelastic representation of the brain tissue [70, 70] based on the data of Galford and McElhaney [19]. Their three-parameter linear viscoelastic model was characterized by short-term and long-term shear moduli of 5.25×10^5 Pa and 1.68×10^5, Pa respectively, and decay constant of 35 sec^{-1}. It is not clear which experimental results were used to extract these parameters. Further, in [44] predictions of coup and contracoup pressures resulting from viscoelastic and elastic material representations were compared; on that basis, the authors concluded that the viscoelastic effect was insignificant. The substitute elastic properties used for this were not reported.

Other viscoelastic models reported by Estes [14], who performed compression tests, and

Donnelly and Medige [11], who performed parallel-plate dynamic shear tests on brain samples, are discussed in details in a subsequent Chapter.

A summary of material properties reported in the literature is presented in Table 1.1.

Table 1.1 Material Representation Schemes and Parameters

Investigators	*Brain Constitutive Law and Parameters*	*Sources and comments*
Khalil *et al.* [38]	Inviscid Fluid: $K = 2.07 \times 10^9$ Pa $\rho = 1.05 \times 10^3$ kg/m^3	Water?
Ward and Thompson [87]	Linear Elastic: $E = 6.67 \times 10^4$ Pa* $\nu = 0.48$ $\rho = 1.04 \times 10^3$ kg/m^3	From WVU Final Report [6] (*Later revisions such as [57] used this value which is the storage modulus from the vibration experiment). Density from Barber *et al.* [3]
Khalil and Hubbard [39]	Inviscid Fluid: $K = 21.9 \times 10^8$ Pa $\rho = 1.01 \times 10^3$ kg/m^3	Water.
Hosey and Liu [34]	Linear Elastic: $E = 6.67 \times 10^4$ Pa $\nu = 0.48$ $\rho = 1.04 \times 10^3$ kg/m^3	The storage modulus of the vibration experiment by Galford and McElhaney [19] is used as Young's modulus.
Ruan *et al.* [69]	Linear Elastic: $E = 6.67 \times 10^4$ Pa $\nu = 0.48$ $\rho = 1.04 \times 10^3$ kg/m^3	Same as Hosey and Liu above.
Chu *et al.* [8]	Linear Elastic: $E = 25 \times 10^4$ Pa $\nu = 0.49$ $\rho = 1.00 \times 10^3$ kg/m^3	Khalil and Viano [40] and Lee *et al.* [44]. [40] used 66.7 kPa as their choice of E, the latter reported the dynamic shear modulus of $80 + 16i$ kPa for primate brain.
Ruan *et al.* [71]	Linear Elastic: $E = 5.06 \times 10^6$ Pa* $E = 5.26 \times 10^6$ Pa† $\nu = 0.4996$ $\rho = 1.04 \times 10^3$ kg/m^3	Based on their previous study [69] and Shugar [78], whose data are based on Goldsmith [23], who in turn extracted data from Galford and McElhaney [19]. (* $G = 1.68 \times 10^6$ Pa, $\nu = 0.4996$) († $K = 2.19 \times 10^9$ Pa, $\nu = 0.4996$)
Ruan *et al.* [70, 70]	Linear Viscoelastic: $G(t) = G_\infty + (G_0 - G_\infty)e^{-bt}$ $G_0 = 5.28 \times 10^5$ Pa $G_\infty = 1.68 \times 10^5$ Pa $b = 0.035$* $K = 1.28 \times 10^8$ Pa†	Data published by Galford and McElhaney [19]. It is unknown which experimental data is used to derive the parameters. (* time in milliseconds) († $E = 1.68 \times 10^6$ Pa, $\nu = 0.4996$)

1.3.4 Injury Mechanisms

It must be noted that the phrase, "injury mechanisms" seems to be poorly defined in the literature. It is assumed that the phrase refers to mechanical causes which inflict particular types of head injuries. Clinically observable injuries such as the ones described in the previous section are, "…caused by deformation of biological tissues beyond their recoverable limit" [85] which can be defined as the tissues' failure strength. In other words, biomechanical nature of injuries is strain; and the type, magnitude and distribution pattern of strains determine the types and levels, or severity of resulting injuries, or more loosely, the "failure" of tissues results in injuries. Failure in conventional engineering materials such as metal is usually defined in terms of stress and strain in a region of a body, and the same applies to the biological systems as well. However, "failure" in such cases can be defined as an anatomical structural breakage observable through visual inspection or certain scanning methods, such as computerized tomography (CT) scan, magnetic resonance imaging (MRI) or positron emission tomography (PET) scan, or as a physiologic dysfunction which can occur in the nervous system before any structural damage is observed [18, 65]. To complicate things further, a set of events that eventually leads to head injuries can be interpreted from different angles. In other words, one postulated injury mechanism theory can contain common components shared with others, leaving gray areas between different injury mechanism theories. With this in mind, however, a categorization scheme which seems to be widely accepted will be used to differentiate popular injury mechanisms [9, 31]. They are; negative pressure theories, positive pressure theories, pressure gradients theories and rotational theories. It will be seen that shear strain is suggested as an underlying cause for many postulations.

Negative pressure theories attribute negative, or tensile pressure and subsequent phenomena such as cavitation as causes of head injuries. This idea has been used to explain contracoup injuries by Denny-Brown and Russell [10], later more extensively by Gross [26] and speculated by Gurdjian *et al.* [28]. In Denny-Brown and Russell's experiments the main focus was on concussion inflicted on animals whose heads were free to move when struck by a pendulum, and contracoup injuries were relatively uncommon. However, when they did occur, they were of focal type in nature, and based on their own observations and results from other researchers it was speculated that inertial lag of the brain caused a "momentary vacuum" in the opposite region of the head to the striking point. It was also noted that

contracoup injuries were not present when the head was fixed therefore not allowed to move. This aspect will be discussed in rotational theories. Gross suggested that both contracoup and coup lesions could be explained by the cavitation theory. In this theory the contracoup lesions, particularly the petechial hemorrhages or conic-shaped contusion, were caused by cavitation in the fluid when the negative (tensile) pressure in the fluid due to acceleration was sufficient to produce tensile failure of the fluid. Gross believed that violent impacting forces could cause those lesions as the cavities collapsed. The formation on cavities due to low pressure in fluids and their effects as they collapse are well known in hydromachinary such as ships' propellers where low pressure, accompanying cavities and their collapse in the trailing edge cause the metal propellers to erode; the process known as cavitation erosion. The following hypothesis was added for relatively infrequent occurrences of the contracoup lesions in the posterior region when the head was struck in the front; right before the frontal region of the head was struck, it might be possible that the head was tilted forward slightly, lowering the contracoup region to near the foramen magnum. Then the flow of the cerebrospinal fluid (CSF) through the foramen magnum into the contracoup region might attenuate the tensile pressure, thus preventing cavitation from forming. A similar theory was postulated for the coup lesions, in which the elasticity of the skull presumably caused a temporarily depressed area to recover rapidly to the original shape, thus creating a local low pressure area. In addition to those focal types of injuries, the theory was further expanded to explain diffuse brain damage by considering the resonance effect. In this hypothesis the resonance caused in the brain (in experiments, a flask or tube) produced volumetric pulsation. If the magnitude of oscillation was sufficiently high, disperse cavitation occurred on the expanding phase of the cycle. In order to explain concussion based on the cavitation theory, the author suggested another well-known phenomenon in the cavitation research field called sonoluminescence. This term refers to a phenomenon where liquids exhibit luminescence associated with electrical discharge when they are under the effect of ultrasonic wave. It was speculated that this type of weak electrical discharge might be responsible for concussion.

Lindenburg is probably the most prominent supporter of positive pressure theories. Similarly to Gross, Lindenburg and Freytag [45] attempted to explain every type of head injuries by positive pressure theories. Clinical observations indicated that contracoup injuries were rare and the dominant lesions were in the coup region in cases where a blow was applied to a stationary, but movable head, and that the opposite happened in cases where a moving head

hit a stationary target as in a fall; that is, the contracoup injuries were dominant and coup injuries were rare. In case of a blow to a stationary movable head, they postulated that the skull deformation due to the blow introduced compressive pressure at the site of impact, in conjunction with compression pressure on the coup site caused by the brain lagging the motion of the skull. In the same situation compressive pressure transferred to the contracoup side was sometimes responsible for rare contracoup injuries, but for most part this compressive pressure was canceled by negative pressure caused by the same lagging effect of the brain with respect to the skull as the head moved. Their postulation on falls was that in such situations the brain lagged the skull, generating negative pressure in the soon-to-be coup site, and due to a relatively long duration of falls, the cerebrospinal fluid accumulated on that side of the head, thus creating a thicker buffer against impact. On the other hand, on the soon-to-be contracoup side the CSF layer was thinner due to the brain's inertia. Similarly to the case of a blow, impact of the head against a target depressed the skull and increased intracranial pressure; this compressive pressure was, as it was implied, instantaneously transferred to the contracoup side where the CSF buffer was thinner, thus causing injuries on this particular region. The brain lag in a fall was discussed in details by Dawson *et al.* [9] who also suggested that compressive pressure was responsible for contracoup injuries in a fall and coup injuries from a blow to the head. However, Dawson *et al.*'s conclusion was that compressive pressure on the thin protective CSF layer produced a nonuniform pressure distribution on the brain, thus generating shear strain which ultimately caused damages.

The next two groups of theories seem to share the same fundamental mechanism; shear strains. Gurdjian *et al.* [28] made a statement that concussion involved the upper brain stem, and that the increase in intracranial pressure which in turn produced pressure gradients at the craniospinal junction where the brainstem was located, could be one of the main causes. Later, Gurdjian and Lissner [27] performed experiments using a photoelastic method where a one-inch thick plastic sagittal section of the head with a foramen magnum opening through which the content was allowed to escape. The model was filled with a milling yellow solution which would change refractivity under shear strain. In their study a pressure pulse applied to the walls of the model induced shear strains in the craniospinal junction. Their conclusion was that those shear strains were caused by pressure gradients in that region as a result of increased simulated intracranial pressure, supporting their previous statement. However, finite element models with the simulated foramen magnum such as the ones developed by Chou *et al.* [8] and Ruan *et al.* [71] failed to show significant pressure gradient

around the craniospinal junction, even though high shear strains in that region were observed in Chou *et al.*'s model.

The rotation theory was discussed in details by Holbourn [33], who suggested that, owing to the brain's high bulk modulus and low modulus of rigidity, the brain could only be injured by the presence of shear strain. Based on this observation, he concluded that only rotational motion could produce substantial shear strain in the brain to cause "injuries". He developed a simulated physical model of a brain with gelatin and confirmed the presence of high shear strain in areas where hemorrhages were observed, though he disclaimed that there was no indication what type of injuries could be induced in high-shear strain areas. The concept that rotational motion causing brain injuries was supported in the case of concussions by a series of impact experiments on cats, dogs and monkeys which had been performed by Denny-Brown and Russell in 1941 [10] who found that it was easier to induce concussion when the head was free to move (that is, rotate). This finding has been supported by [64]. Denny-Brown and Russell also found that velocity of the striking object was not relevant since similar levels of striking velocities were required to induce concussion to animals with greatly different head sizes. Instead, they postulated that the rate of change in velocity, *i.e.* acceleration was the crucial factor. The authors made a clear distinction between acceleration concussion and compression concussion, the former of which was caused when a sufficiently high acceleration was applied to the head, while the latter referred to cases where the head was supported by a hard surface thus not allowed to rotate while the head was struck. Acceleration concussion was not accompanied by significant intracranial pressure increase. On the other hand, a great increase in intracranial pressure was observed when compression concussion was induced. Though not one of the main focuses of the study, they also found that the contracoup injury could only be induced when the head was allowed to rotate (see the negative pressure theory paragraph above).

Concentrating mainly on concussion, Ommaya [64] introduced the centripetal theory which stated that the more severe degrees of concussion were produced as shear strains which would cause functional and structural disturbance on the neural tissues, progressed from the outer surface of the brain towards the center. Even though no particular loading conditions were explicitly specified in the theory, in their previous works [63] it was speculated that rotational motion was the primary cause of diffuse injuries with other secondary factors such as the nature of loading (impact versus impulsive) affecting the outcome. They also indicated

that in their translation-only, non-impact (impulsive) experiments, diffuse type of injuries could not be obtained unless rotational components have been added. Only the focal type of injuries were produced in such experiments, and the authors further noted that those focal type injuries differed from those observed in their impact experiments, which suggested cavitation as the cause of injuries.

Rotational, or shear strain as the subsequent event, theories were implied and applied for experimentally-induced acute subdural hematomas (ASDH) by Gennarelli and Thibault [22] and numerical analyses were performed to support the theories by Lee *et al.* [44]. Since the most common source of ASDH is the rupture of bridging veins as it connects the brain surface and dural sinuses in the subdural space [22], Lee *et al.* focused their analysis on tearing of such veins due to the relative motion between the brain and rigid skull during rotational acceleration and deceleration phases. Similarly Chou *et al.* [8] performed numerical analyses on cerebral contusions. Their model is a parasagittal plane-strain model subjected to rotation by an imposed displacement history. By comparing their numerical results and clinical observation, they concluded that cerebral contusions were caused by shear strain.

Table 1.2 Types of Injuries and Postulated Injury Mechanisms

Investigators	*Postulated cause of injuries/injury mechanisms*
Denny-Brown and Russell [10]	• Rotational acceleration (acceleration concussion). • Intracranial pressure irrelevant for this type of concussion. • Contracoup injury due to negative pressure (“momentary vacuum”).
Holbourn [33]	• Shear strain caused by rotation of the head (shear strain due to rotational acceleration).
Gurdjian *et al.* [28, 29]	• Concussion involves upper brain stem—due to intracranial pressure gradient and resulting shear strain in the area. • Intracranial pressure could be relevant—with pressure gradient around the brainstem producing shear strain. • Acceleration alone not indicative.
Gross [26]	• Cavitation due to high tensile stress, sonoluminescence.
Ommaya and Gennarelli [63]	• Focal lesion due to pure translation, no concussion. • Diffuse type of injury only inducible with the addition of rotation; added rotation to induce the same tangential acceleration as the pure translation easily producing concussion.
Lindenburg and Freytag [45]	• Positive pressure—both coup and contracoup.
Dawson *et al.* [9]	• Shear stress (though based on compressive pressure).
Ommaya [64]	• Contusions due to translational acceleration (no contact) may be caused by cavitation. • Centripetal theory on concussion.

1.3.5 Head Injury Criteria

Goldsmith and Ommaya [24] cites the EEC (European Economic Community) Biomechanics program for the definition of injury criteria. That is, “(The term ‘injury criterion’ or ‘injury criteria’) denotes a physical parameter which correlates well with the injury severity of the body region under consideration.” Therefore, the term “head injury criteria” refers to physical parameters that correlate with the injury severity in the head. As seen in the previous section, those physical parameters that are proposed for this purpose include shear strain, pressure (both positive and negative) and acceleration. The Head Injury Criterion (HIC) which is derived from the resultant acceleration history at the center of the gravity of the head, is the most widely used criterion for head injuries.

The evolution of HIC is well documented [24, 32, 55], and its history is summarized from these references. HIC's origin traces to the Wayne State Tolerance Curve (WSTC) which was a curve initially generated by six data points relating acceleration level and duration that produced linear skull fracture in embalmed cadaver heads. This concept was expanded and refined in 1966 by Gadd to form the Gadd Severity Index (GSI or SI). Versace in 1971 critiqued SI and proposed what would turn out to be the current mathematical form of HIC with the following expression:

$$\mathrm{HIC} = \max_{t_1, t_2} \left\{ (t_2 - t_1) \left[\frac{1}{(t_2 - t_1)} \int_{t_1}^{t_2} a(t) dt \right]^{2.5} \right\}$$

where $a(t)$ is the resultant acceleration history and t_1 and t_2 are two points in time which would maximize the HIC value. The threshold value of HIC (currently 1000) for head injuries, the maximum time interval $(t_2 - t_1)$ (currently 36 milliseconds) and even the applicability of HIC itself as a head injury indicator are being questioned.

However, as mentioned previously, Ward *et al.* [87] found a relatively good agreement between their brain pressure tolerance (BPT) and HIC. In addition, Ruan *et al.* [70]'s parametric study with a finite element model of a head where loading conditions were changed by altering the mass and velocity of the impactor, showed that HIC corresponded with maximum shear strain, coup and contracoup pressure and head acceleration, thus suggesting the suitability of HIC as a general head injury indicator.

Prasad and Mertz [68], under the assumption that there is a correlation between HIC and observed head injuries, used data from cadaver experiments to generate a risk factor curve based on HIC. "Head injuries" were defined as either the presence of skull fracture or artery rupture in the brain. They employed the Mertz/Weber method of constructing a cumulative head injury distribution curve to use HIC as a head injury potential indicator. Using this method, HIC value of 1500 was found to correspond to 56% chance of head injury, compared with 16% at HIC of 1000. This method of using HIC as a risk indicator was further expanded in [53] and it was used for airbag effectiveness assessment in [67].

On the other hand, other researchers are pursuing other injury criteria based on the arguments that HIC was not injury-specific and that it did not correlate to injury severity. This trend is

represented recently by Margulies and Thibault [47], who conducted a wide range of experimental and analytical studies on diffuse axonal injury (DAI) using both the baboon and human forms. They proposed a new criterion and tolerance for DAI in terms of the peak angular acceleration and the peak change in angular velocity of the head. Shear strains were assumed to be a measure of tissue response and thus injuries, and used to predict DAI in humans based on the baboon experiments.

Chapter 2
Engineering Background

2.1 Linear Viscoelasticity

The term viscoelasticity originates from simple mechanical models consisting of springs and dashpots which characterize elasticity and viscosity, respectively, to define the load-deflection relationship of a certain group of materials. Such materials are known to exhibit responses that are time-dependent, unlike the simple linear elastic material whose stresses depend only on the instantaneous state of strain, or vice versa. There are a number of simple spring-dashpot (linear elastic and linear viscous units, respectively) models such as the Maxwell fluid (a spring and a dashpot in series), the Kelvin or Voigt solid (a spring and a dashpot in parallel) and any combinations of such models. In this study, the three-parameter solid constitutive model is employed because it is relatively simple, but provides a finite, non-zero relaxation modulus at equilibrium. This characteristic is essential for fitting the data reported by Galford and McElhaney [19].

The three-parameter solid viscoelastic model can be represented as a combination of a Kelvin solid unit and a linear elastic unit in series (see Figure 2.1).

In order to obtain the stress-strain relationship, the derivation is an extension of what is found in Flügge [15]; first apply stress σ on both ends, and the total strain across the model ε is

$$\varepsilon = \varepsilon_1 + \varepsilon_2 \qquad (2\text{-}1)$$

where ε_1 and ε_2 are strains in the spring and the Kelvin unit, respectively.

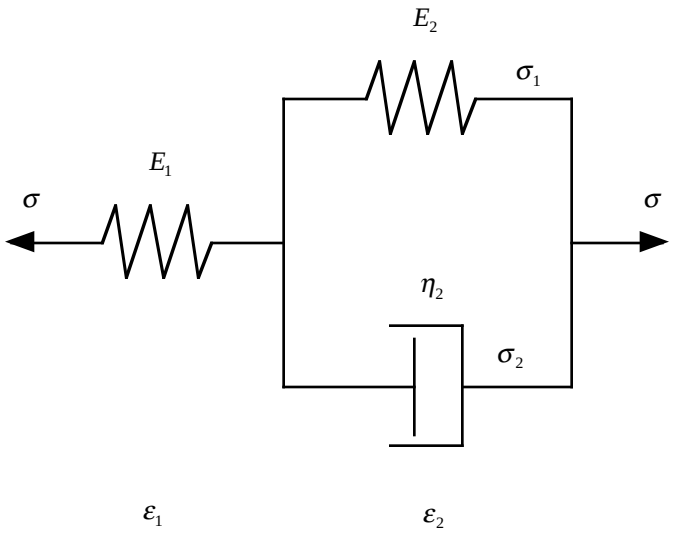

Figure 2.1 Three-Parameter Viscoelastic Solid Model

It follows that

$$\sigma = E_1 \varepsilon_1. \tag{2-2}$$

Within the Kelvin unit,

$$\sigma_1 = E_2 \varepsilon_2 \tag{2-3}$$

and

$$\sigma_2 = \eta_2 \frac{d\varepsilon_2}{dt} \tag{2-4}$$

which are related by

$$\sigma = \sigma_1 + \sigma_2$$

or

$$\sigma = E_2\varepsilon_2 + \eta_2 \frac{d\varepsilon_2}{dt} \tag{2-5}$$

where σ_1 and σ_2 are stresses in the spring and dashpot of the Kelvin unit, respectively. Differentiate (2-2) once and substitute along with (2-5) into the first temporal-derivative of (2-1) to form

$$\frac{d\varepsilon}{dt} = \frac{1}{E_1}\frac{d\sigma}{dt} + \frac{\sigma - E_2\varepsilon_2}{\eta_2}. \tag{2-6}$$

From (2-1), combined with (2-2), ε_2 can be written as

$$\varepsilon_2 = \varepsilon - \frac{\sigma}{E_1}. \tag{2-7}$$

Substituting this into (2-6),

$$\frac{d\varepsilon}{dt} = \frac{1}{E_1}\frac{d\sigma}{dt} + \frac{\sigma}{\eta_2} - \frac{E_2}{\eta_2}\left(\varepsilon - \frac{\sigma}{E_1}\right). \tag{2-8}$$

Collecting terms,

$$\sigma + \frac{\eta_2}{E_1 + E_2}\frac{d\sigma}{dt} = \frac{E_1E_2}{E_1 + E_2}\varepsilon + \frac{E_1\eta_2}{E_1 + E_2}\frac{d\varepsilon}{dt}. \tag{2-9}$$

Equation (2-9) has the form

$$\sigma + p_1\frac{d\sigma}{dt} = q_0\varepsilon + q_1\frac{d\varepsilon}{dt} \tag{2-10}$$

where

$$p_1 = \frac{\eta_2}{E_1 + E_2} \tag{2-11a}$$

$$q_0 = \frac{E_1 E_2}{E_1 + E_2} \tag{2-11b}$$

$$q_1 = \frac{E_1 \eta_2}{E_1 + E_2} \tag{2-11c}$$

or rearrange to express E_1, E_2 and η_2 in terms of p_1, q_0 and q_1

$$E_1 = \frac{q_1}{p_1} \tag{2-12a}$$

$$E_2 = \frac{q_0 q_1}{q_1 - p_1 q_0} \tag{2-12b}$$

$$\eta_2 = \frac{{q_1}^2}{q_1 - p_1 q_0}. \tag{2-12c}$$

The coefficients p_1, q_0 and q_1 in (2-10) describe the one-dimensional stress-strain relationship of the three-parameter viscoelastic model. Now it is necessary to expand the discussion to three dimensions. The following derivation is an extension of an example found in Flügge [15].

When the momentum equilibrium is maintained, the stress tensor is symmetric and expressed by;

$$\begin{bmatrix} \sigma_{xx} & \sigma_{xy} & \sigma_{xz} \\ \sigma_{xy} & \sigma_{yy} & \sigma_{yz} \\ \sigma_{xz} & \sigma_{yz} & \sigma_{zz} \end{bmatrix} \tag{2-13}$$

and can be split into the spherical or hydrostatic and deviatoric parts, so that

$$\begin{bmatrix} \sigma_{xx} & \sigma_{xy} & \sigma_{xz} \\ \sigma_{xy} & \sigma_{yy} & \sigma_{yz} \\ \sigma_{xz} & \sigma_{yz} & \sigma_{zz} \end{bmatrix} = \begin{bmatrix} \sigma_M & 0 & 0 \\ 0 & \sigma_M & 0 \\ 0 & 0 & \sigma_M \end{bmatrix} + \begin{bmatrix} S_{xx} & S_{xy} & S_{xz} \\ S_{xy} & S_{yy} & S_{yz} \\ S_{xz} & S_{yz} & S_{zz} \end{bmatrix} \tag{2-14}$$

where the mean normal stress is defined by

$$\sigma_M = \tfrac{1}{3}\left(\sigma_{xx} + \sigma_{yy} + \sigma_{zz}\right) \tag{2-15}$$

hence

$$S_{xx} + S_{yy} + S_{zz} = 0\,. \tag{2-16}$$

The spherical stresses represent only the volumetric change or dilatation while the deviatoric stresses, shear deformation. The latter statement can be clarified by decomposing the second matrix of equation (2-14)

$$\begin{bmatrix} S_{xx} & S_{xy} & S_{xz} \\ S_{xy} & S_{yy} & S_{yz} \\ S_{xz} & S_{yz} & S_{zz} \end{bmatrix} = \begin{bmatrix} 0 & S_{xy} & 0 \\ S_{xy} & 0 & 0 \\ 0 & 0 & 0 \end{bmatrix} + \begin{bmatrix} 0 & 0 & 0 \\ 0 & 0 & S_{yz} \\ 0 & S_{yz} & 0 \end{bmatrix} + \begin{bmatrix} 0 & 0 & S_{xz} \\ 0 & 0 & 0 \\ S_{xz} & 0 & 0 \end{bmatrix} + \begin{bmatrix} S_{xx} & 0 & 0 \\ 0 & -S_{xx} & 0 \\ 0 & 0 & 0 \end{bmatrix} + \begin{bmatrix} 0 & 0 & 0 \\ 0 & -S_{zz} & 0 \\ 0 & 0 & S_{zz} \end{bmatrix} \tag{2-17}$$

The forth term (and fifth in a similar fashion) represents a state of stresses that can be represented as a pure shear state in a rotated reference plane, which is easily shown using the Mohr's circle.

A similar decomposition can be made for strains by using the tensorial notation of strains,

$$\begin{bmatrix} \varepsilon_{xx} & \varepsilon_{xy} & \varepsilon_{xz} \\ \varepsilon_{xy} & \varepsilon_{yy} & \varepsilon_{yz} \\ \varepsilon_{xz} & \varepsilon_{yz} & \varepsilon_{zz} \end{bmatrix} = \begin{bmatrix} \varepsilon_M & 0 & 0 \\ 0 & \varepsilon_M & 0 \\ 0 & 0 & \varepsilon_M \end{bmatrix} + \begin{bmatrix} \eta_{xx} & \eta_{xy} & \eta_{xz} \\ \eta_{xy} & \eta_{yy} & \eta_{yz} \\ \eta_{xz} & \eta_{yz} & \eta_{zz} \end{bmatrix} \tag{2-18}$$

where the mean normal strain is defined by

$$\varepsilon_M = \tfrac{1}{3}\left(\varepsilon_{xx} + \varepsilon_{yy} + \varepsilon_{zz}\right) \tag{2-19}$$

hence

$$\eta_{xx} + \eta_{yy} + \eta_{zz} = 0. \tag{2-20}$$

In isotropic materials hydrostatic stresses produce only a dilatation and no distortion. Therefore hydrostatic stresses and hydrostatic strains in viscoelastic materials are related by the standard viscoelastic law, which is a general form of (2-10),

$$\sum_{k=0}^{m''} p_k'' \frac{\partial^k \sigma_M}{\partial t^k} = \sum_{k=0}^{n''} q_k'' \frac{\partial^k \varepsilon_M}{\partial t^k} \tag{2-21}$$

or

$$\mathbf{P}''\sigma_M = \mathbf{Q}''\varepsilon_M \tag{2-22}$$

where $\mathbf{P}''$ and $\mathbf{Q}''$ are differential operators.

Similarly shear stresses produce only shear deformations, and the same relation must apply for all five components in equation (2-17) to ensure isotropy. This relationship is represented

by

$$\sum_{k=0}^{m''} p'_k \frac{\partial^k S}{\partial t^k} = \sum_{k=0}^{n''} q'_k \frac{\partial^k \eta}{\partial t^k} \tag{2-23}$$

or

$$\mathbf{P}'S = \mathbf{Q}'\eta \tag{2-24}$$

where $\mathbf{P}'$ and $\mathbf{Q}'$ are different sets of differential operators.

The differential operators $\mathbf{P}''$, $\mathbf{Q}''$, $\mathbf{P}'$ and $\mathbf{Q}'$ are independent, and it is customary to set $p''_0 = p'_0 = 1$.

The elastic solid is a special case of viscoelastic materials. The hydrostatic relationship for this material can be derived from equation (2-21) as

$$\sigma_M = q''_0 \varepsilon_M . \tag{2-25}$$

In elastic materials a normal stress produced by a hydrostatic pressure p is proportional to the cubic dilatation or volume expansion, $\varepsilon_{xx} + \varepsilon_{yy} + \varepsilon_{zz}$, and the proportional constant, the bulk modulus K, relates both by

$$p = -K\left(\varepsilon_{xx} + \varepsilon_{yy} + \varepsilon_{zz}\right) \tag{2-26}$$

since in such a situation $\sigma_{xx} = \sigma_{yy} = \sigma_{zz} = -p$. From equation (2-15) it can be seen that

$$\sigma_M = \tfrac{1}{3}\left(\sigma_{xx} + \sigma_{yy} + \sigma_{zz}\right) = -p . \tag{2-27}$$

Therefore from (2-19) and (2-26),

$$\sigma_M = 3K\varepsilon_M \tag{2-28}$$

which leads to

$$q_0'' = 3K. \tag{2-29}$$

In the shear direction,

$$S = q_0' \eta. \tag{2-30}$$

Comparing this with the isotropic elastic shear stress-strain relationship

$$\tau = G\gamma \tag{2-31}$$

and substituting with the tensorial notation of the strain $\varepsilon = \frac{1}{2}\gamma$, the other coefficient is determined

$$q_0' = 2G. \tag{2-32}$$

Therefore, for the isotropic elastic material the differential operators are constants,

$$\mathbf{P}'' = 1,\ \mathbf{Q}'' = 3K,\ \mathbf{P}' = 1 \text{ and } \mathbf{Q}' = 2G. \tag{2-33}$$

When an isotropic material is subjected to simple tension, the only stress present in the material is the normal stress in the direction of the load, which is assumed to be x for now. From equation (2-15), the mean normal stress is

$$\sigma_M = \tfrac{1}{3}\sigma_{xx} \tag{2-34}$$

since $\sigma_{yy} = \sigma_{zz} = 0$. Substitute this in the corresponding components in equation (2-14),

$$\sigma_{xx} = \sigma_M + S_{xx}. \tag{2-35}$$

Therefore, the deviatoric portion is

$$S_{xx} = \tfrac{2}{3}\sigma_{xx} \tag{2-36}$$

which leads to

$$S_{yy} = S_{zz} = -\tfrac{1}{3}\sigma_{xx}. \tag{2-37}$$

The corresponding state of strains has three components; the longitudinal strain ε_{xx} and transverse contractions $\varepsilon_{yy} = \varepsilon_{zz}$. From equation (2-19), the mean normal strain is

$$\varepsilon_M = \tfrac{1}{3}\left(\varepsilon_{xx} + 2\varepsilon_{yy}\right) \text{ or } \varepsilon_M = \tfrac{1}{3}\left(\varepsilon_{xx} + 2\varepsilon_{zz}\right). \tag{2-38}$$

From (2-18), the deviatoric portion is

$$\eta_{xx} = \varepsilon_{xx} - \varepsilon_M \tag{2-39}$$

or

$$\eta_{xx} = \tfrac{2}{3}\left(\varepsilon_{xx} - \varepsilon_{yy}\right) \tag{2-40}$$

and it follows that

$$\eta_{yy} = \eta_{zz} = -\tfrac{1}{3}\left(\varepsilon_{xx} - \varepsilon_{yy}\right). \tag{2-41}$$

Therefore the spherical components of stress and strain are related by (2-22), and using (2-34) and (2-38),

$$\mathbf{P}''\left(\tfrac{1}{3}\sigma_{xx}\right) = \mathbf{Q}''\left[\tfrac{1}{3}\left(\varepsilon_{xx} + 2\varepsilon_{yy}\right)\right] \tag{2-42a}$$

and the deviatoric components, from (2-24), (2-36) and (2-40),

$$\mathbf{P}'\left(\tfrac{2}{3}\sigma_{xx}\right) = \mathbf{Q}'\left[\tfrac{2}{3}\left(\varepsilon_{xx} - \varepsilon_{yy}\right)\right]. \tag{2-42b}$$

Equations (2-42) can be expanded to form

$$\mathbf{P}''\sigma_{xx} = \mathbf{Q}''\varepsilon_{xx} + 2\mathbf{Q}''\varepsilon_{yy} \tag{2-43a}$$

and

$$\mathbf{P}'\sigma_{xx} = \mathbf{Q}'\varepsilon_{xx} - \mathbf{Q}'\varepsilon_{yy}. \tag{2-43b}$$

Apply $\mathbf{Q}'$ to (2-43a) and $2\mathbf{Q}''$ to (2-43b) and add,

$$\left(\mathbf{Q}'\mathbf{P}'' + 2\mathbf{Q}''\mathbf{P}'\right)\sigma_{xx} = \left(\mathbf{Q}'\mathbf{Q}'' + 2\mathbf{Q}''\mathbf{Q}'\right)\varepsilon_{xx} + 2\left(\mathbf{Q}'\mathbf{Q}'' - \mathbf{Q}''\mathbf{Q}'\right)\varepsilon_{yy}. \tag{2-44}$$

Since the differential operators are communicative, *i.e.* $\mathbf{Q}'\mathbf{Q}''\varepsilon_{yy} = \mathbf{Q}''\mathbf{Q}'\varepsilon_{yy}$, (2-44) becomes

$$\left(\mathbf{P}''\mathbf{Q}' + 2\mathbf{Q}''\mathbf{P}'\right)\sigma_{xx} = 3\mathbf{Q}''\mathbf{Q}'\varepsilon_{xx}. \tag{2-45}$$

One approximation here is to assume that the response in dilatation is elastic, thus from (2-33), $\mathbf{P}'' = 1$, $\mathbf{Q}'' = 3K$, and the equation (2-45) can be reduced to

$$\left(\mathbf{Q}' + 6K\mathbf{P}'\right)\sigma_{xx} = 9K\mathbf{Q}'\varepsilon_{xx}. \tag{2-46}$$

If the deviatoric response is assumed to follow the governing equation for the three-parameter solid, (2-46) must have the form of (2-10). Therefore,

$$\mathbf{P}' = 1 + p_1' \frac{\partial}{\partial t} \tag{2-47a}$$

$$\mathbf{Q}' = q_0' + q_1' \frac{\partial}{\partial t}. \tag{2-47b}$$

Using (2-47), equation (2-46) can be rewritten as

$$\left(q_0' + 6K\right)\sigma_{xx} + \left(q_1' + 6Kp_1'\right)\frac{\partial \sigma_{xx}}{\partial t} = 9Kq_0'\varepsilon_{xx} + 9Kq_1'\frac{\partial \varepsilon_{xx}}{\partial t}. \tag{2-48}$$

Divide (2-48) by $\left(q_0' + 6K\right)$ to get

$$\sigma_{xx} + \left(\frac{q_1' + 6Kp_1'}{q_0' + 6K}\right)\frac{\partial \sigma_{xx}}{\partial t} = \left(\frac{9Kq_0'}{q_0' + 6K}\right)\varepsilon_{xx} + \left(\frac{9Kq_1'}{q_0' + 6K}\right)\frac{\partial \varepsilon_{xx}}{\partial t} \tag{2-49}$$

Equation (2-49) must correspond to the one-dimensional governing equation (2-10). Therefore,

$$p_0 = 1$$

$$p_1 = \frac{q_1' + 6Kp_1'}{q_0' + 6K} \tag{2-50a}$$

$$q_0 = \frac{9Kq_0'}{q_0' + 6K} \tag{2-50b}$$

$$q_1 = \frac{9Kq_1'}{q_0' + 6K} \tag{2-50c}$$

or,

$$p_1' = \frac{9Kp_1 - q_1}{9K - q_0} \tag{2-51a}$$

$$q_0' = \frac{6q_0K}{9K - q_0} \tag{2-51b}$$

$$q_1' = \frac{6q_1K}{9K - q_0}. \tag{2-51c}$$

Combined with (2-12),

$$p_1' = \frac{9K\eta_2 - E_1\eta_2}{9K\left(E_1 + E_2\right) - E_1E_2} \tag{2-52a}$$

$$q_0' = \frac{6KE_1E_2}{9K\left(E_1 + E_2\right) - E_1E_2} \tag{2-52b}$$

$$q_1' = \frac{6KE_1\eta_2}{9K\left(E_1 + E_2\right) - E_1E_2}. \tag{2-52c}$$

Now the coefficients $p_0'(=1)$, p_1', q_0' and q_1' define the differential operators in the deviatoric governing equation for the three-parameter solid, the deviatoric or shear relaxation modulus can be found.

The stress relaxation modulus is found experimentally by applying a constant strain and observe the resulting stress as a function of time. This is expressed mathematically by the application of strain $\varepsilon = \varepsilon_0\Delta(t)$ where $\Delta(t)$ is the unit step function,

$$\Delta(t) = 0 \text{ for } t < 0,$$
$$\Delta(t) = 1 \text{ for } t > 0.$$

Then the stress is proportional to ε_0;

$$\sigma(t) = \varepsilon_0 Y(t) \tag{2-53}$$

and the proportional function $Y(t)$ is the relaxation modulus.

Now a standard governing equation for a viscoelastic material

$$\sum_{k=0}^{m} p_k \frac{\partial^k \sigma}{\partial t^k} = \sum_{k=0}^{n} q_k \frac{\partial^k \varepsilon}{\partial t^k} \tag{2-54}$$

can be transformed in the Laplace plane to form

$$\sum_{k=0}^{m} p_k s^k \bar{\sigma} = \sum_{k=0}^{n} q_k s^k \bar{\varepsilon} \tag{2-55}$$

or
$$\mathcal{P}(s)\bar{\sigma} = \mathcal{Q}(s)\bar{\varepsilon} \tag{2-56}$$

where $\mathcal{P}(s)$ and $\mathcal{Q}(s)$ are polynomials in *s*, and the bar denotes the Laplace transform. Though the Laplace transform of a derivative of a function is

$$\int_0^\infty \frac{d^k f(t)}{dt^k} e^{-st} = s^k \bar{f}(s) - \sum_{n=1}^{k} s^{n-1} \frac{d^{n-1} f}{dt^{n-1}}(0) \tag{2-57}$$

all f terms in the equation (2-57) vanish if f vanishes for $t < 0$ and the base is taken from 0^-.

Substitute the Laplace transforms of $\varepsilon = \varepsilon_0 \Delta(t)$ with $\varepsilon_0 = 1$ and (2-53) into (2-56), then

$$\overline{Y}(s) = \frac{Q(s)}{s\mathcal{P}(s)}. \tag{2-58}$$

For the three-parameter solid

$$Q(s) = q_0 + sq_1$$

$$\mathcal{P}(s) = 1 + sp_1.$$

Now the deviatoric stress relaxation modulus can be found by replacing $Q(s)$ and $\mathcal{P}(s)$ by $Q'(s)$ and $\mathcal{P}'(s)$ where

$$Q'(s) = q_0' + sq_1' \tag{2-59}$$

$$\mathcal{P}'(s) = 1 + sp_1'. \tag{2-60}$$

From equation (2-58), the Laplace transform of the deviatoric relaxation modulus $\overline{G}'(s)$ can be expressed as

$$\overline{G}'(s) = \frac{q_0' + sq_1'}{s(1 + sp_1')} \tag{2-61}$$

which can be split into partial fractions

$$\overline{G}'(s) = \frac{1}{p_1'}\left[\frac{p_1'q_0'}{s} + \frac{q_1' - p_1'q_0'}{\left(\frac{1}{p_1'} + s\right)}\right]. \tag{2-62}$$

Now transform (2-62) back to the physical plane,

$$G'(t) = q_0'\Delta t + \left(\frac{q_1' - p_1' q_0'}{p_1'} \right) e^{(-t/p_1')} \tag{2-63}$$

where Δt is a unit step function

$$\Delta t = 0 \text{ for } t < 0$$
$$\Delta t = 1 \text{ for } t > 0.$$

Here only the time $t > 0$ is of concern, therefore $\Delta t = 1$. Then the stress relaxation modulus is

$$G'(t) = q_0' + \left(\frac{q_1'}{p_1'} - q_0' \right) e^{(-t/p_1')}, \tag{2-64}$$

as it is found in Flügge [15].

The constitutive relation between stress and strain in a viscoelastic material can also be expressed in terms of frequency in the complex plane, that is,

$$\sigma = \Sigma e^{i\omega t}$$

$$\varepsilon = \mathrm{E} e^{i\omega t}.$$

The following derivation is analogous to what is found in Fung [17]. Then the differentiation with respect to time is equivalent to multiplication by $i\omega$. Therefore the equation (2-10) can be rewritten as

$$(1 + p_1 i\omega)\Sigma = (q_0 + q_1 i\omega)\mathrm{E}$$

or $$\Sigma = \frac{q_0 + q_1 i\omega}{1 + p_1 i\omega} \mathrm{E}$$

where

$$E(i\omega) = \frac{q_0 + q_1 i\omega}{1 + p_1 i\omega} \tag{2-65}$$

is the complex modulus for the three-parameter viscoelastic solid model. Equation (2-65) can be decomposed into the real and imaginary parts,

$$E(i\omega) = \frac{q_0 + p_1 q_1 \omega^2}{1 + {p_1}^2 \omega^2} + \frac{q_1 \omega - p_1 q_0 \omega}{1 + {p_1}^2 \omega^2} i \tag{2-66}$$

or $$E(i\omega) = E_1 + E_2 i$$

where

$$E_1 = \frac{q_0 + p_1 q_1 \omega^2}{1 + {p_1}^2 \omega^2} \tag{2-67a}$$

$$E_2 = \frac{q_1 \omega - q_1 q_0 \omega}{1 + {p_1}^2 \omega^2}. \tag{2-67b}$$

E_1 is the storage modulus, and E_2 is the loss modulus.

Its magnitude is the “apparent” stiffness which is expressed as

$$\left|E(i\omega)\right| = \sqrt{\frac{{q_0}^2 + {q_1}^2 \omega^2}{1 + {p_1}^2 \omega^2}}.$$

The ratio of the loss modulus (the imaginary part) and the storage modulus (the real part) is the measure of the internal friction. This value, shown in the Argand diagram (the complex plane), is the tangent of the complex modulus "vector" and sometimes referred to as the loss tangent. This value is shown to be

$$\tan\delta = \frac{q_1\omega - p_1 q_0 \omega}{q_0 + p_1 q_1 \omega^2}$$

where δ is the phase angle. By plotting $|E(i\omega)|$ and $\tan\delta$ against frequency, the frequency-dependence of the three-parameter viscoelastic solid is shown in Figure 2.2. It must be noted that the abscissa is in the log scale. As illustrated, at lower frequency the magnitude of the complex modulus stays virtually constant and the loss tangent is nearly zero, indicating that at this range internal friction is practically non-existent. The same can be observed at high frequency ranges. In between the magnitude of the complex modulus changes and the internal friction shows an increase. Within this frequency window the viscous effect is more prominent and outside of this window, the linear elastic units dominate the response. At lower frequency, the three-parameter viscoelastic model can be considered as two linear elastic units in series (E_1 and E_2 in Figure 2.1) and at higher frequency, only one linear elastic unit (E_1 in Figure 2.1).

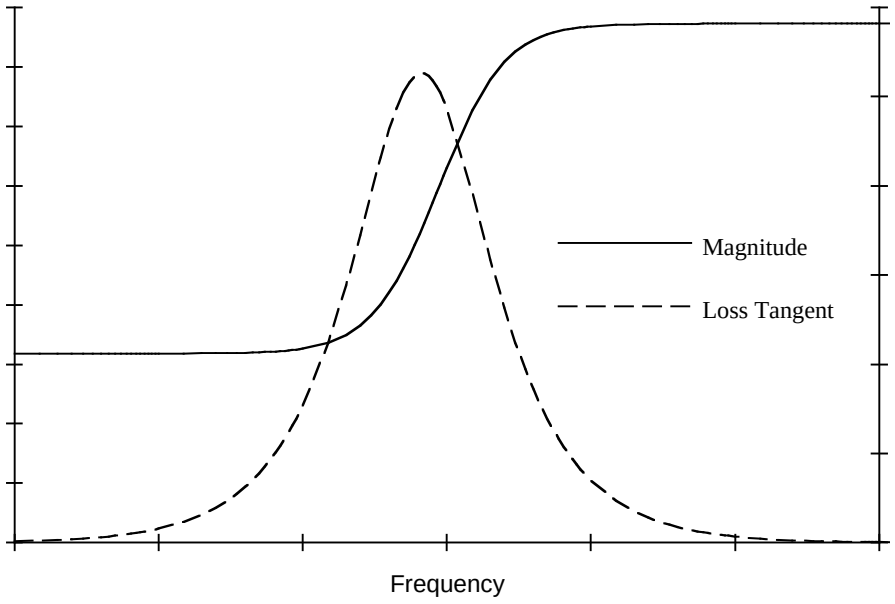

Figure 2.2 Frequency-Dependency of Three-Parameter Viscoelastic Solid: Magnitude and Loss Tangent of Complex Modulus

2.2 Wave Propagation

2.2.1 Elastic Wave

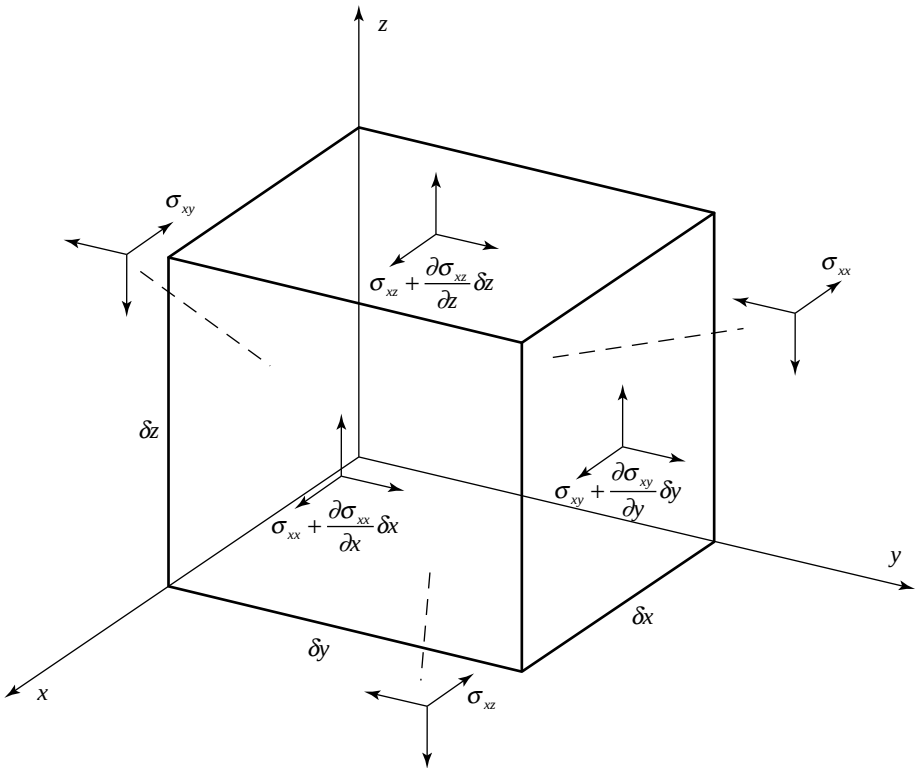

Figure 2.3 Three Dimensional State of Stress in an Infinitesimally Small Parallelepiped Segment

The derivations of wave propagation speed and particle velocity are based on Kolskey [42] and Timoshenko and Goodier [84]. For an infinitesimally small parallelepiped segment with stresses, take the resultant in the x direction,

$$\left(\sigma_{xx}+\frac{\partial\sigma_{xx}}{\partial x}\delta x\right)\delta y\delta z-\sigma_{xx}\delta y\delta z+$$
$$\left(\tau_{xy}+\frac{\partial\sigma_{xy}}{\partial y}\delta y\right)\delta x\delta z-\sigma_{xy}\delta x\delta z+$$
$$\left(\tau_{zx}+\frac{\partial\sigma_{xz}}{\partial z}\delta z\right)\delta x\delta y-\sigma_{zx}\delta x\delta y=\rho\delta x\delta y\delta z\frac{\partial^2 u}{\partial t^2}$$

or
$$\left(\frac{\partial\sigma_{xx}}{\partial x}+\frac{\partial\sigma_{xy}}{\partial y}+\frac{\partial\sigma_{xz}}{\partial z}\right)\delta x\delta y\delta z=\rho\delta x\delta y\delta z\frac{\partial^2 u}{\partial t^2}. \tag{2-68}$$

Therefore,

$$\frac{\partial\sigma_{x}}{\partial x}+\frac{\partial\sigma_{xy}}{\partial y}+\frac{\partial\sigma_{xz}}{\partial z}=\rho\frac{\partial^2 u}{\partial t^2}. \tag{2-69a}$$

Similarly in other directions, the equations

$$\frac{\partial\sigma_{yx}}{\partial x}+\frac{\partial\sigma_{yy}}{\partial y}+\frac{\partial\sigma_{yz}}{\partial z}=\rho\frac{\partial^2 v}{\partial t^2} \tag{2-69b}$$

and
$$\frac{\partial\sigma_{zx}}{\partial x}+\frac{\partial\sigma_{zy}}{\partial y}+\frac{\partial\sigma_{zz}}{\partial z}=\rho\frac{\partial^2 w}{\partial t^2} \tag{2-69c}$$

are obtained.

The elastic material is assumed to follow the Hooke's law, which can be described as

$$\begin{Bmatrix}\sigma_{xx}\\ \sigma_{yy}\\ \sigma_{zz}\\ \sigma_{yz}\\ \sigma_{zx}\\ \sigma_{xy}\end{Bmatrix}=\begin{bmatrix}c_{11} & c_{12} & c_{13} & c_{14} & c_{15} & c_{16}\\ c_{21} & c_{22} & c_{23} & c_{24} & c_{25} & c_{26}\\ c_{31} & c_{32} & c_{33} & c_{34} & c_{35} & c_{36}\\ c_{41} & c_{42} & c_{43} & c_{44} & c_{45} & c_{46}\\ c_{51} & c_{52} & c_{53} & c_{54} & c_{55} & c_{56}\\ c_{61} & c_{62} & c_{63} & c_{64} & c_{65} & c_{66}\end{bmatrix}\begin{Bmatrix}\varepsilon_{xx}\\ \varepsilon_{yy}\\ \varepsilon_{zz}\\ \gamma_{yz}\\ \gamma_{zx}\\ \gamma_{xy}\end{Bmatrix}. \tag{2-70}$$

For isotropic materials, there are only two independent constants;

$$c_{12}=c_{13}=c_{21}=c_{23}=c_{31}=c_{32}=\lambda$$

$$c_{44}=c_{55}=c_{66}=\mu$$

$$c_{11}=c_{22}=c_{33}=\lambda+2\mu$$

where λ and μ are Lame's constants. Using these two constants, stress components can be expressed as:

$$\sigma_{xx}=\lambda\Delta+2\mu\varepsilon_{xx} \tag{2-71a}$$

$$\sigma_{yy}=\lambda\Delta+2\mu\varepsilon_{yy} \tag{2-71b}$$

$$\sigma_{zz}=\lambda\Delta+2\mu\varepsilon_{zz} \tag{2-71c}$$

$$\sigma_{yz}=\mu\gamma_{yz} \tag{2-72a}$$

$$\sigma_{zx}=\mu\gamma_{zx} \tag{2-72b}$$

and $$\sigma_{xy} = \mu\gamma_{xy} \tag{2-72c}$$

where $\Delta = \varepsilon_{xx} + \varepsilon_{yy} + \varepsilon_{zz}$.

Substitute equations (2-71) and (2-72) into (2-69a) to obtain

$$\rho\frac{\partial^2 u}{\partial t^2} = \frac{\partial}{\partial x}\left(\lambda\Delta + 2\mu\varepsilon_x\right) + \frac{\partial}{\partial y}\left(\mu\gamma_{xy}\right) + \frac{\partial}{\partial z}\left(\mu\gamma_{xz}\right). \tag{2-73}$$

Substituting $\varepsilon_x = \frac{\partial u}{\partial x}$, $\gamma_{xz} = \frac{\partial w}{\partial x} + \frac{\partial u}{\partial z}$ and $\gamma_{xy} = \frac{\partial v}{\partial x} + \frac{\partial u}{\partial y}$ into the equation above, the resulting equation of motion is

$$\rho\frac{\partial^2 u}{\partial t^2} = \left(\lambda + \mu\right)\frac{\partial\Delta}{\partial x} + \mu\nabla^2 u \tag{2-74a}$$

where ∇^2 is a differential operator $\frac{\partial^2}{\partial x^2} + \frac{\partial^2}{\partial y^2} + \frac{\partial^2}{\partial z^2}$.

Similarly in other directions,

$$\rho\frac{\partial^2 v}{\partial t^2} = \left(\lambda + \mu\right)\frac{\partial\Delta}{\partial y} + \mu\nabla^2 v \tag{2-74b}$$

and $$\rho\frac{\partial^2 w}{\partial t^2} = \left(\lambda + \mu\right)\frac{\partial\Delta}{\partial z} + \mu\nabla^2 w. \tag{2-74c}$$

Equations (2-74) are the equations of motion for the elastic isotropic material without body forces.

Now, differentiate equations (2-74) with respect to x, y and z, respectively, to get

$$\rho\frac{\partial}{\partial x}\left(\frac{\partial^2 u}{\partial t^2}\right)=(\lambda+\mu)\frac{\partial^2\Delta}{\partial x^2}+\mu\frac{\partial}{\partial x}\nabla^2 u \tag{2-75a}$$

$$\rho\frac{\partial}{\partial y}\left(\frac{\partial^2 v}{\partial t^2}\right)=(\lambda+\mu)\frac{\partial^2\Delta}{\partial y^2}+\mu\frac{\partial}{\partial y}\nabla^2 v \tag{2-75b}$$

$$\rho\frac{\partial}{\partial z}\left(\frac{\partial^2 w}{\partial t^2}\right)=(\lambda+\mu)\frac{\partial^2\Delta}{\partial z^2}+\mu\frac{\partial}{\partial z}\nabla^2 w. \tag{2-75c}$$

Add (2-75) together to form

$$\rho\frac{\partial^2\Delta}{\partial t^2}=(\lambda+\mu)\left(\frac{\partial^2\Delta}{\partial x^2}+\frac{\partial^2\Delta}{\partial y^2}+\frac{\partial^2\Delta}{\partial z^2}\right)+\mu\left(\frac{\partial}{\partial x}\nabla^2 u+\frac{\partial}{\partial y}\nabla^2 v+\frac{\partial}{\partial z}\nabla^2 w\right) \tag{2-76}$$

or

$$\rho\frac{\partial^2\Delta}{\partial t^2}=(\lambda+2\mu)\nabla^2\Delta. \tag{2-77}$$

This is the wave equation for dilatational or irrotational waves with the propagation wave speed of

$$c_1=\sqrt{\frac{\lambda+2\mu}{\rho}}. \tag{2-78}$$

Now, if dilatation Δ is zero in equations (2-75), (2-75) become

$$\rho\frac{\partial}{\partial x}\left(\frac{\partial^2 u}{\partial t^2}\right)=\mu\frac{\partial}{\partial x}\nabla^2 u \tag{2-79a}$$

$$\rho \frac{\partial}{\partial y}\left(\frac{\partial^2 v}{\partial t^2}\right) = \mu \frac{\partial}{\partial y}\nabla^2 v \tag{2-79b}$$

$$\rho \frac{\partial}{\partial z}\left(\frac{\partial^2 w}{\partial t^2}\right) = \mu \frac{\partial}{\partial z}\nabla^2 w. \tag{2-79c}$$

These are the equations of motion for distortional or equivoluminal waves with the propagation wave speed of

$$c_2 = \sqrt{\frac{\mu}{\rho}}. \tag{2-80}$$

If the one-dimensional dilatational wave propagation is concerned, the wave propagation in the x direction is obtained by setting $\varepsilon_{yy} = \varepsilon_{zz} = 0$ in equation (2-77) as:

$$\rho \frac{\partial^2 u}{\partial t^2} = (\lambda + 2\mu)\frac{\partial^2 u}{\partial x^2}. \tag{2-81}$$

Here the x direction is selected as the direction of wave travel, but this selection is irrelevant due to the isotropy of the material.

Assume the solution has the form

$$u = f(x - c_1 t) + g(x + c_1 t) \tag{2-82}$$

where c_1 is the dilatational wave propagation speed (2-78).

The physical interpretation of (2-82) is that the function f represents the wave propagating in the negative x direction, whereas g the wave propagating in the positive x direction. It is assumed for now the wave propagation in the positive x direction is of concern. Therefore $g \equiv 0$.

Substituting the argument of f by $\xi = x - c_1 t$, the particle velocity v can be expressed as

$$v = \frac{\partial u}{\partial t} = -\frac{1}{c_1}\frac{\partial f}{\partial \xi}. \tag{2-83}$$

From (2-71a), (again, $\varepsilon_{yy} = \varepsilon_{zz} = 0$)

$$\sigma_{xx} = (\lambda + 2\mu)\varepsilon_{xx}. \tag{2-84}$$

Since now ε_{xx} can be expressed as

$$\varepsilon_{xx} = \frac{\partial u}{\partial x} = \frac{\partial f}{\partial \xi} \tag{2-85}$$

which combined with (2-83) becomes

$$\varepsilon_{xx} = -\frac{v}{c_1}. \tag{2-86}$$

From (2-78) it can be shown that

$$(\lambda + 2\mu) = {c_1}^2 \rho. \tag{2-87}$$

Therefore from (2-86), (2-87) and (2-84),

$$\sigma_{xx} = -c_1 \rho v \tag{2-88}$$

or

$$v = -\frac{\sigma_{xx}}{c_1 \rho} \tag{2-89}$$

which is the particle velocity of the elastic dilatational wave. The minus sign simply indicates that the particle velocity is in the positive x direction when the stress is negative, *i.e.* compressive.

2.2.2 Viscoelastic Wave

The equations of motion (2-69) are valid here as well. The three-parameter viscoelastic model is applied to derive a unique solution. Differentiate (2-69a) with respect to t, multiply it by p_1', where p_1' is a coefficient in the three-parameter solid stress-strain relation introduced earlier, to get

$$\rho p_1' \frac{\partial^3 u}{\partial t^3} = p_1' \frac{\partial}{\partial t}\left(\frac{\partial \sigma_{xx}}{\partial x} \right) + p_1' \frac{\partial}{\partial t}\left(\frac{\partial \sigma_{xy}}{\partial x} \right) + p_1' \frac{\partial}{\partial t}\left(\frac{\partial \sigma_{xz}}{\partial x} \right). \tag{2-90}$$

Add this and equation (2-69a) to get

$$\begin{aligned} \rho \frac{\partial^2 u}{\partial t^2} + \rho p_1' \frac{\partial^3 u}{\partial t^3} = {} & \frac{\partial \sigma_{xx}}{\partial x} + p_1' \frac{\partial}{\partial t}\left(\frac{\partial \sigma_{xx}}{\partial x} \right) \\ & + \frac{\partial \sigma_{xy}}{\partial x} + p_1' \frac{\partial}{\partial t}\left(\frac{\partial \sigma_{xy}}{\partial x} \right). \\ & + \frac{\partial \sigma_{xz}}{\partial x} + p_1' \frac{\partial}{\partial t}\left(\frac{\partial \sigma_{xz}}{\partial x} \right) \end{aligned} \tag{2-91}$$

Decompose the stresses into the spherical and deviatoric components by substituting

$$\sigma_{xx} = \sigma_M + S_{xx} \tag{2-92a}$$

$$\sigma_{xy} = S_{xy} \tag{2-92b}$$

$$\sigma_{xz} = S_{xz}, \tag{2-92c}$$

equation (2-91) can be rewritten as

$$\rho\frac{\partial^2 u}{\partial t^2} + \rho p_1'\frac{\partial^3 u}{\partial t^3} = \frac{\partial}{\partial x}\left(\sigma_M + S_{xx}\right) + p_1'\frac{\partial}{\partial t}\left[\frac{\partial}{\partial x}\left(\sigma_M + S_{xx}\right)\right] + \frac{\partial S_{xy}}{\partial x} + p_1'\frac{\partial}{\partial t}\left(\frac{\partial S_{xy}}{\partial x}\right) + \frac{\partial S_{xz}}{\partial x} + p_1'\frac{\partial}{\partial t}\left(\frac{\partial S_{xz}}{\partial x}\right)$$

or

$$\rho\frac{\partial^2 u}{\partial t^2} + \rho p_1'\frac{\partial^3 u}{\partial t^3} = \frac{\partial}{\partial x}\left(\sigma_M + p_1'\frac{\partial \sigma_M}{\partial t}\right) + \frac{\partial}{\partial x}\left(S_{xx} + p_1'\frac{\partial S_{xx}}{\partial t}\right) + \frac{\partial}{\partial y}\left(S_{xy} + p_1'\frac{\partial S_{xy}}{\partial t}\right) + \frac{\partial}{\partial z}\left(S_{xz} + p_1'\frac{\partial S_{xz}}{\partial t}\right). \tag{2-93}$$

If the deviatoric stress-strain relation is assumed to follow the three-parameter viscoelastic model, it has the form (see the previous Section),

$$S + p_1'\frac{\partial S}{\partial t} = q_0'\eta + q_1'\frac{\partial \eta}{\partial t}$$

and (2-93) becomes

$$\rho\frac{\partial^2 u}{\partial t^2} + \rho p_1'\frac{\partial^3 u}{\partial t^3} = \frac{\partial}{\partial x}\left(\sigma_M + p_1'\frac{\partial \sigma_M}{\partial t}\right) + \frac{\partial}{\partial x}\left(q_0'\eta_{xx} + q_1'\frac{\partial \eta_{xx}}{\partial t}\right) + \frac{\partial}{\partial y}\left(q_0'\eta_{xy} + q_1'\frac{\partial \eta_{xy}}{\partial t}\right) + \frac{\partial}{\partial z}\left(q_0'\eta_{xz} + q_1'\frac{\partial \eta_{xz}}{\partial t}\right) \tag{2-94}$$

where

$$\eta_{xx} = \varepsilon_{xx} - \varepsilon_M = \varepsilon_{xx} - \tfrac{1}{3}\Delta \tag{2-95a}$$

$$\eta_{xy} = \varepsilon_{xy} = \frac{1}{2}\left(\frac{\partial v}{\partial x} + \frac{\partial u}{\partial y}\right) \tag{2-95b}$$

$$\eta_{xz} = \varepsilon_{xz} = \frac{1}{2}\left(\frac{\partial w}{\partial x} + \frac{\partial u}{\partial z}\right). \tag{2-95c}$$

Rewrite (2-94) using above relations to get

$$\begin{aligned}\rho\frac{\partial^2 u}{\partial t^2} + \rho p_1'\frac{\partial^3 u}{\partial t^3} = {} & \frac{\partial}{\partial x}\left(\sigma_M + p_1'\frac{\partial \sigma_M}{\partial t}\right) \\ & + \frac{\partial}{\partial x}\left[q_0'\left(\frac{\partial u}{\partial x} - \frac{\Delta}{3}\right) + q_1'\frac{\partial}{\partial t}\left(\frac{\partial u}{\partial x} - \frac{\Delta}{3}\right)\right] \\ & + \frac{\partial}{\partial y}\left[\frac{q_0'}{2}\left(\frac{\partial v}{\partial x} + \frac{\partial u}{\partial y}\right) + \frac{q_1'}{2}\frac{\partial}{\partial t}\left(\frac{\partial v}{\partial x} + \frac{\partial u}{\partial y}\right)\right] \\ & + \frac{\partial}{\partial z}\left[\frac{q_0'}{2}\left(\frac{\partial w}{\partial x} + \frac{\partial u}{\partial z}\right) + \frac{q_1'}{2}\frac{\partial}{\partial t}\left(\frac{\partial w}{\partial x} + \frac{\partial u}{\partial z}\right)\right]\end{aligned}$$

or

$$\begin{aligned}\rho\frac{\partial^2 u}{\partial t^2} + \rho p_1'\frac{\partial^3 u}{\partial t^3} = {} & \frac{\partial}{\partial x}\left(\sigma_M + p_1'\frac{\partial \sigma_M}{\partial t}\right) \\ & + q_0'\left(\frac{\partial^2 u}{\partial x^2} - \frac{1}{3}\frac{\partial \Delta}{\partial x}\right) + q_1'\frac{\partial}{\partial t}\left(\frac{\partial^2 u}{\partial x^2} - \frac{1}{3}\frac{\partial \Delta}{\partial x}\right) \\ & + \frac{q_0'}{2}\left(\frac{\partial^2 v}{\partial x \partial y} + \frac{\partial^2 u}{\partial y^2}\right) + \frac{q_1'}{2}\frac{\partial}{\partial t}\left(\frac{\partial^2 v}{\partial x \partial y} + \frac{\partial^2 u}{\partial y^2}\right) \\ & + \frac{q_0'}{2}\left(\frac{\partial^2 w}{\partial x \partial z} + \frac{\partial^2 u}{\partial z^2}\right) + \frac{q_1'}{2}\frac{\partial}{\partial t}\left(\frac{\partial^2 w}{\partial x \partial z} + \frac{\partial^2 u}{\partial z^2}\right)\end{aligned}. \tag{2-96a}$$

Similar operations are performed on (2-69b) and (2-69c) to obtain

$$\begin{aligned}\rho\frac{\partial^2 v}{\partial t^2}+\rho p_1'\frac{\partial^3 v}{\partial t^3}=&\frac{\partial}{\partial y}\left(\sigma_M+p_1'\frac{\partial\sigma_M}{\partial t}\right)\\&+\frac{q_0'}{2}\left(\frac{\partial^2 v}{\partial x^2}+\frac{\partial^2 u}{\partial x\partial y}\right)+\frac{q_1'}{2}\frac{\partial}{\partial t}\left(\frac{\partial^2 v}{\partial x^2}+\frac{\partial^2 u}{\partial x\partial y}\right)\\&+q_0'\left(\frac{\partial^2 v}{\partial y^2}-\frac{1}{3}\frac{\partial\Delta}{\partial y}\right)+q_1'\frac{\partial}{\partial t}\left(\frac{\partial^2 v}{\partial y^2}-\frac{1}{3}\frac{\partial\Delta}{\partial y}\right)\\&+\frac{q_0'}{2}\left(\frac{\partial^2 w}{\partial z\partial y}+\frac{\partial^2 v}{\partial z^2}\right)+\frac{q_1'}{2}\frac{\partial}{\partial t}\left(\frac{\partial^2 w}{\partial z\partial y}+\frac{\partial^2 v}{\partial z^2}\right)\end{aligned} \tag{2-96b}$$

$$\begin{aligned}\rho\frac{\partial^2 w}{\partial t^2}+\rho p_1'\frac{\partial^3 w}{\partial t^3}=&\frac{\partial}{\partial z}\left(\sigma_M+p_1'\frac{\partial\sigma_M}{\partial t}\right)\\&+\frac{q_0'}{2}\left(\frac{\partial^2 w}{\partial x^2}+\frac{\partial^2 u}{\partial x\partial z}\right)+\frac{q_1'}{2}\frac{\partial}{\partial t}\left(\frac{\partial^2 w}{\partial x^2}+\frac{\partial^2 u}{\partial x\partial z}\right)\\&+\frac{q_0'}{2}\left(\frac{\partial^2 w}{\partial y^2}+\frac{\partial^2 v}{\partial y\partial z}\right)+\frac{q_1'}{2}\frac{\partial}{\partial t}\left(\frac{\partial^2 w}{\partial y^2}+\frac{\partial^2 v}{\partial y\partial z}\right)\\&+q_0'\left(\frac{\partial^2 w}{\partial z^2}-\frac{1}{3}\frac{\partial\Delta}{\partial z}\right)+q_1'\frac{\partial}{\partial t}\left(\frac{\partial^2 w}{\partial z^2}-\frac{1}{3}\frac{\partial\Delta}{\partial z}\right)\end{aligned} \tag{2-96c}$$

and

Now differentiate (2-96a) with respect to x, (2-96b), to y and (2-96c), to z, respectively, and add, then the left side of the resulting equation is

$$\rho\frac{\partial^2}{\partial t^2}\frac{\partial u}{\partial x}+\rho p_1'\frac{\partial^3}{\partial t^3}\frac{\partial u}{\partial x}+\rho\frac{\partial^2}{\partial t^2}\frac{\partial v}{\partial y}+\rho p_1'\frac{\partial^3}{\partial t^3}\frac{\partial v}{\partial y}+\rho\frac{\partial^2}{\partial t^2}\frac{\partial w}{\partial z}+\rho p_1'\frac{\partial^3}{\partial t^3}\frac{\partial w}{\partial z}$$

or

$$\rho\frac{\partial^2}{\partial t^2}\Delta+\rho p_1'\frac{\partial^3}{\partial t^3}\Delta. \tag{2-97}$$

The right hand side is

$$
\begin{aligned}
&\frac{\partial^2}{\partial x^2}\left(\sigma_M + p_1'\frac{\partial \sigma_M}{\partial t}\right) + \frac{\partial^2}{\partial y^2}\left(\sigma_M + p_1'\frac{\partial \sigma_M}{\partial t}\right) + \frac{\partial^2}{\partial z^2}\left(\sigma_M + p_1'\frac{\partial \sigma_M}{\partial t}\right) \\
&+q_0'\left(\frac{\partial^2}{\partial x^2}\frac{\partial u}{\partial x} - \frac{1}{3}\frac{\partial^2 \Delta}{\partial x^2}\right) + q_1'\frac{\partial}{\partial t}\left(\frac{\partial^2}{\partial x^2}\frac{\partial u}{\partial x} - \frac{1}{3}\frac{\partial^2 \Delta}{\partial x^2}\right) \\
&+\frac{q_0'}{2}\left(\frac{\partial^2}{\partial x^2}\frac{\partial v}{\partial y} + \frac{\partial^2}{\partial y^2}\frac{\partial u}{\partial x}\right) + \frac{q_1'}{2}\frac{\partial}{\partial t}\left(\frac{\partial^2}{\partial x^2}\frac{\partial v}{\partial y} + \frac{\partial^2}{\partial y^2}\frac{\partial u}{\partial x}\right) \\
&+\frac{q_0'}{2}\left(\frac{\partial^2}{\partial x^2}\frac{\partial w}{\partial z} + \frac{\partial^2}{\partial z^2}\frac{\partial u}{\partial x}\right) + \frac{q_1'}{2}\frac{\partial}{\partial t}\left(\frac{\partial^2}{\partial x^2}\frac{\partial w}{\partial z} + \frac{\partial^2}{\partial z^2}\frac{\partial u}{\partial x}\right) \\
&+\frac{q_0'}{2}\left(\frac{\partial^2}{\partial x^2}\frac{\partial v}{\partial y} + \frac{\partial^2}{\partial y^2}\frac{\partial u}{\partial x}\right) + \frac{q_1'}{2}\frac{\partial}{\partial t}\left(\frac{\partial^2}{\partial x^2}\frac{\partial v}{\partial y} + \frac{\partial^2}{\partial y^2}\frac{\partial u}{\partial x}\right) \\
&+q_0'\left(\frac{\partial^2}{\partial y^2}\frac{\partial v}{\partial y} - \frac{1}{3}\frac{\partial^2 \Delta}{\partial y^2}\right) + q_1'\frac{\partial}{\partial t}\left(\frac{\partial^2}{\partial y^2}\frac{\partial v}{\partial y} - \frac{1}{3}\frac{\partial^2 \Delta}{\partial y^2}\right) \\
&+\frac{q_0'}{2}\left(\frac{\partial^2}{\partial y^2}\frac{\partial w}{\partial z} + \frac{\partial^2}{\partial z^2}\frac{\partial v}{\partial y}\right) + \frac{q_1'}{2}\frac{\partial}{\partial t}\left(\frac{\partial^2}{\partial y^2}\frac{\partial w}{\partial z} + \frac{\partial^2}{\partial z^2}\frac{\partial v}{\partial y}\right) \\
&+\frac{q_0'}{2}\left(\frac{\partial^2}{\partial x^2}\frac{\partial w}{\partial z} + \frac{\partial^2}{\partial z^2}\frac{\partial u}{\partial x}\right) + \frac{q_1'}{2}\frac{\partial}{\partial t}\left(\frac{\partial^2}{\partial x^2}\frac{\partial w}{\partial z} + \frac{\partial^2}{\partial z^2}\frac{\partial u}{\partial x}\right) \\
&+\frac{q_0'}{2}\left(\frac{\partial^2}{\partial y^2}\frac{\partial w}{\partial z} + \frac{\partial^2}{\partial z^2}\frac{\partial v}{\partial y}\right) + \frac{q_1'}{2}\frac{\partial}{\partial t}\left(\frac{\partial^2}{\partial y^2}\frac{\partial w}{\partial z} + \frac{\partial^2}{\partial z^2}\frac{\partial v}{\partial y}\right) \\
&+q_0'\left(\frac{\partial^2}{\partial z^2}\frac{\partial w}{\partial z} - \frac{1}{3}\frac{\partial^2 \Delta}{\partial z^2}\right) + q_1'\frac{\partial}{\partial t}\left(\frac{\partial^2}{\partial z^2}\frac{\partial w}{\partial z} - \frac{1}{3}\frac{\partial^2 \Delta}{\partial z^2}\right)
\end{aligned}
\quad . \qquad \text{(2-98)}
$$

By substituting $\frac{\partial u}{\partial x} = \varepsilon_{xx}$, $\frac{\partial v}{\partial y} = \varepsilon_{yy}$ and $\frac{\partial w}{\partial z} = \varepsilon_{zz}$ and collecting terms, (2-98) becomes

$$\frac{\partial^2}{\partial x^2}\left(\sigma_M + p_1'\frac{\partial \sigma_M}{\partial t}\right) + \frac{\partial^2}{\partial y^2}\left(\sigma_M + p_1'\frac{\partial \sigma_M}{\partial t}\right) + \frac{\partial^2}{\partial z^2}\left(\sigma_M + p_1'\frac{\partial \sigma_M}{\partial t}\right)$$
$$+q_0'\left[\frac{\partial^2}{\partial x^2}\left(\varepsilon_{xx}+\varepsilon_{yy}+\varepsilon_{zz}\right) + \frac{\partial^2}{\partial y^2}\left(\varepsilon_{xx}+\varepsilon_{yy}+\varepsilon_{zz}\right) + \frac{\partial^2}{\partial z^2}\left(\varepsilon_{xx}+\varepsilon_{yy}+\varepsilon_{zz}\right)\right.$$
$$\left.-\frac{1}{3}\left(\frac{\partial^2 \Delta}{\partial x^2}+\frac{\partial^2 \Delta}{\partial y^2}+\frac{\partial^2 \Delta}{\partial z^2}\right)\right]$$
$$+q_1'\frac{\partial}{\partial t}\left[\frac{\partial^2}{\partial x^2}\left(\varepsilon_{xx}+\varepsilon_{yy}+\varepsilon_{zz}\right) + \frac{\partial^2}{\partial y^2}\left(\varepsilon_{xx}+\varepsilon_{yy}+\varepsilon_{zz}\right) + \frac{\partial^2}{\partial z^2}\left(\varepsilon_{xx}+\varepsilon_{yy}+\varepsilon_{zz}\right)\right.$$
$$\left.-\frac{1}{3}\left(\frac{\partial^2 \Delta}{\partial x^2}+\frac{\partial^2 \Delta}{\partial y^2}+\frac{\partial^2 \Delta}{\partial z^2}\right)\right]$$

or

$$\begin{aligned}&\frac{\partial^2}{\partial x^2}\left(\sigma_M + p_1'\frac{\partial \sigma_M}{\partial t}\right) + \frac{\partial^2}{\partial y^2}\left(\sigma_M + p_1'\frac{\partial \sigma_M}{\partial t}\right) + \frac{\partial^2}{\partial z^2}\left(\sigma_M + p_1'\frac{\partial \sigma_M}{\partial t}\right)\\ &+q_0'\frac{2}{3}\nabla^2\Delta + q_1'\frac{2}{3}\frac{\partial}{\partial t}\nabla^2\Delta\end{aligned}. \qquad (2\text{-}99)$$

Now if the dilatational response is assumed to be elastic, then

$$\sigma_M = 3K\varepsilon_M \qquad (2\text{-}100)$$

and

$$\frac{\partial \sigma_M}{\partial t} = 3K\frac{\partial \varepsilon_M}{\partial t} = K\frac{\partial \Delta}{\partial t}. \qquad (2\text{-}101)$$

Therefore, the portion of (2-99) involving σ_M becomes

$$\begin{aligned}&\frac{\partial^2}{\partial x^2}\left(\sigma_M + p_1'\frac{\partial \sigma_M}{\partial t}\right) + \frac{\partial^2}{\partial y^2}\left(\sigma_M + p_1'\frac{\partial \sigma_M}{\partial t}\right) + \frac{\partial^2}{\partial z^2}\left(\sigma_M + p_1'\frac{\partial \sigma_M}{\partial t}\right)\\ &= K\nabla^2\Delta + p_1'K\frac{\partial}{\partial t}\nabla^2\Delta\end{aligned} \qquad (2\text{-}102)$$

which, combined with (2-97), (2-99) and (2-102), leads to the final form of the wave equation,

$$\rho\frac{\partial^2}{\partial t^2}\Delta+\rho p_1'\frac{\partial^3}{\partial t^3}\Delta=\left(\frac{2}{3}q_0'+K\right)\nabla^2\Delta+\left(\frac{2}{3}q_1'+Kp_1'\right)\frac{\partial}{\partial t}\nabla^2\Delta. \tag{2-103}$$

Assume a one-dimensional equation in the x direction of the same form as (2-103), so that it becomes

$$\rho\frac{\partial^2 u}{\partial t^2}+\rho p_1'\frac{\partial^3 u}{\partial t^3}=\left(\frac{2}{3}q_0'+K\right)\frac{\partial^2 u}{\partial x^2}+\left(\frac{2}{3}q_1'+Kp_1'\right)\frac{\partial^3 u}{\partial x^2\partial t}.$$

Assume that the general solution has the harmonic form of

$$u=U\exp\left\{i\left(\omega t-f_1 x\right)\right\} \tag{2-104}$$

where

$$f_1=f+i\alpha.$$

Substitute in the wave equation, and with $f_1^2=\left(f+i\alpha\right)^2=f^2+2i\alpha f-\alpha^2$,

$$U\rho\omega^2+U\rho p_1'\omega^3 i-U\left(\frac{2}{3}q_0'+K\right)\left(f^2+2\alpha fi-\alpha^2\right)-U\omega\left(\frac{2}{3}q_1'+Kp_1'\right)\left(f^2+2\alpha fi-\alpha^2\right)i=0.$$

Equate the real and imaginary parts,

$$\rho\omega^2-\left(\frac{2}{3}q_0'+K\right)\left(f^2-\alpha^2\right)+2\alpha f\omega\left(\frac{2}{3}q_1'+Kp_1'\right)=0 \tag{2-105}$$

$$\rho p_1' \omega^3 - 2\alpha f\left(\frac{2}{3}q_0' + K\right) - \omega\left(\frac{2}{3}q_1' + Kp_1'\right)\left(f^2 - \alpha^2\right) = 0\,. \tag{2-106}$$

From (2-105)

$$f^2 - \alpha^2 = \frac{\rho\omega^2 + 2\alpha f\omega\left(\frac{2}{3}q_1' + Kp_1'\right)}{\left(\frac{2}{3}q_0' + K\right)}. \tag{2-107}$$

Substitute this into (2-106) to get,

$$\rho p_1' \omega^3 - 2\alpha f\left(\frac{2}{3}q_0' + K\right) - \omega\left(\frac{2}{3}q_1' + Kp_1'\right)\frac{\rho\omega^2 + 2\alpha f\omega\left(\frac{2}{3}q_1' + Kp_1'\right)}{\left(\frac{2}{3}q_0' + K\right)} = 0$$

or
$$\alpha = \frac{\rho\omega^3\left\{p_1'\left(\frac{2}{3}q_0' + K\right) - \left(\frac{2}{3}q_1' + Kp_1'\right)\right\}}{2\left\{\left(\frac{2}{3}q_0' + K\right)^2 + \omega^2\left(\frac{2}{3}q_1' + Kp_1'\right)^2\right\}f}. \tag{2-108}$$

Substitute (2-108) into (2-107), and by collecting terms a forth-order polynomial in f is obtained

$$Af^4 - Bf^2 - C = 0\,,$$

where
$$A = \frac{\left(\frac{2}{3}q_1' + K\right)\left\{\left(\frac{2}{3}q_0' + K\right)^2 + \omega^2\left(\frac{2}{3}q_1' + Kp_1'\right)^2\right\}}{p^2}$$

$$B=\rho\left\{\left(\frac{2}{3}q_0'+K\right)^2+\omega^2\left(\frac{2}{3}q_1'+Kp_1'\right)^2\right\}+\rho\omega^2\left(\frac{2}{3}q_1'+Kp_1'\right)\left\{p_1'\left(\frac{2}{3}q_0'+K\right)-\left(\frac{2}{3}q_1'+Kp_1'\right)\right\}$$

and

$$C=\frac{\rho^2\omega^4\left(\frac{2}{3}q_0'+K\right)\left\{p_1'\left(\frac{2}{3}q_0'+K\right)-\left(\frac{2}{3}q_1'+Kp_1'\right)\right\}^2}{4\left\{\left(\frac{2}{3}q_0'+K\right)^2+\omega^2\left(\frac{2}{3}q_1'+Kp_1'\right)^2\right\}}.$$

Here the only the wave traveling in the positive x direction is of concern, so f must be real and positive. The solution is

$$\begin{aligned}f^2=&\frac{\omega^2}{2\left(\frac{2}{3}q_0'+K\right)\left\{\left(\frac{2}{3}q_0'+K\right)^2+\omega^2\left(\frac{2}{3}q_1'+Kp_1'\right)^2\right\}}\\&\times\left[B+\sqrt{B^2+\rho^2\omega^2\left(\frac{2}{3}q_0'+K\right)^2\left\{p_1'\left(\frac{2}{3}q_0'+K\right)-\left(\frac{2}{3}q_1'+Kp_1'\right)\right\}^2}\right]\end{aligned}\tag{2-109}$$

where B is the coefficient defined above.

The interpretation of the general form of the solution (2-104) becomes clear when it is expanded and the real part is extracted to form

$$u=Ue^{\alpha x}\cos(\omega t-fx).\tag{2-110}$$

U is determined from the initial conditions, α denotes the exponential decay of the response as the wave travels (therefore must be negative), ω is the frequency of the response and $\frac{\omega}{f}$ is the wave propagation speed.

The particle velocity *v* is expressed by

$$v = \frac{\partial u}{\partial t} = Ui\omega \exp\{i(\omega t - f_1 x)\} \tag{2-111}$$

and the strain ε_{xx}, the strain in the direction of the wave propagation, is expressed by

$$\varepsilon_{xx} = \frac{\partial u}{\partial x} = -Uif_1 \exp\{i(\omega t - f_1 x)\}. \tag{2-112}$$

Therefore, ε_{xx} and v are related by

$$\varepsilon_{xx} = -\frac{f_1}{\omega} v \tag{2-113}$$

Now the stress in the wave propagation direction σ_{xx} can be decomposed in the spherical and deviatoric parts by (2-14),

$$\sigma_{xx} = \sigma_M + S_{xx}. \tag{2-114}$$

Both the mean normal stress and deviatoric stress can be represented in the complex form, and related to their respective strains, ε_{xx} and η_{xx}, by the complex moduli

$$\sigma_{xx} = E''(i\omega)\varepsilon_M + E'(i\omega)\eta_{xx}. \tag{2-115}$$

Since in the one-dimensional case,

$$\varepsilon_M = \frac{1}{3}\varepsilon_{xx} \tag{2-116a}$$

$$\eta_{xx} = \varepsilon_{xx} - \varepsilon_M = \frac{2}{3}\varepsilon_{xx}, \tag{2-116b}$$

equation (2-115) can be rewritten, using (2-113), as

$$\sigma_{xx} = -\left[\frac{1}{3}E''(i\omega) + \frac{2}{3}E'(i\omega)\right]\frac{f_1}{\omega}v. \tag{2-117}$$

Expand $E''(i\omega)$, $E'(i\omega)$ and f_1,

$$\sigma_{xx} = -\frac{1}{3\omega}\left[\{E_1'' + E_2''i\} + 2\{E_1' + E_2'i\}\right](f + i\alpha)v \tag{2-118}$$

where E_1'' and E_2'' are the dilatational storage and loss moduli, and E_1' and E_2', deviatoric storage and loss moduli, respectively. This is more conveniently written as

$$\sigma_{xx} = -\frac{e^{i\theta}v}{3\omega}\sqrt{\left(f^2 + \alpha^2\right)\left\{\left(E_1'' + 2E_1'\right)^2 + \left(E_2'' + 2E_2'\right)^2\right\}} \tag{2-119}$$

where θ is the phase shift which is given by

$$\theta = \tan^{-1}\left\{\frac{f\left(E_2'' + 2E_2'\right) + \alpha\left(E_1'' + 2E_1'\right)}{f\left(E_1'' + 2E_1'\right) - \alpha\left(E_2'' + 2E_2'\right)}\right\}. \tag{2-120}$$

2.3 DYNA3D Validation

2.3.1 Elastic Wave Propagation

The speed of dilatational sound wave in an elastic medium (2-78) is rewritten in terms of elastic constants:

$$c_1 = \sqrt{\frac{(1-\nu)E}{\rho(1-2\nu)(1+\nu)}}$$

The following properties are selected based on a common linear elastic representation of brain tissue found in the literature [34, 69 and others];

$$E = 66.7 \text{ kPa}$$
$$\nu = 0.480$$
$$\rho = 1040 \text{ kg/m}^3$$

with the calculated dilatational wave propagation speed of 23.73 m/s.

In order to induce a dilatational wave, a simple model schematically shown in Figure 2.4 is generated. The finite element model is 0.1-meter (m) long and has 100 elements in the thickness in order to capture the necessary details of the traveling wave front. Considering the length of the brain is approximately 0.17 m in the anterior-posterior direction, this length of the model is reasonable to reveal potential problems that can take place as stress wave propagates within the brain. Only one element in the transverse direction is required, with the boundary condition which states that all nodes are allowed to move only in the longitudinal direction (that is, the direction of the wave propagation).

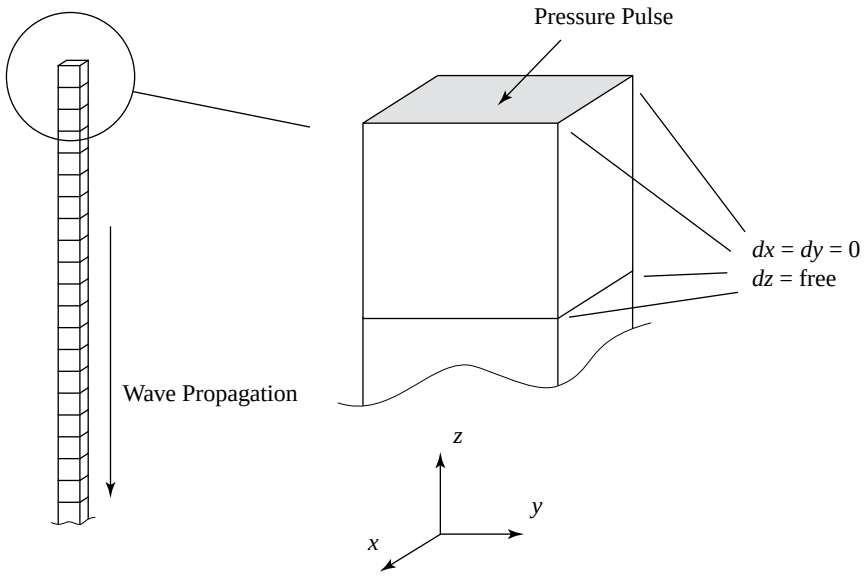

Figure 2.4 Schematic of Finite Element Model for One-Dimensional Wave Propagation Test

The input pressure pulse is a piecewise linear approximation of a sinusoidal function represented by:

$$P(t) = 50\cos\left(\frac{t\pi}{2.0\times10^{-4}} + \pi\right) + 50,\ 0 < t < 4.0\times10^{-4}$$

which has the peak pressure of 100 Pa (see Figure 2.5). From the wave propagation speed the calculated arrival time for the wave on the bottom is 0.00421 second, and the peak particle velocity is calculated from equation (2-89) to be 0.00405 m/s.

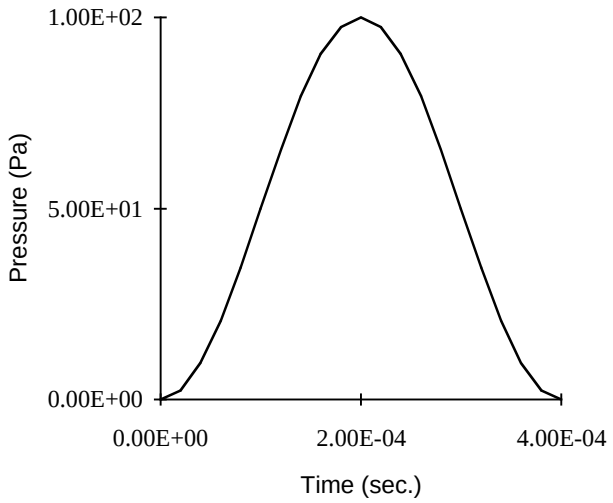

Figure 2.5 Input Pressure Pulse

The time histories of z stress and z particle velocity are recorded at eleven uniformly distributed points along the z axis, and plotted in the Figures 2.6 and 2.7, respectively. All eleven histories are superimposed on a single graph, with time zero taken to be the initiation of the loading pulse. The first valley corresponds to the node at the top, and second, the second node down along the z axis, and so forth.

In Figure 2.6, it can be seen that the z stress faithfully reproduces the sinusoidal pressure input with the peak value of approximately 100 Pa for the duration of close to 4.0×10^{-4} second. However, the next valley which corresponds to the second node, and third, and so forth, show that the peak magnitude decreases and at the same time the pulse form widens. This is believed to be caused by the application of artificial viscosity, which is confirmed later. The 11th and very weak valley corresponds to the node at the bottom. From the wave propagation velocity the estimated arrival time of the wave at the bottom of the plate is 4.21×10^{-3} second. It can be seen that the 11th valley starts to take form slightly after 4.1×10^{-3} second. Incidentally, the boundary condition states that this node is supposed to be stress-free, therefore this non-zero response is caused by numerical error. The same arrival time of the wave can be seen in Figure 2.7 as well.

In Figure 2.7, the particle velocity in the z direction is plotted. The peak z particle velocity is

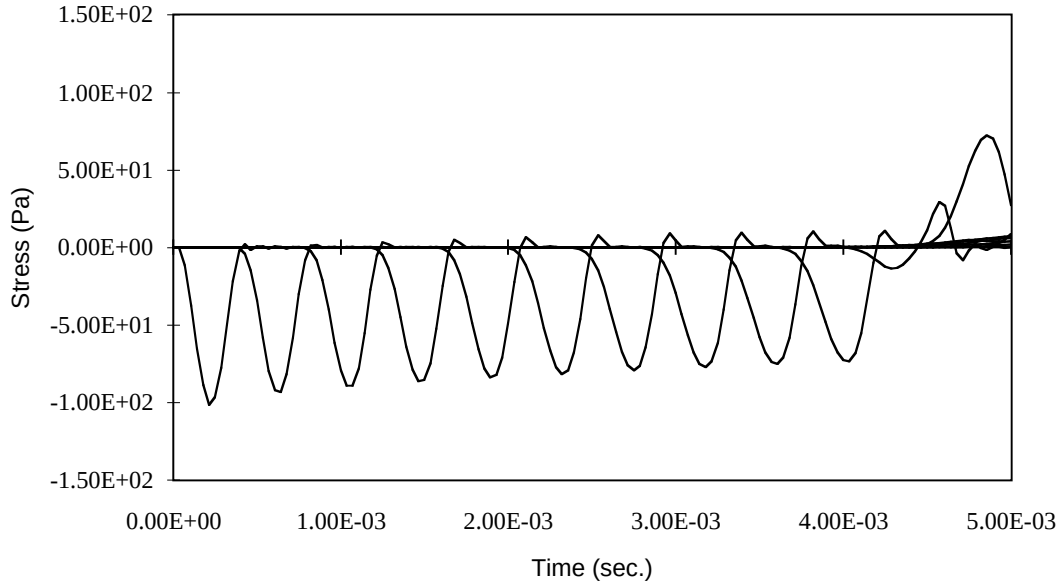

Figure 2.6 Z Stress History Along the Z Axis in Elastic Medium

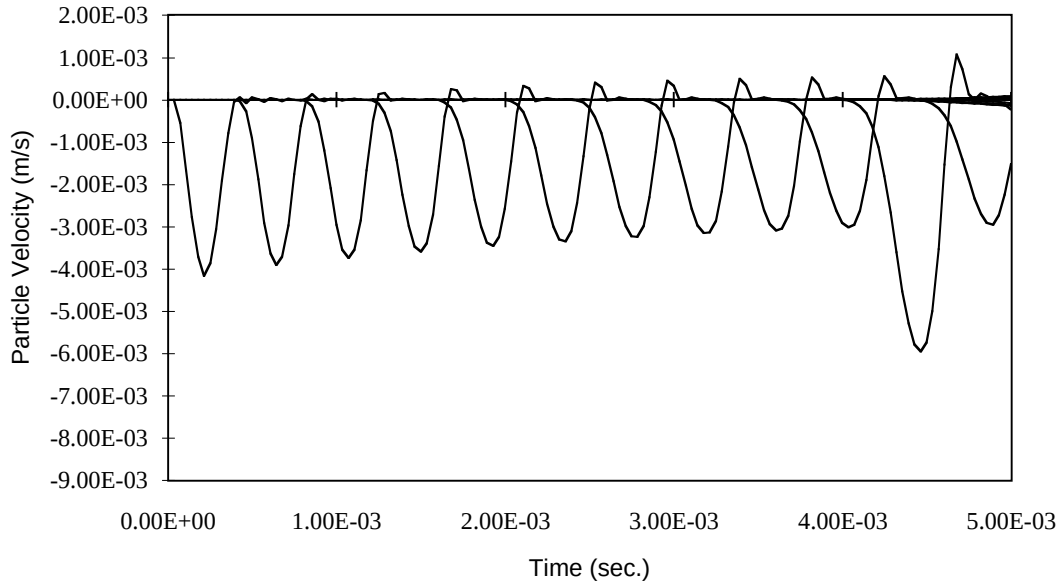

Figure 2.7 Z Particle Velocity History Along the Z Axis in Elastic Medium

4.16×10^{-3} m/s which is comparable to what is obtained analytically. As is seen in Figure 2.6, the z velocity pulse show that same tendency of decrease of the peak magnitude and widening of the pulse as the wave travels down the z axis. The 11th valley which corresponds to the node at the bottom of the plate, shows the characteristic doubling of

magnitude as the wave reflects off of a free surface by comparing against the valley directly preceding it.

The reason for the degradation of the pulse is the default artificial viscosity used in DYNA3D. DYNA3D was originally designed to analyze situations where shock formation in materials was of great concern. In reality a discontinuity characterized by a sudden change in variables (pressure, density and so forth) is formed across a shock front, which numerical simulation methods like the finite element method have difficulties handling. The artificial viscosity, which is a fictitious entity, “smears” this discontinuity over several elements so that it can be handled in a more numerically stable manner. However, the observed results suggest that the system is unnecessarily and inappropriately damped and therefore produces less stress than anticipated in areas away from the load. Since at this point the generation of shock is of no concern, it is decided to “turn off” the artificial viscosity. DYNA3D uses a quadratic form of artificial bulk viscosity to treat the shock phenomena. This viscosity can be defined by two coefficients, and the user can practically turn off the artificial viscosity by giving small coefficient values, since DYNA3D automatically assigns the default values if those coefficients are exactly zero. In this case an arbitrarily small number, 1.0×10^{-10}, is assigned for both coefficients.

Figures 2.8 and 2.9 are the results of the second analysis, which show the same phenomena as in Figures 2.6 and 2.7, but without the decrease in magnitude nor widening of the pulse form. Therefore it is recommended that the artificial viscosity be turned off unless shock is of concern.

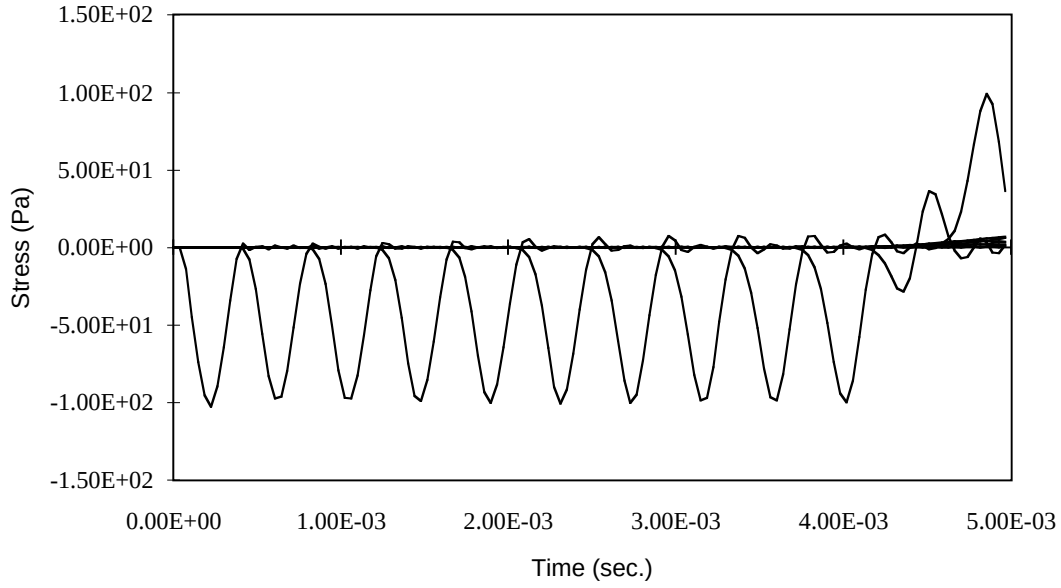

Figure 2.8 Z Stress History Along the Z Axis Without Artificial Viscosity in Elastic Medium

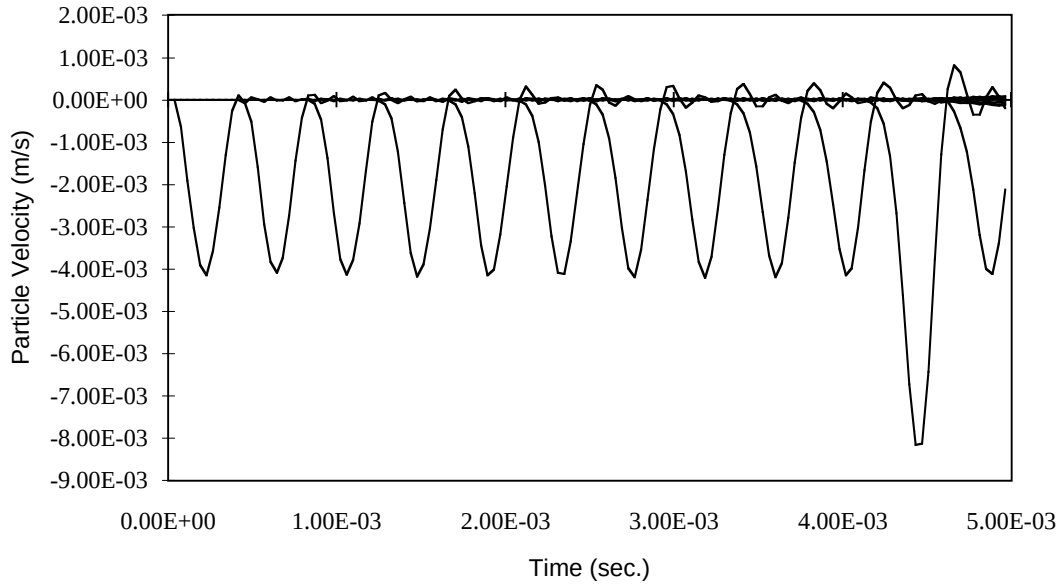

Figure 2.9 Z Particle Velocity History Along the Z Axis Without Artificial Viscosity in Elastic Medium

2.3.2 Viscoelastic Wave Propagation

From [19], the uniaxial relaxation function is approximated by

$$Y(t) = 0.347 + (0.95 - 0.347)e^{(-0.111t)} \text{ (psi)}$$

which is shown against the experimental results in Figure 2.10.

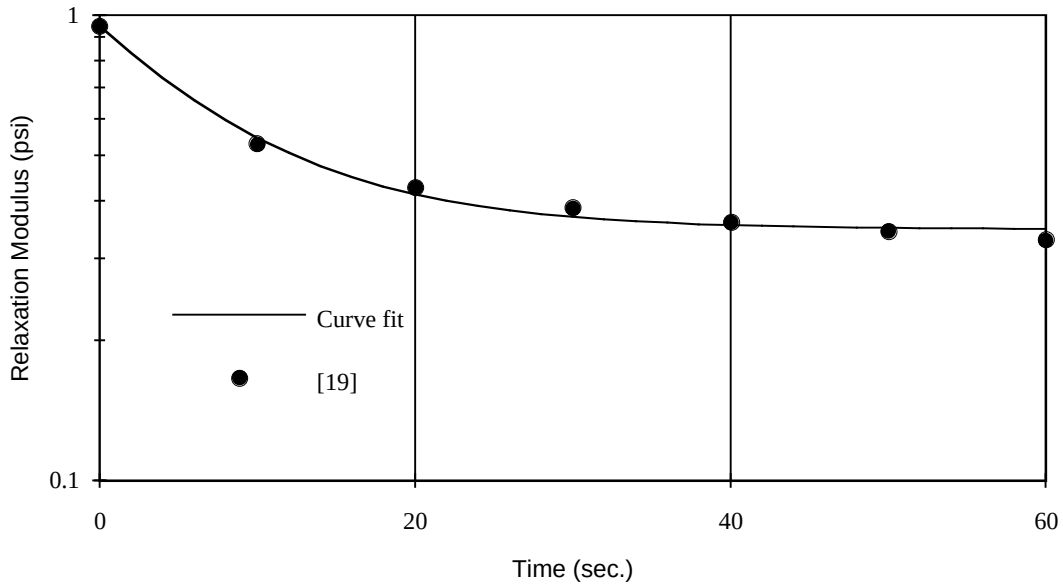

Figure 2.10 Relaxation Modulus for Human Brain

This equation is determined by the least square curve fit of the relaxation curve for the human brain, and short term relaxation modulus reported by the authors (0.95 psi). This equation is converted into the SI unit

$$Y(t) = 2.39 \times 10^3 + \left(6.55 \times 10^3 - 2.39 \times 10^3\right)e^{(-0.111t)} \text{ (Pa).}$$

The uniaxial relaxation modulus has the same form shown in (2-64),

$$Y(t) = q_0 + \left(\frac{q_1}{p_1} - q_0 \right) e^{(-t/p_1)}.$$

From this the values for q_0, q_1 and p_1 are determined as

$$q_0 = 2.39 \times 10^3$$
$$q_1 = 5.90 \times 10^4$$
$$p_1 = 9.01.$$

Substituting these values in (2-51) the coefficients for the shear relaxation modulus p_1', q_0' and q_1' can be obtained. The bulk modulus $K = 2.07$ GPa reported in McElhaney *et al.* [50] is chosen for the calculation.

Therefore,

$$q_0' = 1.59 \times 10^3$$
$$q_1' = 3.93 \times 10^4$$
$$p_1' = 9.01.$$

From equation (2-64), the deviatoric relaxation modulus is

$$G'(t) = 1.59 \times 10^3 + \left(4.37 \times 10^3 - 1.59 \times 10^3\right) e^{(-0.111t)} \text{ (Pa)}.$$

However, $G'(t)$ is a relaxation modulus that is defined between the deviatoric stress and *tensorial* deviatoric strain, the engineering shear relaxation modulus is

$$G(t) = 7.97 \times 10^2 + \left(2.18 \times 10^3 - 7.97 \times 10^2\right) e^{(-0.111t)} \text{ (Pa)}.$$

This shows that the short terms shear modulus G_0 is 2.18×10^3 Pa, the long term shear modulus G_∞, 7.97×10^2 Pa and the decay constant β is 0.111.

Those values, along with the same density used in the elastic test described above, are used to define Material Type 6 (Viscoelasticity) in DYNA3D.

In this case the number of elements along the wave propagation is increased to 500 in order to accommodate shorter pulse period which is needed for this "stiffer" material. The input sinusoidal pressure pulse has the same form as the one used in the elastic test, but the period of 8.0×10^{-6} second, which corresponds to 125.0 kHz. The frequency ω is expressed in circular form, therefore, ω is 785.4×10^{3} rad./s. From (2-109) f is calculated to be 557.0, which gives 1410.1 m/s as the wave propagation velocity at this particular frequency, and the wave arrives at the bottom at 7.09×10^{-4} second. The decay constant α is calculated to be -3.52×10^{-11}, therefore the dissipation is minimal. The phase shift between the particle velocity and stress is given by (2-120) and calculated to be 6.32×10^{-14}, which indicates that they are practically synchronized (in phase). The equation (2-119) gives the proportional constant between the stress and particle velocity magnitudes, which in this case is 1.47×10^{6}. From this the peak particle velocity value is calculated to be 6.82×10^{-5} m/s.

The results of this viscoelastic wave propagation were shown in Figures 2.11 and 2.12 in the form of stress and the particle velocity histories in the direction of the wave travel.

It is seen from both figures that the arrival of the wave at the bottom, indicated by the start of the 11th valley, is around 7.1×10^{-5} second, which matches the analytical solution. In addition, the stress wave form in Figure 2.11 indicates that the material faithfully responds to the pressure pulse, as predicted from the traction boundary conditions, and the same pulse form is maintained throughout, as expected from the very small value of α..

Figure 2.12 shows the particle velocity in synch with the stress pulse, having the peak value of 6.79×10^{-5} m/s, which is within 5% of the predicted value.

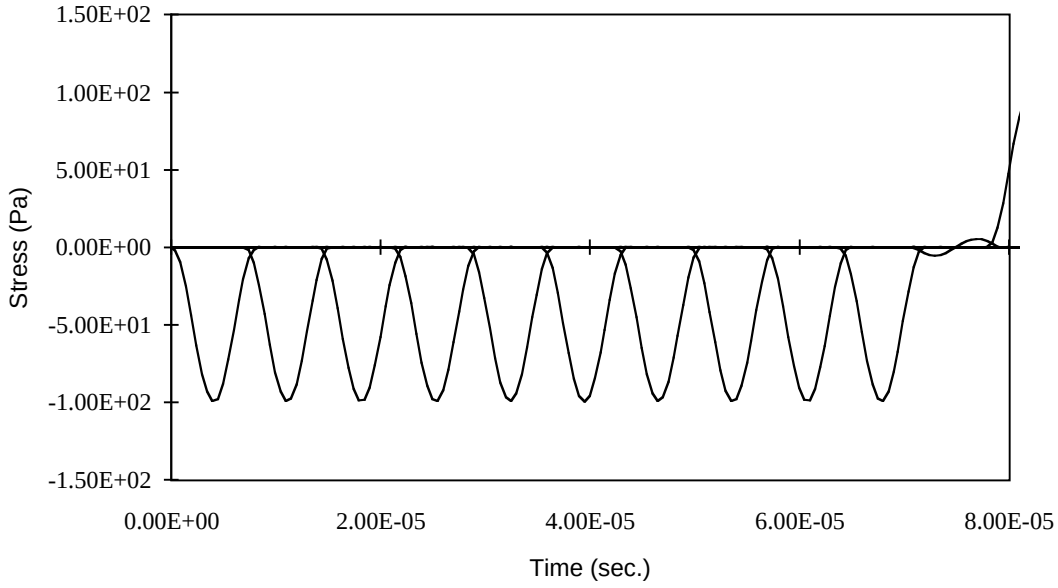

Figure 2.11 Z Stress History Along the Z Axis in Viscoelastic Medium

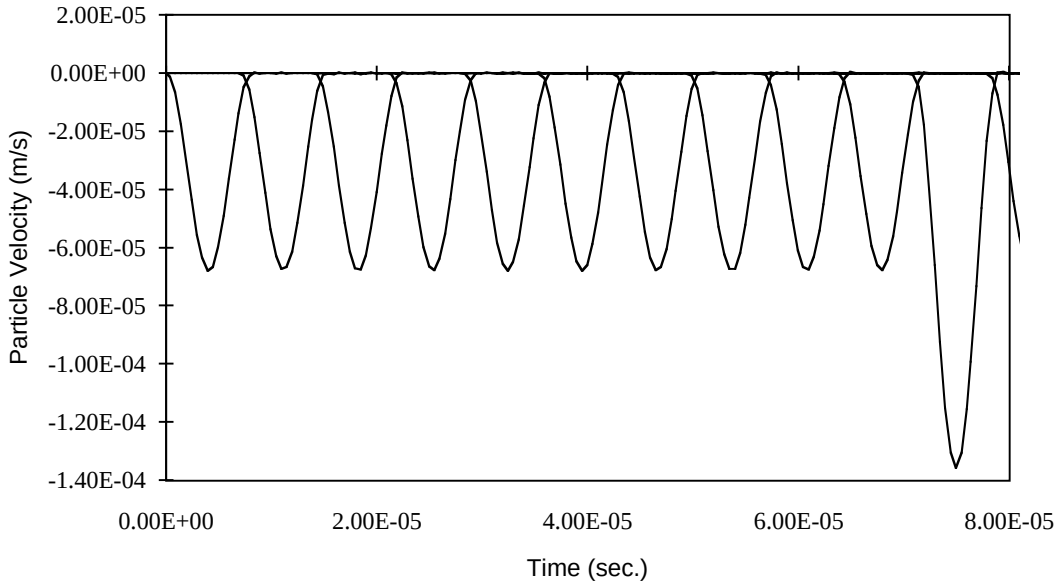

Figure 2.12 Z Particle Velocity History Along the Z Axis in Viscoelastic Medium

Chapter 3
Simulated Head Model

Before more complex finite element models of the human head are analyzed, a set of preliminary analyses is performed using a simplified model. The concentric spherical form has been widely used as the simplest possible three-dimensional alternative to the human head since the days when numerical methods were far less prevalent than they are today. Here one such model is constructed to investigate differences in wave propagation effects caused by the choice of material representations.

3.1 Geometry

The dimensions of the simplified concentric spherical model are based on several measurements of the actual human head. The average cranium volume is 1400 cubic centimeters (cc) [25], and the thickness of the cranium is chosen as 9.0 millimeters (mm) [39] (see the description of the skull material properties later). This leads to the interior radius of the simulated cranium to be 69.4 mm, and the exterior, 78.4 mm. The average weight of the brain is 1.36 kg [51], and with the average specific gravity of 1.036 [51], it occupies 1313 cc in the cranium. This leaves 87 cc of empty space which, in actuality, is filled with cerebrospinal fluid (CSF). This value is smaller than 140 milliliters (ml) reported in [25]. If 87 cc is assumed, the thickness of the CSF layer is roughly 1.44 mm (volume divided by the interior surface of the cranium), and if 140 cc is assumed, the thickness will be 2.31 mm. However, at this stage of the study it is decided not to incorporate such thin feature since it leads to unnecessarily small time integration steps. For the same reason, the skull is treated as a one-layer structure.

Through visual inspection in the Visible Human Dataset images the thickness of the falx cerebri ranges from 2 to 4 pixels wide. With 0.33 mm-per-pixel resolution, this corresponds

to 0.66 to 1.32 mm. The dura that is adhered to the skull is not readily discernible in the images. Here the dura is assumed to have a uniform thickness of 1.0 mm, and modeled as membrane elements. The model, which is quarter-symmetric, is shown in Figure 3.1. The total mass of the quarter-symmetry system, with the density values described below, is 0.601 kg which corresponds to 2.404 kg for the whole sphere. This value is approximately half of the weight of the standard adult human head, which is generally considered to be 4.5 kg. The discrepancy is due to missing parts such as facial features and scalp.

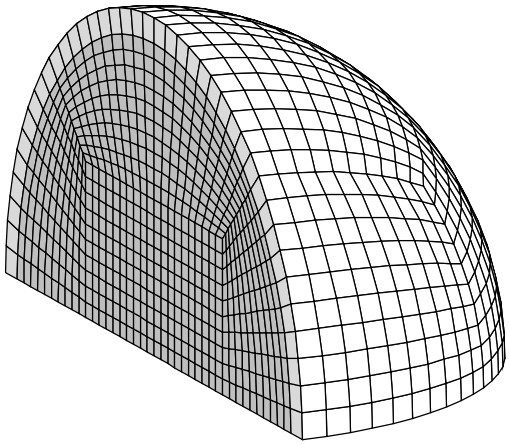

Figure 3.1 Quarter-Symmetric Pseudo-Head Model

3.2 Material Constitutive Laws

Two linear viscoelastic and four linear elastic constitutive models are employed to investigate the effect of tissue properties on stress wave propagation in the brain. These models are summarized in Table 3.1.

Table 3.1 Material Properties For Examined Cases

Case	*Bulk Modulus (Pa)*	*Relaxation Modulus (Pa)*		
VE1	2.07×10^{9}	$7.97\times10^{2}+\left(2.18\times10^{3}-7.97\times10^{2}\right)e^{-0.110t}$		
VE2	1.28×10^{8}	$1.68\times10^{5}+\left(5.28\times10^{5}-1.68\times10^{5}\right)e^{-35t}$		
		Young's Modulus (Pa)	*Poisson's Ratio*	*Shear Modulus (Pa)*
E1	2.07×10^{9}	66.7×10^{3}	0.49999462	2.22×10^{4}
E2	2.07×10^{9}	71.7×10^{3}	0.49999422	2.39×10^{4}
E3	2.06×10^{9}	6.55×10^{3}	0.49999947	2.18×10^{3}
E4	2.10×10^{9}	2.39×10^{3}	0.49999981	7.97×10^{2}

The first linear viscoelastic characterization (case VE1) is based on the uniaxial stress relaxation test performed by [19], and the bulk modulus of $K = 2.068\times10^{9}$ Pa is from McElhaney *et al.* [50]. This model is characterized by the shear relaxation modulus $G(t)$,

$$G(t) = 7.97\times10^{2} + \left(2.18\times10^{2} - 7.97\times10^{2}\right)e^{-0.110t} \text{ Pa.}$$

This is the same material linear viscoelastic model derived in the previous chapter for wave propagation validation.

The other viscoelastic model, case VE2, is the one that was employed in actual finite element applications by Ruan *et al.* [70]. Since the decay constant β is defined with *t* in milliseconds, it is scaled to fit the SI system. For the sake of consistency, the bulk modulus *K* used by the same authors ($K = 1.279\times10^{8}$ Pa, derived from $E = 3.07\times10^{5}$ Pa and $\nu = 0.4996$) is also used. This case is represented by this bulk modulus and the shear relaxation modulus of

$$G(t) = 1.68\times10^{5} + \left(5.28\times10^{5} - 1.68\times10^{5}\right)e^{-35t} \text{ Pa.}$$

The four linear elastic models considered here are presented as potential alternatives for a viscoelastic model. Each case is based on a different argument as to how to "reduce" a linear viscoelastic model to a linear elastic model. Cases E1 and E2 are different interpretations of the vibrational experiments performed by [19], while E3 and E4 are based on the relaxation experiments by [19], through the relaxation modulus derived in the previous chapter. For all

linear elastic cases the same bulk modulus, $K = 2.07$ GPa, is used to calculate Poisson's ratios. As those Poisson's ratios are used in the standard linear elastic model in DYNA3D, the actual bulk moduli used by DYNA3D internally are slightly different due to an insufficient number of significant digits.

The real part of the complex modulus (storage modulus) reported in [19] is used as the Young's modulus in the first linear elastic model (case E1). This approximation was also used by [34], [69] and others. The second linear elastic case, E2, uses the magnitude of the complex modulus reported in [19]. This value defines the stress-strain relation in amplitudes in a vibration test [35].

The Young's moduli for the third and fourth linear elastic representations (cases E3 and E4) use the short-term and long-term moduli, respectively, of the uniaxial relaxation modulus from [19]. In essence these models are "reduced" cases from VE1. Note that VE1 above is represented as the shear relaxation modulus, while E3 and E4 are derived from uniaxial relaxation modulus. The Young's modulus used in case E3 is the stiffness of the linear elastic unit that is in series with the Kelvin unit in the linear three-parameter viscoelastic solid, while case E4 is equivalent to removing the viscous unit.

The density of the brain reported in the literature ranges from 1010 [19], 1036 [35,19], 1040 [87 and others] to 1081 [3] kg/m^3. Here 1036 kg/m^3 is selected.

The density of the skull as a whole ranges from 1411.7 [50], 1610 [12] 1807 [3] to 2030.7 [39] kg/m^3. Khalil and Hubbard [39] used 2940 and 1710 kg/m^3 for the cortical (compact) and trabecular (cancellous) bones, respectively. Duck [12] lists 1990 and 1080 kg/m^3 for the compact and cancellous bones with bone marrow, respectively. If the skull is modeled as a three-layered system, the values from [12] are chosen since the data from [39] appear to be on the high side. If the skull is modeled as a whole (*i.e.* one-layer system), as it is the case for now, the value from the same source is used (1610 kg/m^3).

According to Khalil and Hubbard [39], the Young's modulus $E = 65.0 \times 10^8$ Pa and Poisson's ratio $\nu = 0.2$ are given for the whole skull which, along with thicker-than-usual thickness, are representative of the three-layered counterpart in terms of bending and membrane stiffness.

The density of the dura is given by Barber *et al.* [3] as 1133 kg/m^3. There has not been a

particular mention of Poisson's ratio; here the value reported in Hosey and Liu [34]—0.45—is used.

Galford and McElhaney [19] report that the complex modulus for the dura at 20 Hz is

$$E(i\omega) = 31.51\times10^{6} + 3.45\times10^{6} i \text{ Pa},$$

of which the storage modulus (the real part) is used as the elastic modulus by Hosey and Liu [34]. McElhaney *et al.* [50] has the elastic moduli of $E = 41.55\times10^{6}$ Pa at 0.0666 s^{-1}, $E = 44.33\times10^{6}$ Pa at 0.666 s^{-1} and $E = 60.67\times10^{6}$ Pa at 6.66 s^{-1}. Even though it is clear that the dura exhibits high strain-rate sensitivity, the elastic representation with the highest recorded elastic modulus (60.67×10^{6} Pa) is selected for now.

3.3 Boundary, Initial and Special Conditions

The simplified head system is given an initial velocity of 15.0 meters per second (m/s), and impacted into a stationary rigid wall. This initial velocity is arbitrarily selected as an estimated upper limit of what one might encounter in auto accidents. Appropriate symmetry boundary conditions are applied to ensure the quarter-section response is representative of the entire structure. Otherwise the system is unconstrained. In addition, as indicated in the previous chapter, the artificial viscosity is, for all practical purposes, turned off since shock formation is not expected to occur at the low impact speed considered.

3.4 Results

Three parameters, pressure, maximum shear strain and normal stress in the direction of travel, at three different locations are recorded to observe the differences caused by the selection of material constitutive relations. The three locations selected are; 1) coup site (outermost node on the brain under the impact site), 2) contracoup site (the opposite location from the impact) and 3) pole site (90 degree away from the coup site). Those locations are depicted in Figure 3.2

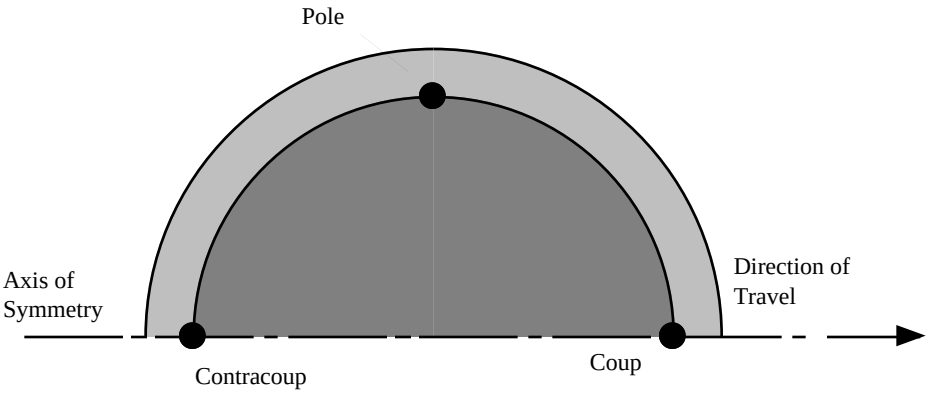

Figure 3.2 Output Locations of Pseudo Head Model

First, some observations are made on the differences between two viscoelastic characterizations. Figure 3.3 shows the pressure history at the coup site. At the first valley, the two responses which may be dominated by the simulated skull, appear almost identical.

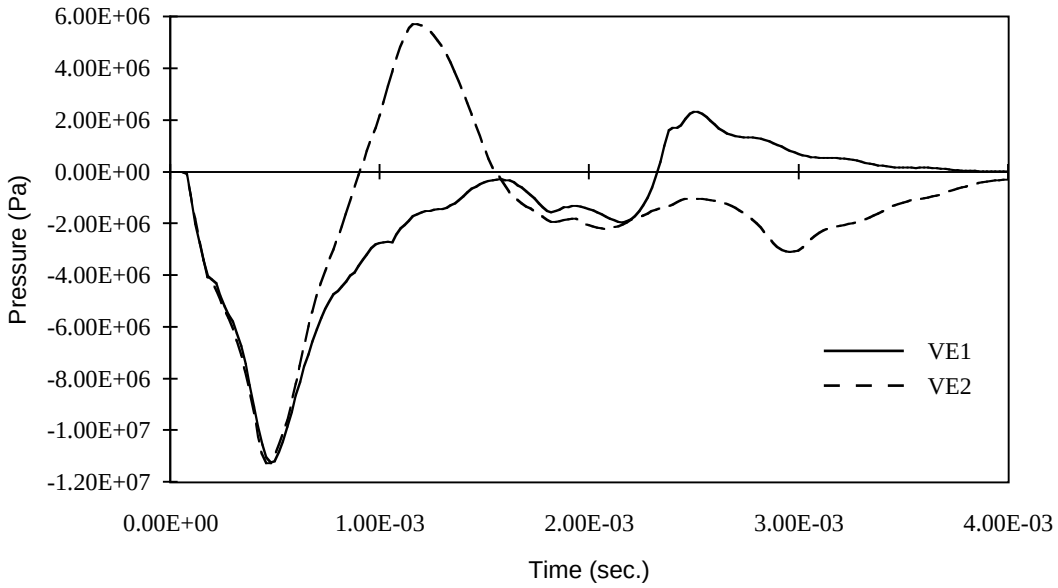

Figure 3.3 Pressure History at Coup Site: Viscoelastic Materials, $V_i = 15$ m/s

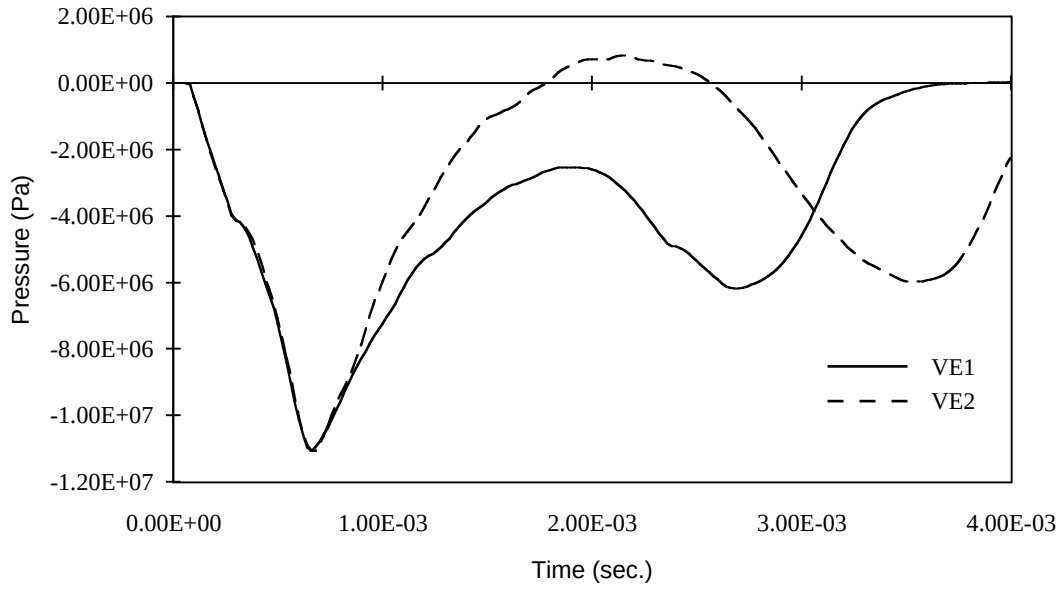

Figure 3.4 Pressure History at Coup Site: Viscoelastic Materials, $V_i = 7.5$ m/s

However, the rebound exhibited by VE2 is far more pronounced than that by VE1, and their responses are markedly different for the remainder of the duration, VE1 returns to positive pressure much later than VE2, and VE2 stays in the negative range after the rebound.

When the same system is analyzed with a different initial velocity (7.5 m/s), the rebound peak from VE2 occurs later than that from VE1. The pressure histories at the contracoup site (Figures 3.5 and 3.6) do not appear to show that trend, however. While VE2's peak magnitude is significantly less and occurs slightly later than VE1 under both initial velocities, VE2 does not rebound any more than VE1.

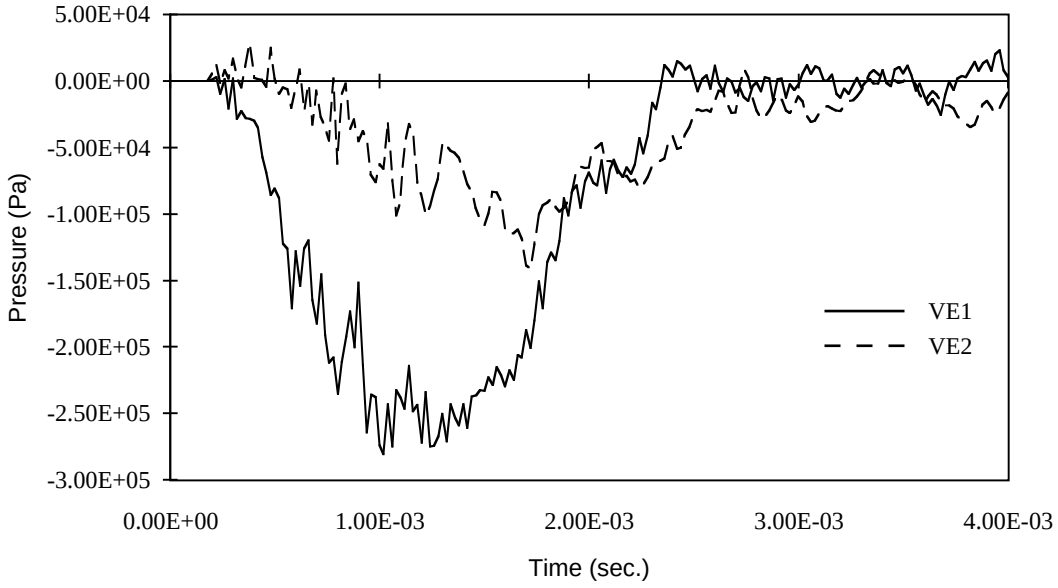

Figure 3.5 Pressure History at Contracoup Site: Viscoelastic Materials, $V_i = 15$ m/s

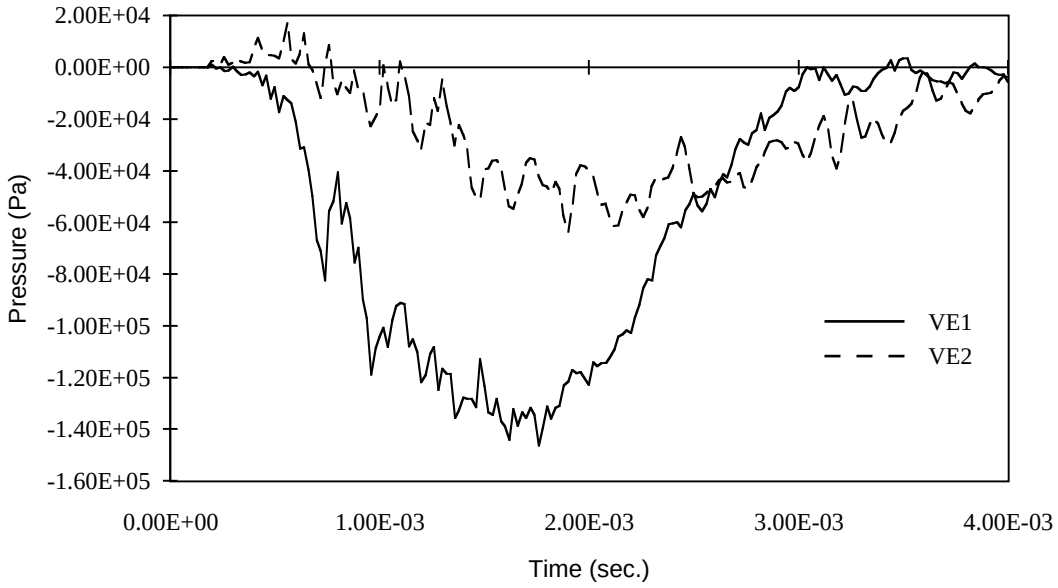

Figure 3.6 Pressure History at Contracoup Site: Viscoelastic Materials, $V_i = 7.5$ m/s

More pronounced differences are observed in the maximum shear strain at the pole site, as shown in Figures 3.7 and 3.8. While VE1 exhibits a very distinctive maximum shear strain peak, VE2's maximum is far less pronounced.

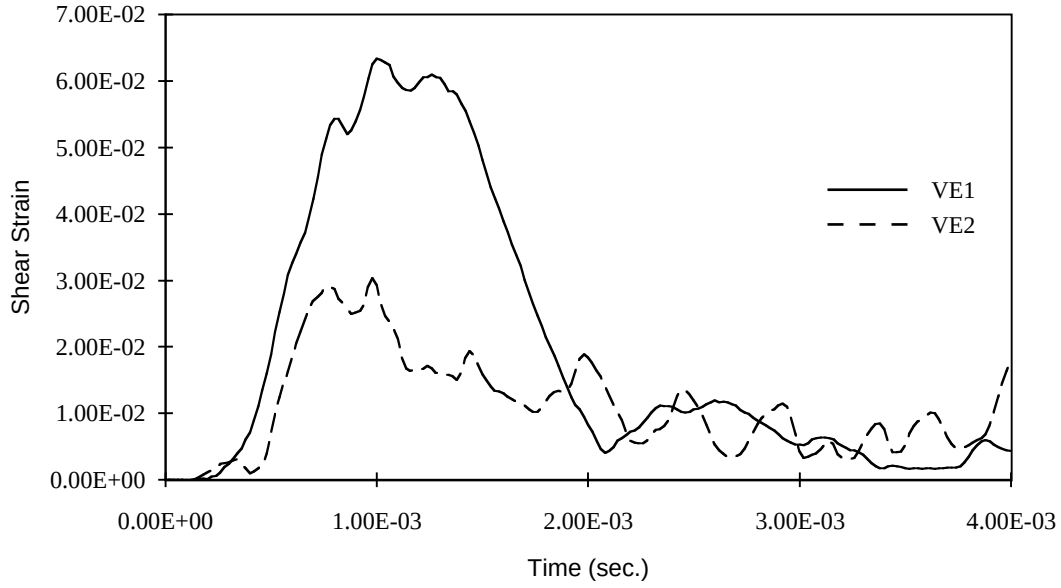

Figure 3.7 Maximum Shear Strain History at Pole Site: Viscoelastic Materials, $V_i = 15$ m/s

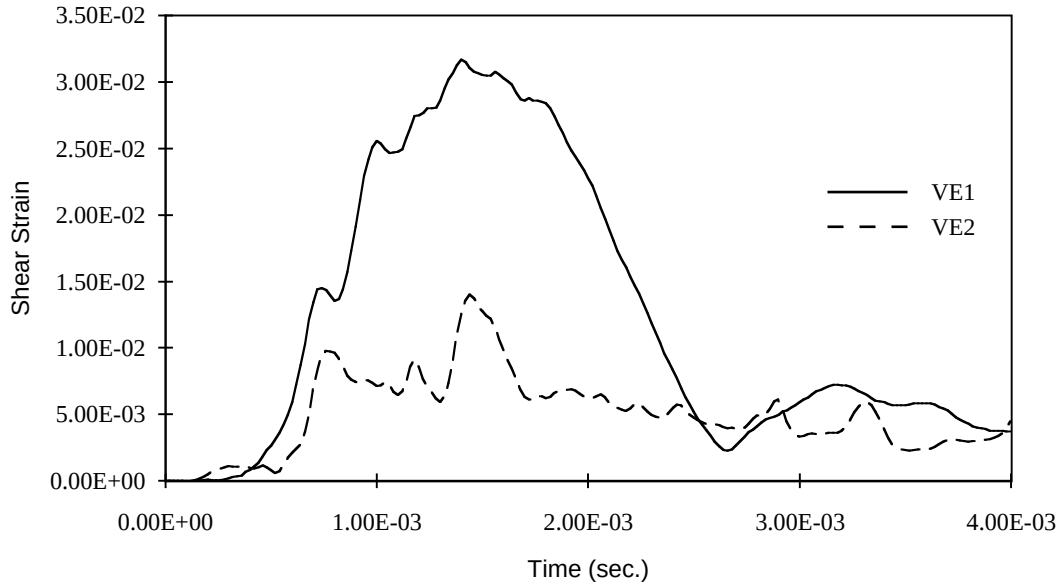

Figure 3.8 Maximum Shear Strain History at Pole Site: Viscoelastic Materials, $V_i = 7.5$ m/s

When the four linear elastic models are compared with VE1, it is found that their responses are nearly identical. It is apparent that in a system where volumetric changes dominate the deformation, as they do in the case under consideration, and the bulk moduli of all constitutive models considered are essentially the same, the results produced are nearly

identical (see Figures 3.9 through 3.12).

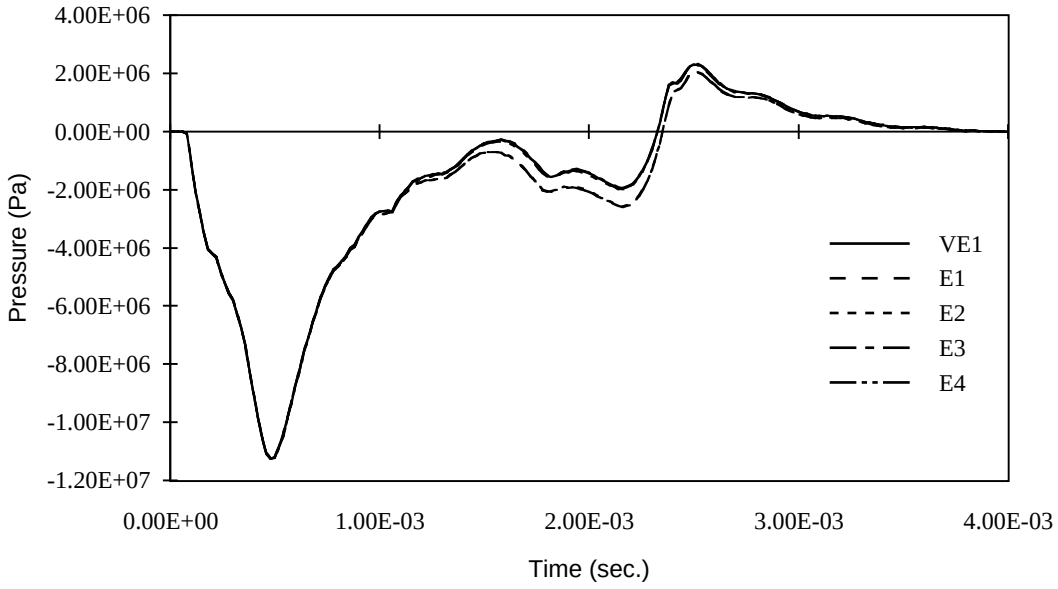

Figure 3.9 Pressure History at Coup Site: Elastic versus Viscoelastic Materials, $V_i = 15$ m/s

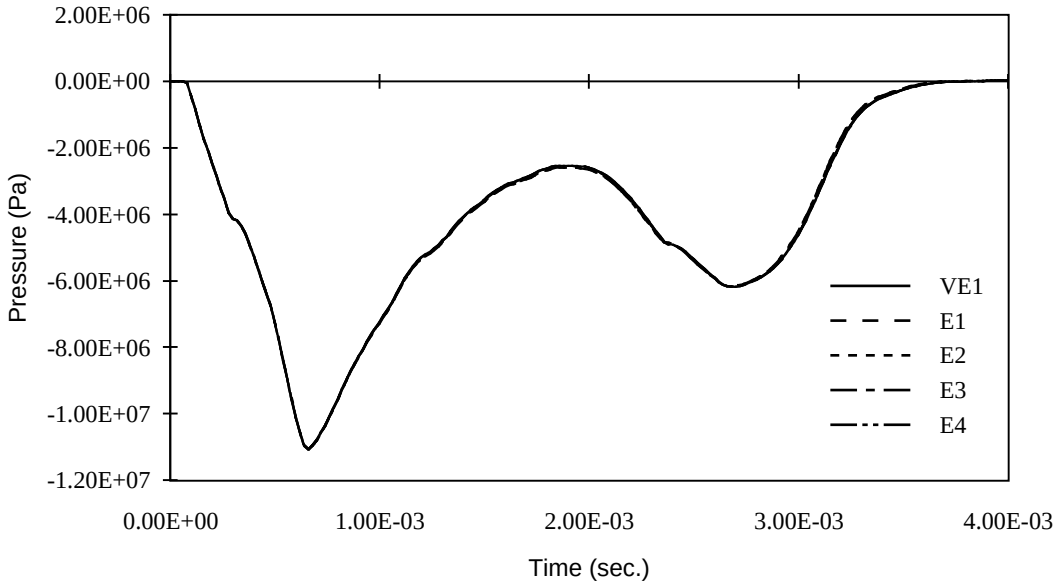

Figure 3.10 Pressure History at Coup Site: Elastic versus Viscoelastic Materials, $V_i = 7.5$ m/s

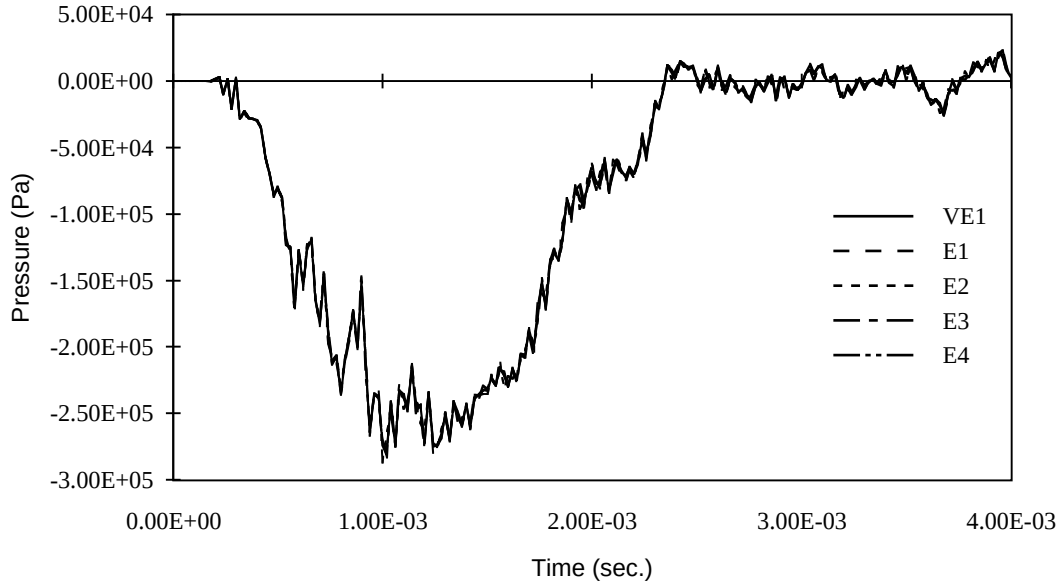

Figure 3.11 Pressure History at Contracoup Site: Elastic versus Viscoelastic Materials, $V_i = 15$ m/s

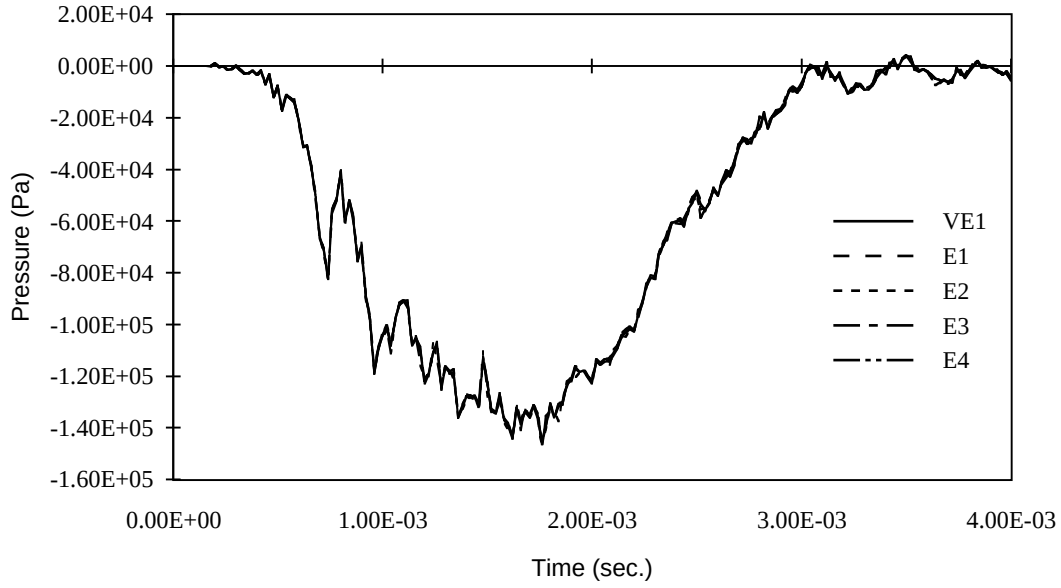

Figure 3.12 Pressure History at Contracoup Site: Elastic versus Viscoelastic Materials, $V_i = 7.5$ m/s

Due to the boundary and initial conditions, large distortion, instead of deformation, is expected at the pole site. Figures 3.13 and 3.14 give the maximum shear strain histories at the pole. It can be observed that E1 and E2 deviate from the viscoelastic solution after the initial rise, and underpredict the peak maximum shear strain by 15 to 30 percent relative to the

viscoelastic solution. In addition, both the E1 and E2 solutions exhibit a second strong peak which is not observed from VE1. E4, on the other hand, slightly overshoots the peak produced by VE1, but nonetheless produces similar results.

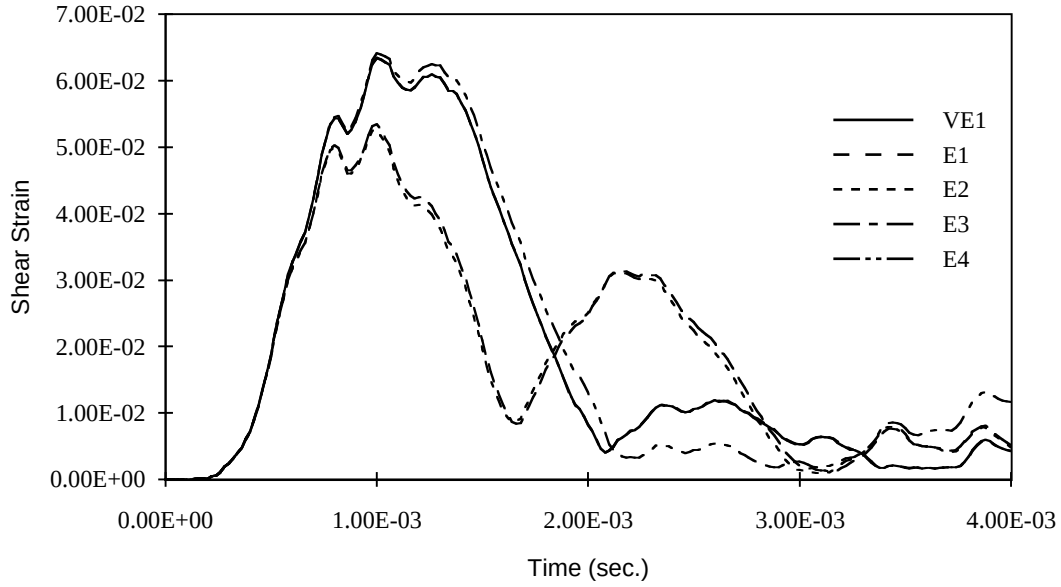

Figure 3.13 Maximum Shear Strain at Pole Site: Elastic versus Viscoelastic Materials, $V_i = 15$ m/s

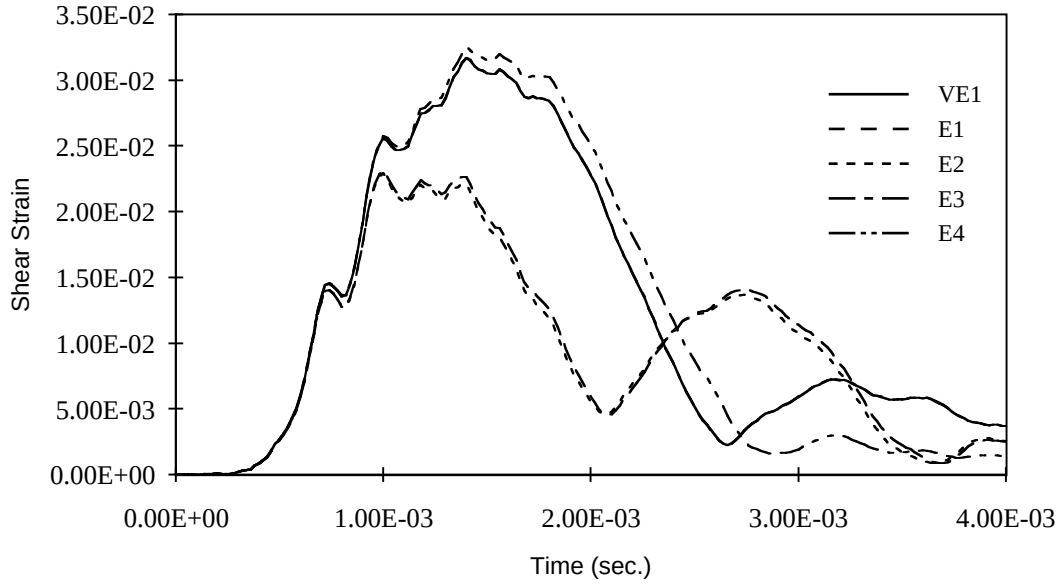

Figure 3.14 Maximum Shear Strain at Pole Site: Elastic versus Viscoelastic Materials, $V_i = 7.5$ m/s

One important finding here is that the E3 solution very nearly matches the VE1 solution (they are almost indistinguishable in the figures). E3 is an elastic model with a Young's modulus equal to the short-term modulus from [19] and a Poisson's ratio that was chosen to give a bulk modulus nearly identical to that used in VE1. It is clear that E3 and VE1 (or any of the other elastic materials with similar bulk moduli) produce identical results in the spherical components. The closeness of the solutions in the deviatoric components (which, combined with the spherical components produces the overall response) is due to the fact that VE1 exhibits a shear (deviatoric) response that can be approximated with a linear elastic model having a shear modulus about equal to the instantaneous shear modulus of the viscoelastic material.

In order to clarify this, the shear properties of those materials are compared graphically. The complex shear modulus of the three-parameter linear viscoelastic solid has the same form as the uniaxial counterpart as shown in the previous chapter;

$$\Gamma(i\omega) = \frac{q_0' + p_1' q_1' \omega^2}{1 + p_1'^2 \omega^2} + \frac{q_1' \omega - p_1' q_0' \omega}{1 + p_1'^2 \omega^2} i, \tag{3.1}$$

and the magnitude of this complex modulus is

$$\left|\Gamma(i\omega)\right| = \sqrt{\frac{q_0'^2 + q_1'^2 \omega^2}{1 + p_1'^2 \omega^2}}. \tag{3.2}$$

This magnitude of the complex modulus, defined by the deviatoric parameters q_0', q_1' and p_1', relates the magnitudes of tensorial shear strain and stress. When the engineering notation is called for, this value is multiplied by 0.5. When $\frac{1}{2}\left|\Gamma(i\omega)\right|$ and G calculated from the given E and ν are plotted against frequency, the result is shown in Figure 3.15. Naturally all linear elastic models have no frequency or strain rate sensitivity , thus appear as straight lines.

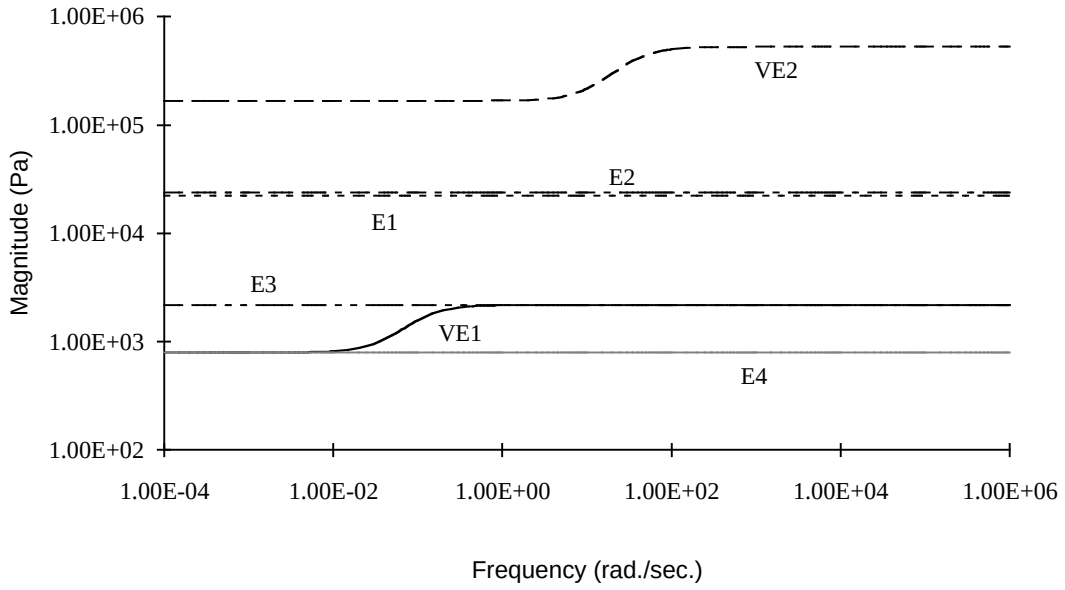

Figure 3.15 Magnitudes of Complex and Shear Moduli against Frequency

As can be seen, in high frequency ranges, which represent high strain-rate as encountered in this series of runs, it is clear that both cases VE1 and E3 exhibit the same shear characteristics.

In conclusion for this series of analyses using the pseudo-head model, the following points are deduced. First, the three-parameter linear viscoelastic model derived for this study is substantially different from what has been used in the literature. This is clear from somewhat "theoretical" point of view, such as shown in Figure 3.15, but also from "application" side, as demonstrated by the pseudo-head test.

Secondly, under certain conditions, it is possible to substitute a three-parameter linear viscoelastic material with a linear elastic model. However, clear understanding must be made regarding the specific viscoelastic characteristics and situation being analyzed in order to accomplish this. More explicitly, it must be known at which frequency range the three-parameter model can be approximated as pseudo-linear elastic, and whether or not the scenario to be analyzed falls into this frequency range. Reviewing the subject on the frequency-dependency of the three-parameter model in the previous chapter, this assumption can only be made with the short-term modulus in high frequency ranges, and long-term modulus in low frequency ranges. Given the amount of preplanning required to examine these conditions, however, using a linear elastic model as a substitute for a three-parameter

viscoelastic solid hardly constitutes as “simplification.”

Lastly, this characterization derived for this study may not be suitable for high-strain rate scenarios, as encountered in automobile accidents. Galford and McElhaney’s relaxation experiments may be a good starting point, but experiments which span up to 60 seconds will not provide meaningful information when the constitutive laws derived from them are used in much shorter time periods.

One note that must be made at this end of this chapter is that when a linear elastic material is chosen to simulate near incompressibility, the selection of the value of Poisson’s ratio must be made extremely carefully. From a simple relation between elastic constants it can be shown that Poisson’s ratio for the isotropic linear elastic material must be less than 0.5. When the bulk modulus is obtained from Young’s modulus and Poisson’s ratio, as Poisson’s ratio approaches its upper limit the bulk modulus becomes highly sensitive to a small change in Poisson’s ratio (this can be shown by plotting a dimensionless parameter $\frac{K}{E}$ against Poisson’s ratio). For example, even if Poisson’s ratio of 0.49999 is selected, which may be conventionally considered incompressible, the results will deviate from what are observed with more “accurate” Poisson’s ratios. Those results are shown in Figures 3.16 and 3.17.

DYNA3D treats all non-integer variables as double precision, and is fully capable of handling as many digits as provided in the material property fields. However, considering the sensitivity of the bulk modulus on Poisson’s ratio in the vicinity of its upper limit, using the simple linear elastic model, for which the Young’s modulus and Poisson’s ratio are defined, does not appear to be a sensible method. Another linear elastic model is available in DYNA3D where both bulk and shear moduli are directly entered, and use of this model is recommended.

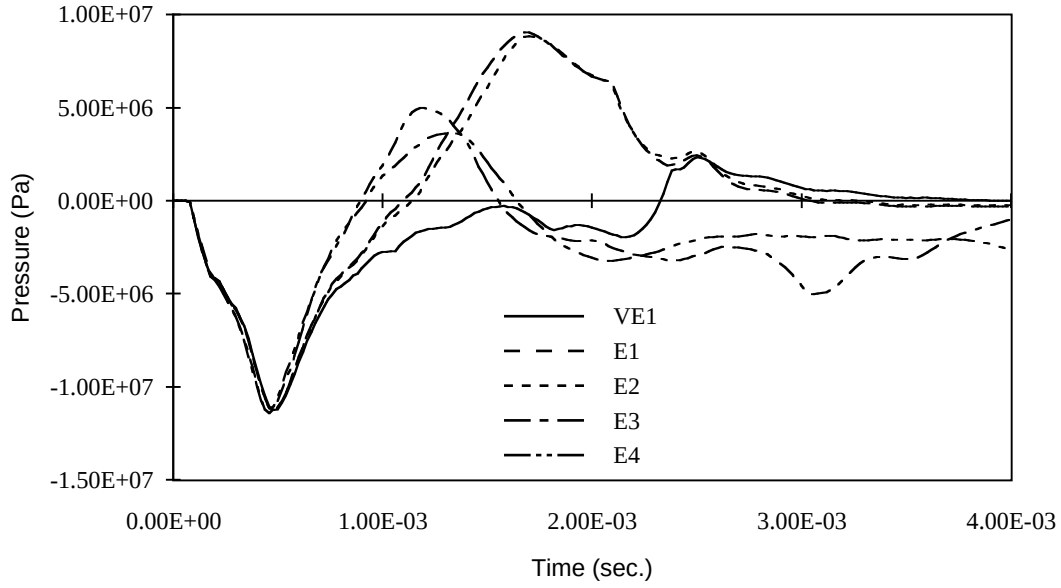

Figure 3.16 Pressure History at Coup Site: Elastic versus Viscoelastic Materials, with Poisson's Ratio = 0.49999, $V_i = 15$ m/s

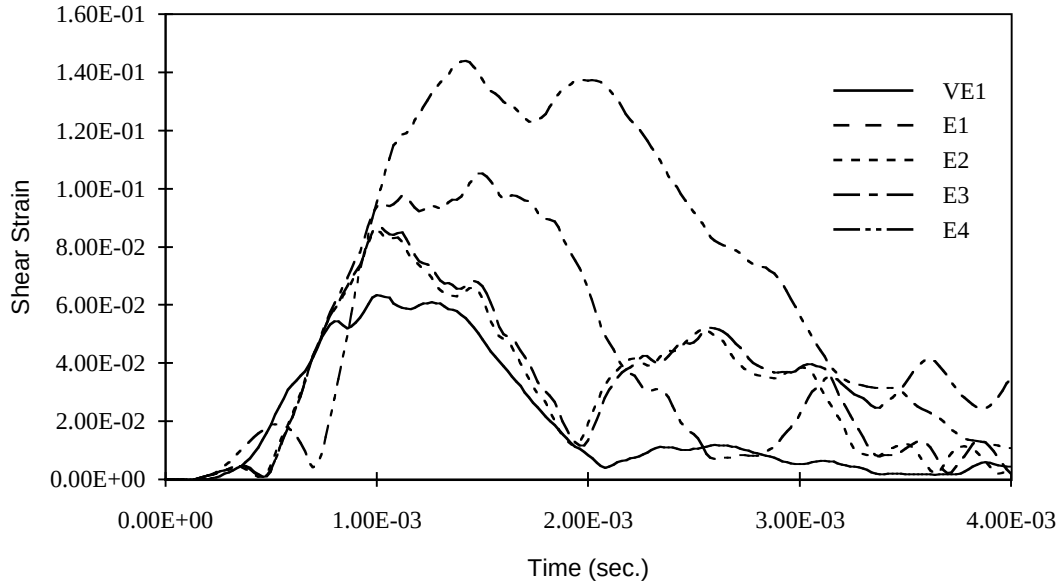

Figure 3.17 Maximum Shear Strain at Pole Site: Elastic versus Viscoelastic Materials, with Poisson's Ratio = 0.49999, $V_i = 15$ m/s

Chapter 4
Injury Theory Assessment

4.1 Purposes

As described in the literature review, a number of finite element models of the human head have been developed for the purpose of analyzing its dynamics under impact or impulse loading. Normally certain engineering parameters such as acceleration, pressure and shear strain histories are examined as head injury criteria. In particular, resultant acceleration history measured at the center of gravity (CG) of the occupant's head is used to compute the Head Injury Criterion (HIC), one of the criteria employed by the United States Government to assess passenger vehicle safety.

The problem of using a finite element model of the human head in such application is two-fold; first, although the finite element models' geometry has been improved over the years, the material constitutive models of the components in the head, especially of the brain, have been somewhat neglected. When these finite element models are used as a injury-prediction tool, this negligence nearly invalidates the results since different brain material constitutive models are likely to produce different engineering parameters.

Therefore, it is important to understand how those parameters can be affected when different material representations for the brain are used. This will illustrate the significance of brain material characterization, and reveal the sensitivity of certain parameters, including HIC, with respect to the differences in brain material properties. At the same time, it will clarify to what extent today's finite element models can be used for this purpose. It is important to understand the limitation of those models imposed by the level of uncertainty in the knowledge of material constitutive relations.

The second problem is that it is not altogether clear as to how HIC relates to the actual dynamics inside the head. The official protocol for assessing a passenger vehicle's safety requires HIC be calculated from the resultant acceleration history measured at the CG of a dummy's head. However, when physical surrogates such as cadavers or volunteers are employed for acceleration/deceleration experiments, their head acceleration histories are usually measured on the side of the head, approximately at the lateral projection of the head CG [57] (assuming that the dominant head motion is in the sagittal plane). Then when a finite element model of a human head, as opposed to that of a dummy, is used to obtain HIC, it is naturally calculated from the acceleration history measured at the head CG [70], owing to the manipulability of the mathematical method. Consequently, there is a need to investigate how those different methods of measuring acceleration history affect HIC, and how they relate to the internal dynamics of the head.

4.2 Finite Element Model

4.2.1 Geometry

The finite element model used in this study is based on the Visible Human Dataset™ (VHD) made available by the National Library of Medicine. The VHD is a result of the collaboration between the National Library of Medicine and the University of Colorado School of Medicine, which was to produce a complete library of digital volumetric image data of a normal human [70]. So far two sets of data have been produced; the Visible Human Male and the Visible Human Female. The Male dataset was completed first in 1994, and the images from this dataset is used for this study. For a brief description of how the images are transformed into a three-dimensional computer model, see Appendix.

Since this study is focused on material constitutive laws, further simplification on the model is performed so that iterative calculations are feasible. First, the facial features are eliminated. Thus the main framework of the model is to have the cranial content itself and a shell-like structure which represents a modified skull, to enclose cranial content. In addition, the cerebrospinal fluid (CSF) layer has been eliminated. While it is generally believed that CSF

functions as a protective buffer [8], it is feared that its inclusion in the model will unnecessarily increase computational cost. Since the model does not contain the skin layer, another potential protective layer, it is noted that this model may lack realistic protective faculty.

The resulting brain, which fills the cranial cavity completely, is 1375 cc in volume. The average weight of the human brain is 1.36 kg [51] and using the density of 1036 kg/m^3 [12], the model's volume which includes the CSF, is quite reasonable.

The model's simplicity also means that it is significantly lighter than the real head. In order to compensate for the loss, two sets of discrete masses are added to the bottom of the model to approximate the facial features and neck. The amount of mass is described in the following section.

The impactor's shape and size are arbitrarily defined; it is a right cylinder with a diameter of 40 mm by length of 70 mm.

The head model and impactor are shown in Figure 4.1.

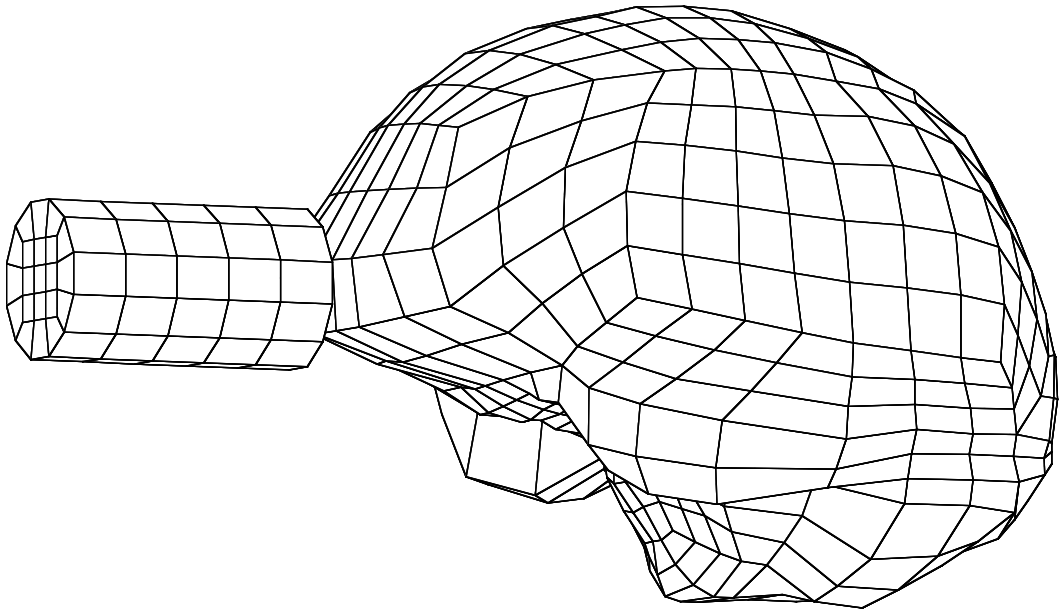

Figure 4.1 Finite Element Head Model and Impactor

4.2.2 Material Constitutive Laws

The skull in this case, once again, is treated as a one-layer system, and is assumed to be linear elastic. The mechanical properties for the skull are adopted from McElhaney *et al.* [50]. Isotropy is also assumed even though it appears that the skull may be transversely isotropic, having different material properties in the tangential and radial directions. The Young's modulus is assumed to be the average of three values—compressive tangential and radial, and tensile tangential moduli. The density for the whole skull from [50] is used.

Both linear viscoelastic and linear elastic representations are used for the brain. In addition to the two linear viscoelastic models examined in the previous Chapter (VE1 and VE2), three more models are studied. The first additional model (labeled as VE3) was reported in Estes [57]. Through compression tests on brain specimens his interpretation of the results is represented by,

$$E_1 = 4.00 \text{ psi}$$

$$E_2 = 1.89 \text{ psi}$$

$$\eta_2 = 0.315 \text{ lb-sec./in}^2.$$

In the SI unit,

$$E_1 = 27.58 \times 10^3 \text{ Pa}$$

$$E_2 = 13.03 \times 10^3 \text{ Pa}$$

$$\eta_2 = 2.17 \times 10^3 \text{ Pa-sec.}$$

which lead to

$$p_1 = 0.0535$$

$$q_0 = 8.85 \times 10^3$$

$$q_1 = 1.475 \times 10^3 .$$

Even though Estes assumed the brain to be incompressible, in order to calculate deviatoric parameters, a bulk modulus of $K = 2.068 \times 10^9$ Pa [51] is used. This results in

$$p_1' = 0.0535$$

$$q_0' = 5.90 \times 10^3$$

$$q_1' = 9.83 \times 10^2 .$$

Another three-parameter linear viscoelastic solid model (labeled as VE4) is reported by Donnelly and Medige [12]. They performed dynamic shear experiments using a parallel-plate apparatus. Though their results are fitted with a non-linear derivative of the three-parameter viscoelastic solid model, here the core three-parameter model is used, whose characteristics are represented by

$$p_1' = 0.0112$$

$$q_0' = 381$$

$$q_1' = 12.32 .$$

The last additional viscoelastic model (labeled VE5) is derived from Galford and McElhaney's axial free vibration experiments [19]. Since there are only two quantities (storage and loss moduli) reported at one frequency value, three necessary parameters cannot be uniquely defined. Therefore, a computer program is used to simply scan a range of possible values to find the best combination to match their experimental results. From the storage and loss moduli of 9.68 psi and 3.8 psi (66.7×10^3 Pa and 26.2×10^3 Pa) respectively at 34 Hz, the following uniaxial parameters are obtained;

$$p_1 = 0.01$$

$$q_0 = 1.076\times10^4$$

$$q_1 = 7.9\times10^2.$$

Assuming again $K = 2.068\times10^9$ Pa, the deviatoric parameters are;

$$p_1' = 0.01$$

$$q_0' = 7.17\times10^3$$

$$q_1' = 5.27\times10^2.$$

Once again, those values are not necessarily unique. However, they will be used in this study as a representation from the free vibration test.

These viscoelastic models are listed in Table 4.1, but a comparison among these models can be seen graphically as done in the previous Chapter. The ratio of the loss modulus (the imaginary part of the complex modulus) and the storage modulus (the real part) is the measure of internal friction. This value, shown in the Argand diagram (the complex plane), is

the tangent of the complex modulus "vector" and sometimes referred to as the loss tangent. This value is shown to be

$$\tan\delta = \frac{q_1'\omega - p_1'q_0'\omega}{q_0' + p_1'q_1'\omega^2}$$

where δ is the phase angle The magnitudes of the complex moduli $|\Gamma(i\omega)|$ and $\tan\delta$ plotted against frequency are shown in Figures 4.2 and 4.3, respectively.

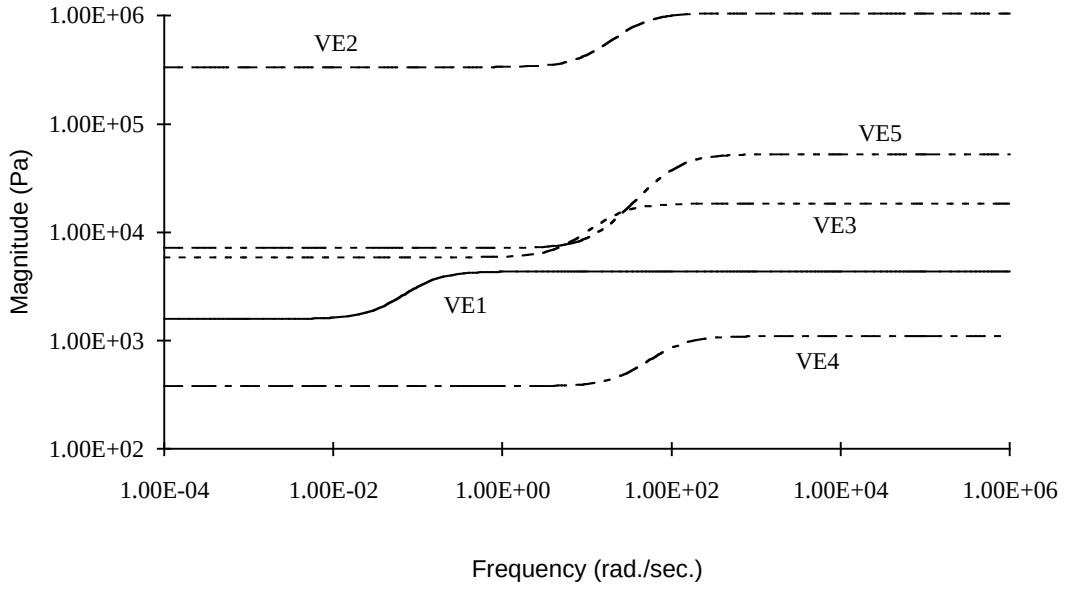

Figure 4.2 Magnitudes of Complex Moduli against Frequency

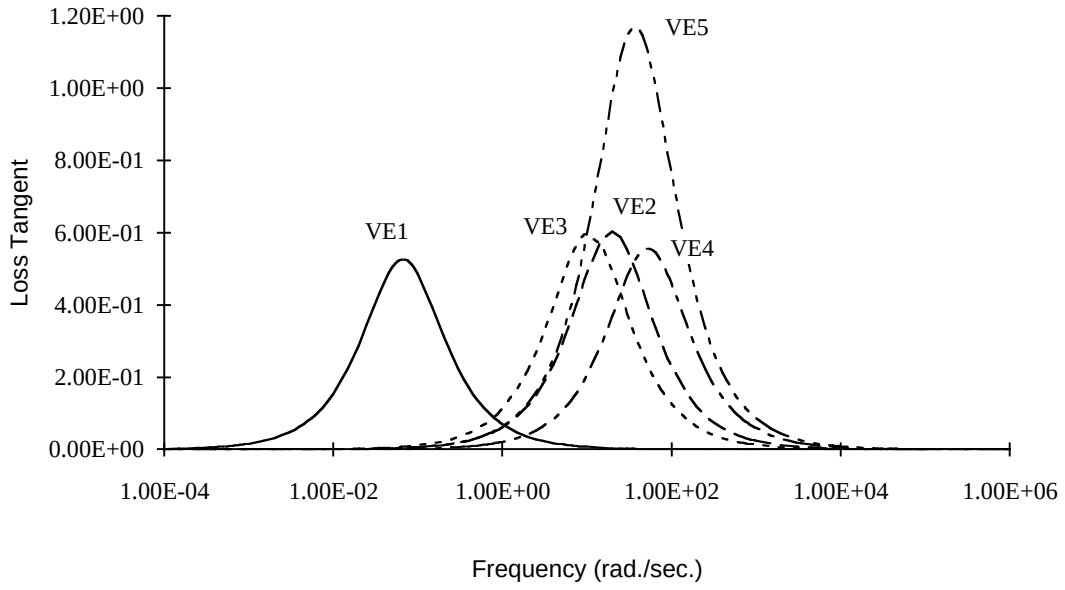

Figure 4.3 Loss Tangents of Complex Moduli against Frequency

It is noted that the scale is log-log for Figure 4.2 and semi-log for Figure 4.3. What appear close may be a factor of one or two apart.

As discovered in the previous Chapter, if a linear elastic model is substituted for a three-parameter viscoelastic model in high strain rate situations, it is best advised to use a shear modulus that is equal to the deviatoric short-term modulus. In this study, five linear elastic models with shear moduli thus derived from their corresponding viscoelastic models (labeled as elastic alternatives, EA1 through 5) are also analyzed. These elastic models, along with their viscoelastic counterparts in the engineering notation are summarized in Table 4.1.

Table 4.1 Brain Material Models for Examined Cases

Case	*Bulk Modulus (Pa)*	*Relaxation Modulus (Pa)*
VE1	2.07×10^{9}	$7.97\times10^{2}+\left(2.18\times10^{3}-7.97\times10^{2}\right)e^{-0.110t}$
VE2	1.28×10^{8}	$1.68\times10^{5}+\left(5.28\times10^{5}-1.68\times10^{5}\right)e^{-35t}$
VE3	2.07×10^{9}	$2.95\times10^{3}+\left(9.19\times10^{3}-2.95\times10^{3}\right)e^{-18.7t}$
VE4	2.07×10^{9}	$190.5+(551.3-190.5)e^{-89.5t}$ *
VE5	2.07×10^{9}	$3.59\times10^{3}+\left(2.63\times10^{4}-3.59\times10^{3}\right)e^{-100t}$
		Shear Modulus (Pa)
EA1	2.07×10^{9}	2.18×10^{3}
EA2	1.28×10^{8}	5.28×10^{5}
EA3	2.07×10^{9}	9.19×10^{3}
EA4	2.07×10^{9}	551.3
EA5	2.07×10^{9}	2.63×10^{4}

* Reported as a non-linear model

In this phase of the study it is decided to make use of another linear elastic material type in DYNA3D (Material Type 12) where material properties are directly entered as shear and bulk moduli. The same stress wave propagation test in Chapter 2 is performed using the same property values, $E = 66.7\times10^{3}$ Pa and $\nu = 0.48$, which are converted to $G = 22.534\times10^{3}$ Pa and $K = 555.83\times10^{3}$ Pa. The results, in the form of stress and particle velocity in the wave propagation direction, are identical to those observed in Chapter 2, thus confirming suitability of this material representation.

The impactor is simply assumed to be a rigid body, and the material properties for carbon steel taken from [74] are used for contact calculations. The density of the impactor is artificially modified to increase its mass to 2.6 kg, roughly half of the weight used in Nahum *et al.*'s cadaver impact experiments [57]. This weight is chosen since the current model lacks the skin layer and padding materials supposedly used in Nahum *et al.*'s experiments.

The amount of discrete masses added to compensate for the lack of the facial features and neck is determined to match the numbers reported in Walker *et al.* [57]. A set of discrete masses is added to the front half of the bottom of the model to match the weight of the head without the neck, which is 4.38 kg. Another set of discrete masses is added to the back half of the same region to simulate the neck. The total weight is 6.00 kg.

4.2.3 Scenarios

The model is used to simulate frontal impact. The impact location on the head is arbitrarily determined; no attempt is made to align the head and impactor using some anatomical reference planes such as the Frankfort plane. The models are tested at two different impactor velocities; one at 15 miles per hour (mph) (one half of the standard crash test speed used by National Highway Traffic Safety Administration) and the other at 7.5 mph.

4.3 Results and Discussions

The results are extracted from the model in the form of maximum shear strain, pressure, and resultant acceleration. Pressure is measured at the coup, contracoup sites. Maximum shear strain is measured at the same locations as pressure, and at two additional locations; one is at the bottom of the frontal lobe, and the other, an arbitrarily selected point furtherers from any skull interior surface. The resultant acceleration is measured at the CG of the head and points on the both sides of the skull, which are projected laterally from the CG of the head.

The additional points of interest for maximum shear strain are selected; one is the bottom of the frontal lobe and the other an arbitrarily selected interior point, since the former happens to be where the maximum shear strain is likely to occur in this model. Once again, it must be noted that this model does not contain some important anatomical structures such as the tentorium or falx. Therefore, it does not meant to predict specific locations of injuries. The latter location is selected since this is away from the surface of the brain which is adhered to the skull. This location avoids the boundary effect between the brain and the skull.

From the acceleration histories measured at those locations, HIC is calculated using a FORTRAN subroutine provided by the National Highway Traffic Safety Administration (NHTSA). This subroutine uses an algorithm that efficiently finds a time interval, or time window, that gives the maximum value of HIC. A driver and other supporting routines are written to read an output file generated by GRIZ, a post-processor for DYNA3D. These routines assume the acceleration histories are in m/sec^2, and covert them in terms of acceleration of gravity (G).

One approximation that must be taken into account is that the provided subroutine assumes a

uniform time step size. An acceleration history is read as a series of discrete acceleration values at this interval. Output files from GRIZ, however, are written at intervals that generally change from time step to time step, since DYNA3D determines time step size based on the minimum effective element size which can change due to deformation and distortion. Therefore, an average time step size is determined for the entire history, and this value is used as the time step size used in the subroutine. At this point, it is assumed that excessive deformation does not cause drastic changes in time step sizes. A standard deviation is calculated for time step sizes to check this assumption.

A fictitious acceleration history, shown in Figure 4.4, is used to test the validity of the code. Using the formula for the HIC,

$$\mathrm{HIC} = \max_{t_1,t_2}\left\{(t_2 - t_1)\left[\frac{1}{(t_2 - t_1)}\int_{t_1}^{t_2} a(t)dt\right]^{2.5}\right\}$$

the provided acceleration history should give the HIC value of 819.9 with a proper time window of 20 milliseconds or more. The FORTRAN code gives 817.2, which is within less than 0.35% of the theoretical value. This accuracy is deemed acceptable.

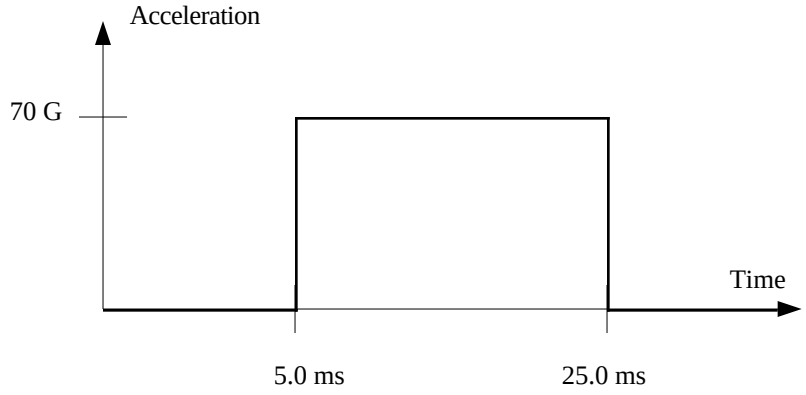

Figure 4.4 Test Acceleration History

Before the results from the material models listed in Table 4.1 are examined, a fictitious "average" viscoelastic model is created to perform a parametric study. Even though doing so is not the main purpose of this study, a parametric study helps confirm speculations observed

from the existing brain constitutive models. Parametric studies are performed only at 15 mph.

This "average" model is created by simply taking the arithmetic averages of the short term moduli, long term moduli and time constants from VE1, VE3, VE4 and VE5. VE2 is dropped since it does not have a clear experimental foundation. It must be noted such averaging itself from different experiments is purely academic and has no basis for representing the brain material. The model thus created (referred to as VEA) is represented by:

$$G(t) = 1.88 \times 10^3 + \left(9.56 \times 10^3 - 1.88 \times 10^3\right) e^{-52.08t}$$

First, the comparisons are made between the results from the linear viscoelastic models and their linear elastic counterparts. As pointed out in the previous Chapter, this substitution only works only if the material characteristics and dynamic conditions are such that strain rate is high enough so that a linear viscoelastic model's behavior can be simulated by a linear elastic model whose Young's modulus is the same as the short term modulus.

As expected, most viscoelastic-elastic pairs produce identical results at both speeds, in terms of pressure and maximum shear strain. Representative plots from VE1 and EA1 at both speeds are shown in Figures 4.5 through 4.12.

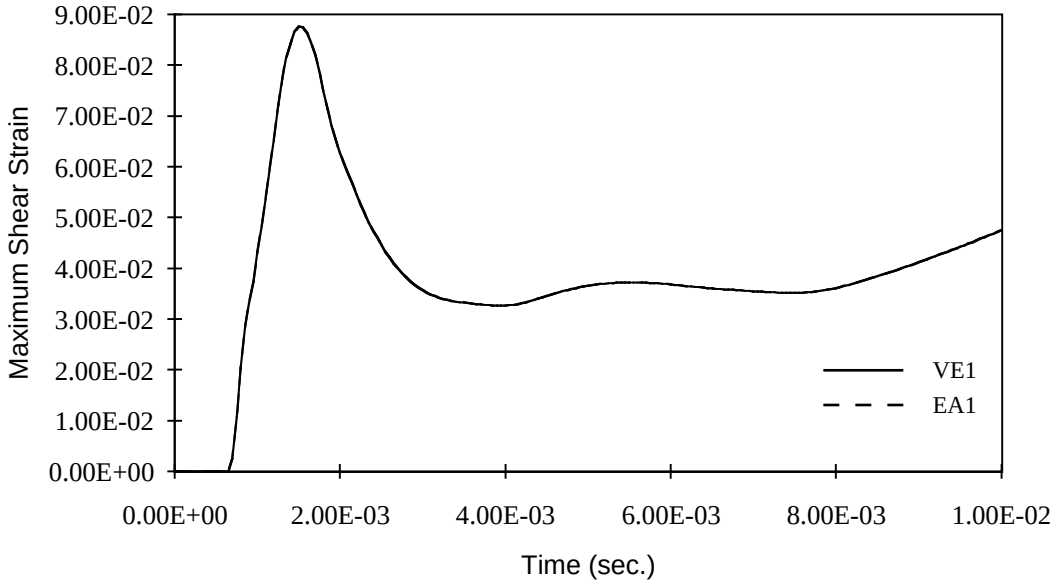

Figure 4.5 Maximum Shear Strain History at Coup Site, Models VE1 and EA1 at 15 mph

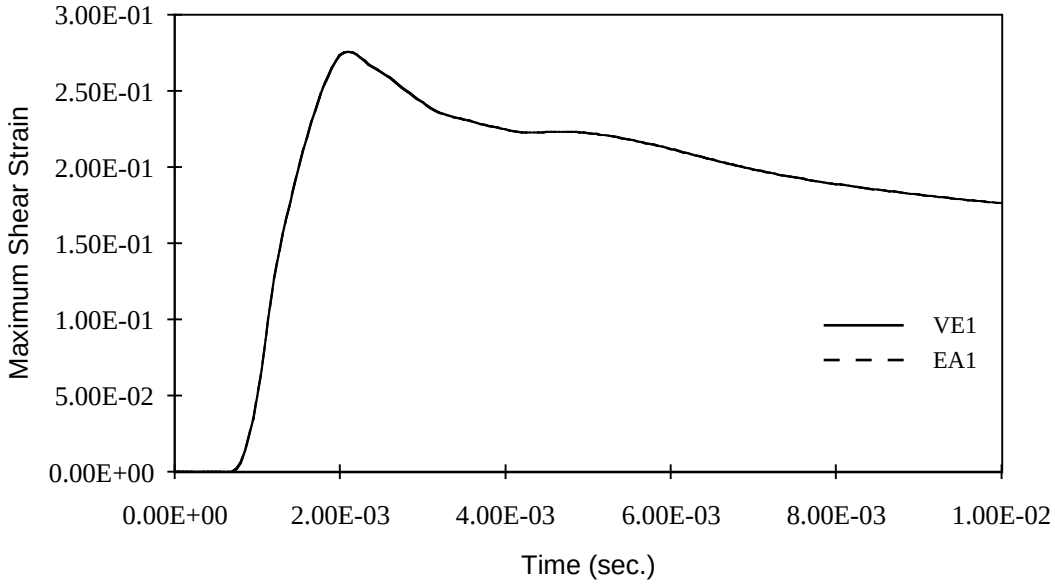

Figure 4.6 Maximum Shear Strain History at Bottom of Frontal Lobe, Models VE1 and EA1 at 15 mph

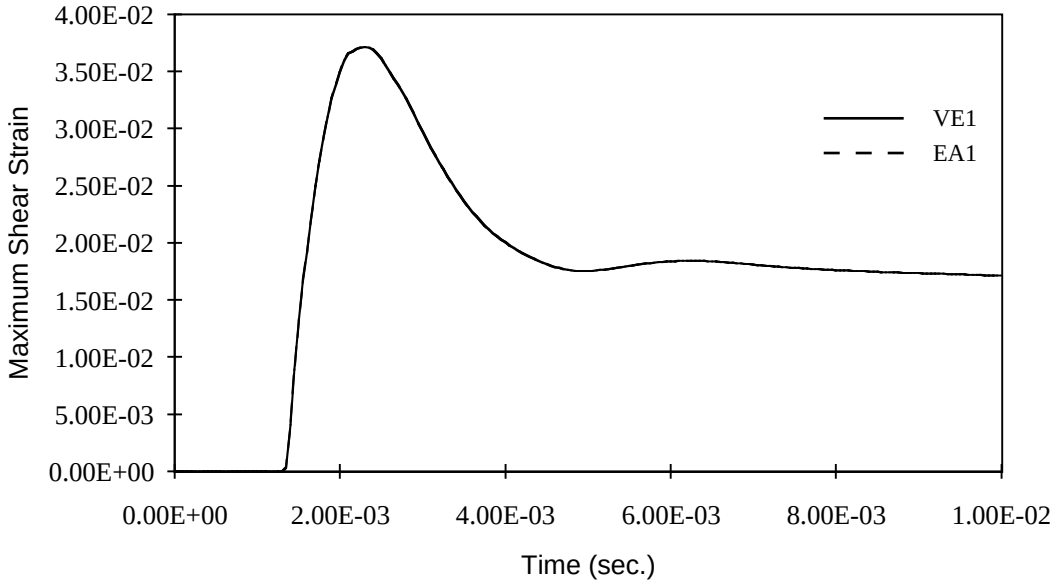

Figure 4.7 Maximum Shear Strain History at Coup Site, Models VE1 and EA1 at 7.5 mph

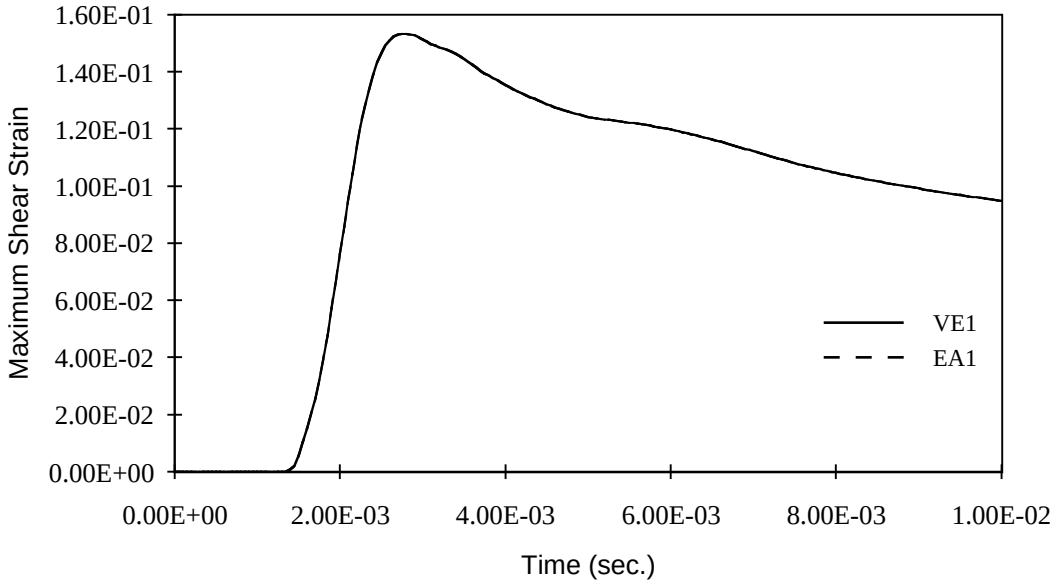

Figure 4.8 Maximum Shear Strain History at Bottom of Frontal Lobe, Models VE1 and EA1 at 7.5 mph

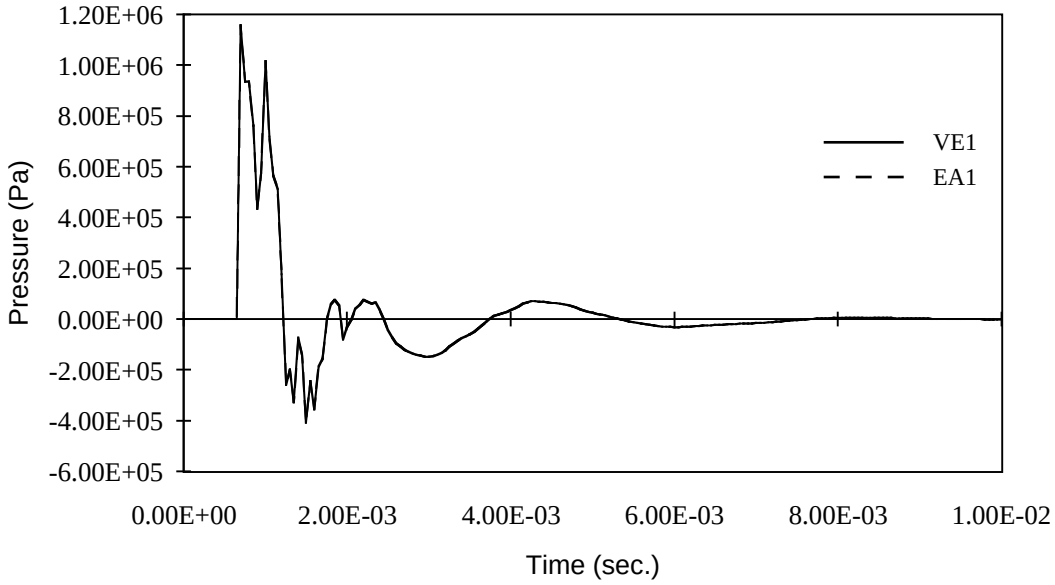

Figure 4.9 Pressure History at Coup Site, Models VE1 and EA1 at 15 mph

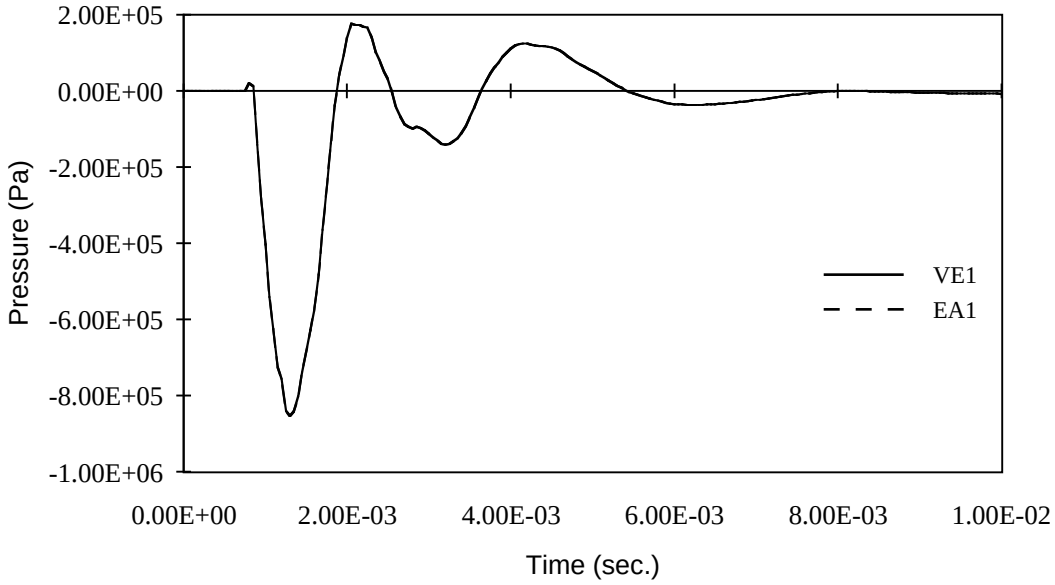

Figure 4.10 Pressure History at Contracoup Site, Models VE1 and EA1 at 15 mph

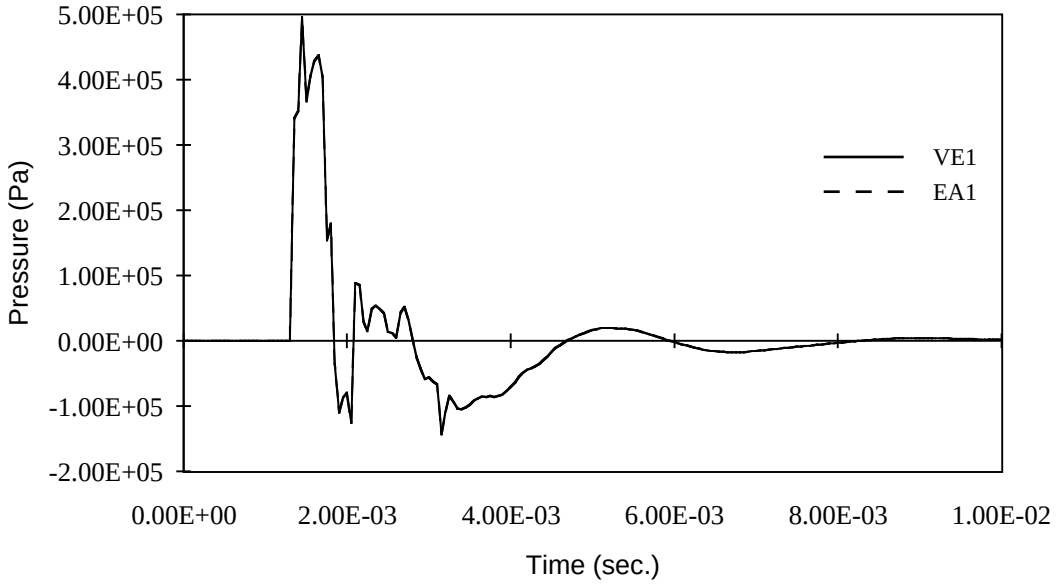

Figure 4.11 Pressure History at Coup Site, Models VE1 and EA1 at 7.5 mph

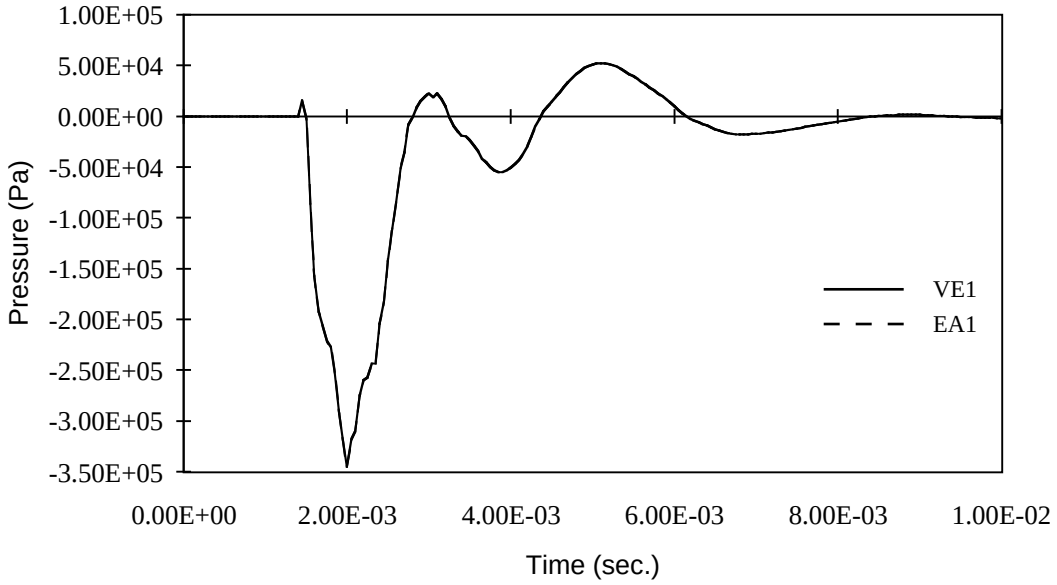

Figure 4.12 Pressure History at Contracoup Site, Models VE1 and EA1 at 7.5 mph

However, VE5 and EA5, while their pressure responses are identical, produce noticeably different results in terms of maximum shear strain, as shown in Figures 4.13 though 4.18.

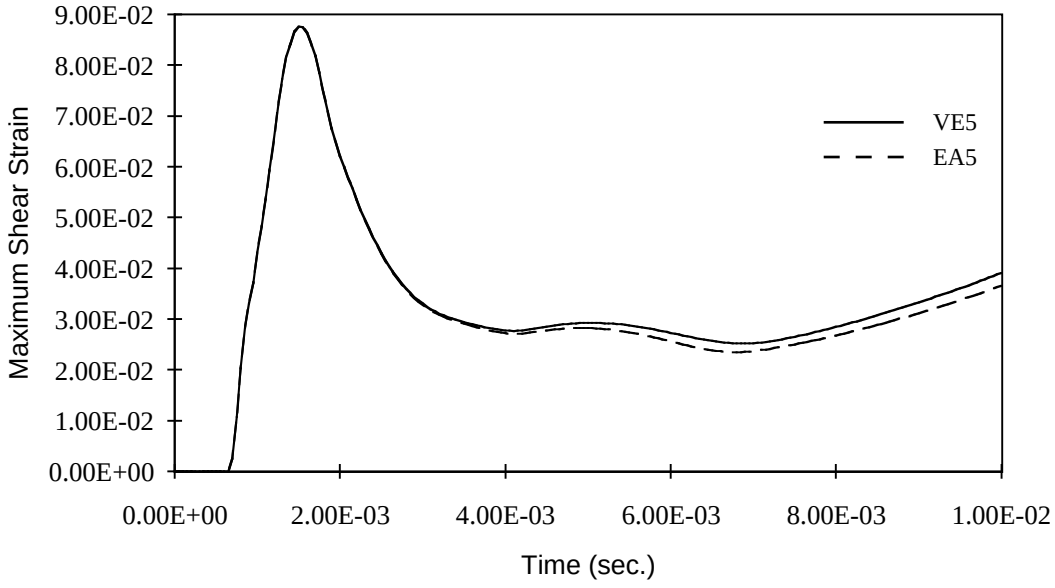

Figure 4.13 Maximum Shear Strain History at Coup Site, Models VE5 and EA5 at 15 mph

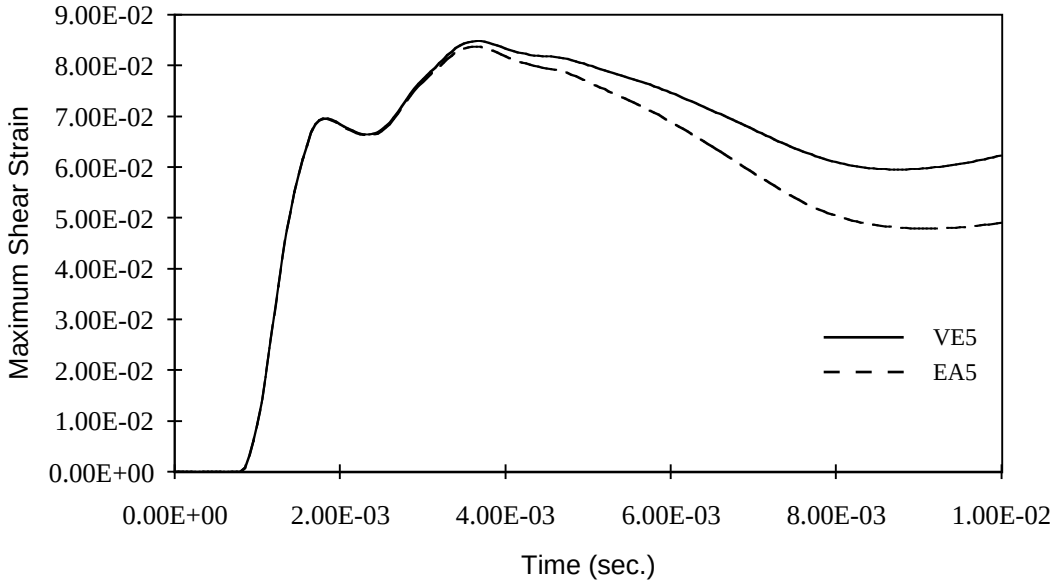

Figure 4.14 Maximum Shear Strain History at Contracoup Site, Models VE5 and EA5 at 15 mph

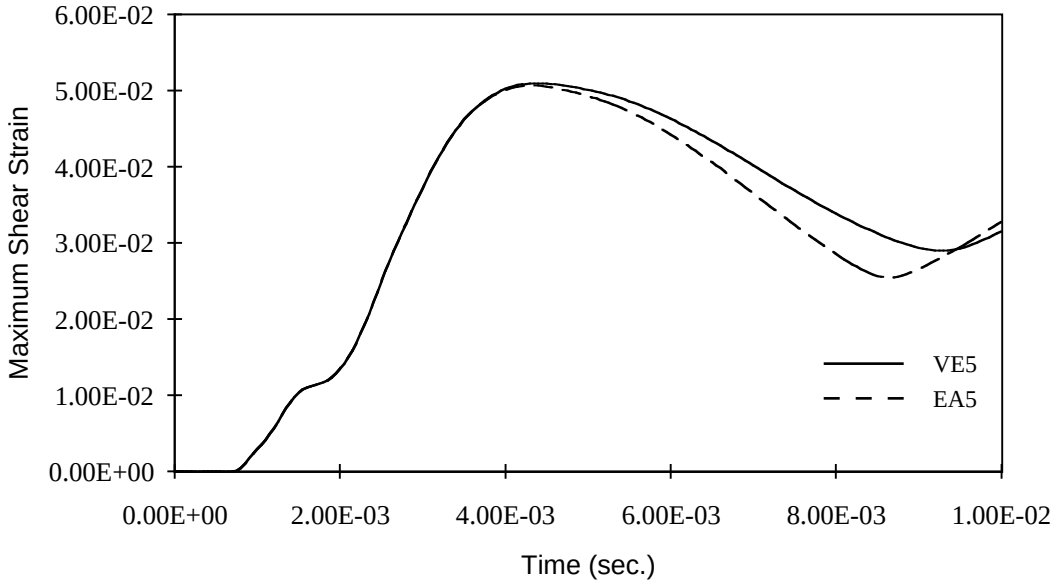

Figure 4.15 Maximum Shear Strain History at Middle of Brain, Models VE5 and EA5 at 15 mph

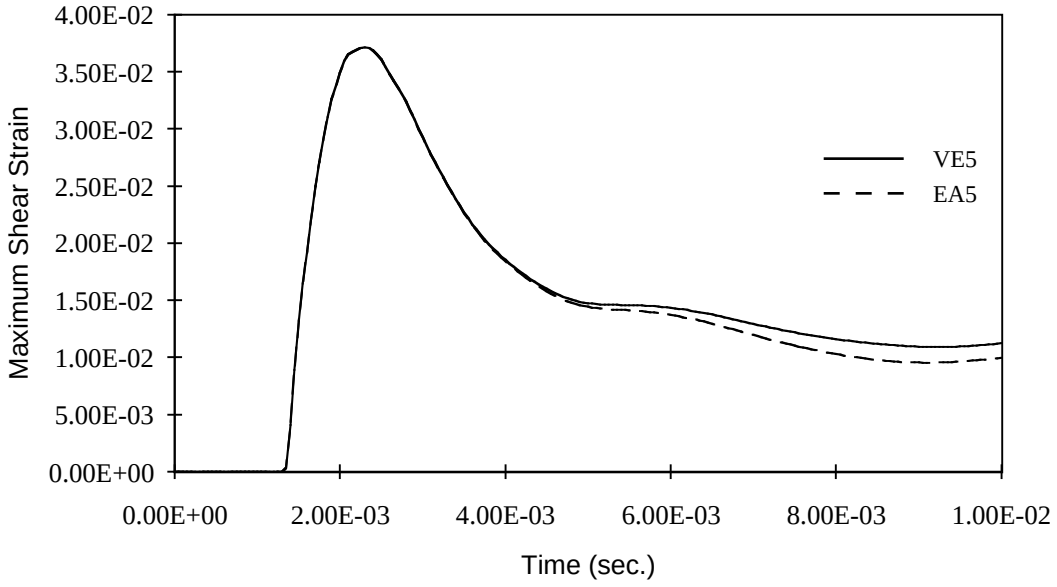

Figure 4.16 Maximum Shear Strain History at Coup Site, Models VE5 and EA5 at 7.5 mph

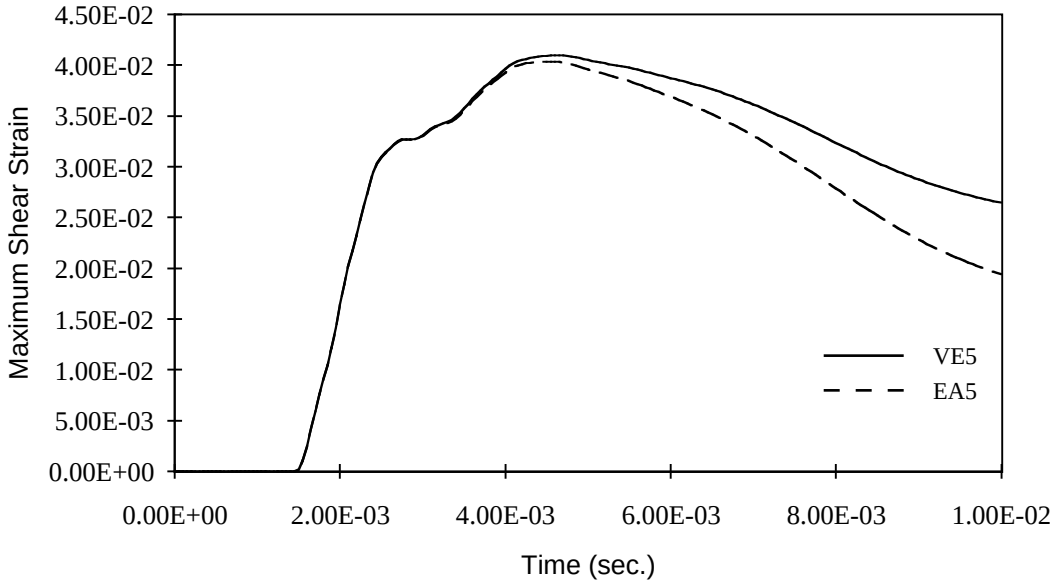

Figure 4.17 Maximum Shear Strain History at Contracoup Site, Models VE5 and EA5 at 7.5 mph

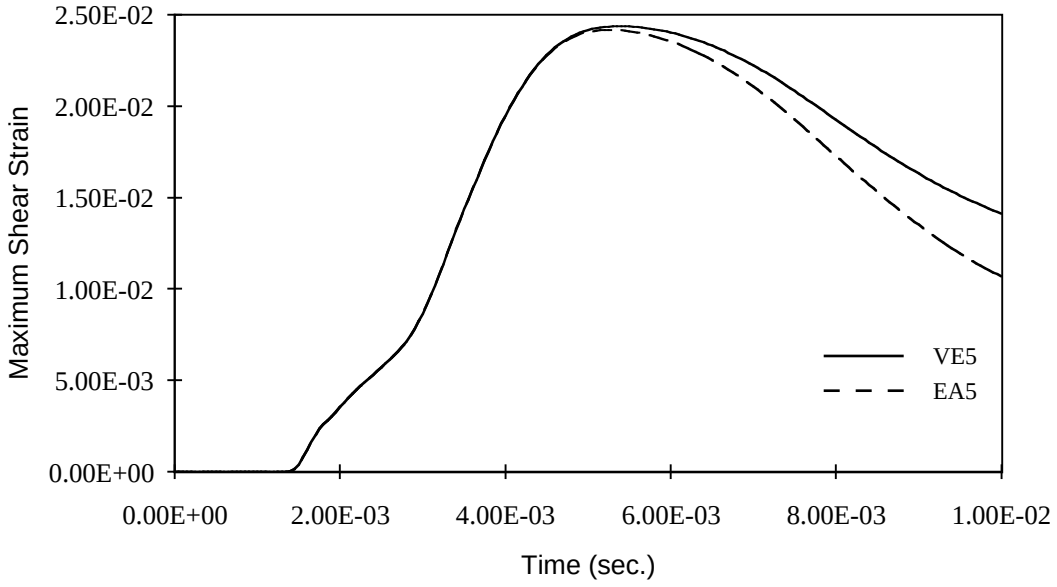

Figure 4.18 Maximum Shear Strain History at Middle of Brain Site, Models VE5 and EA5 at 7.5 mph

For this pair at 15 mph, after reaching the same maximum value around 3.6 milliseconds (msec.), the unloading for VE5 is more slowly than that for E5. It is suspected that in this unloading phase, VE5's high decay constant value (100) causes the discrepancy. In order to confirm this, a parametric study using VEA is shown in Figures 4.19 through 4.21. In this

series of runs, the decay constant is increased by 10 and 100 to demonstrate that increasing the decay constant slows down the unloading after the peak.

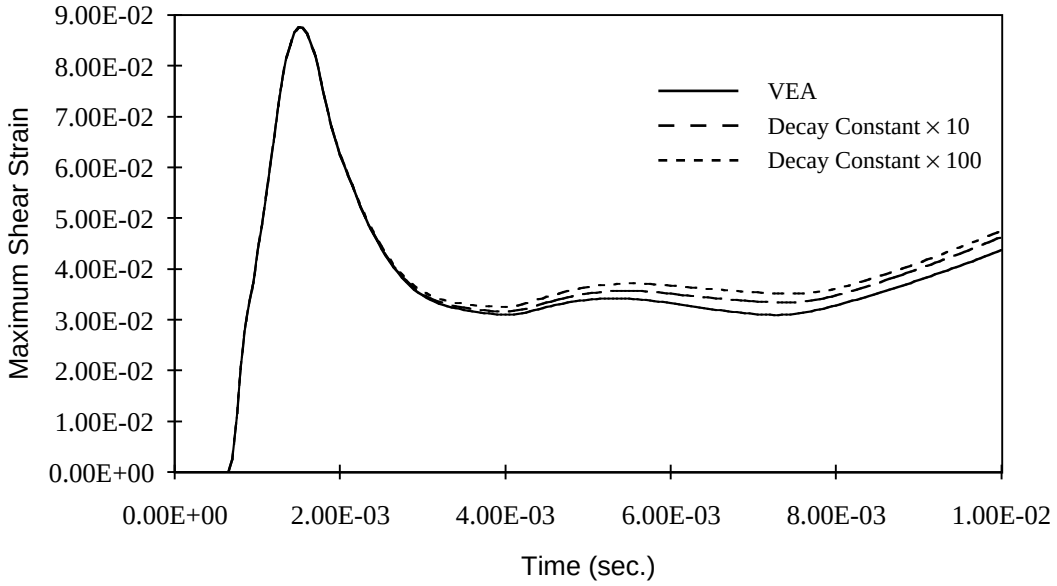

Figure 4.19 Maximum Shear Strain History at Coup Site, Model VEA with Varying Decay Constant

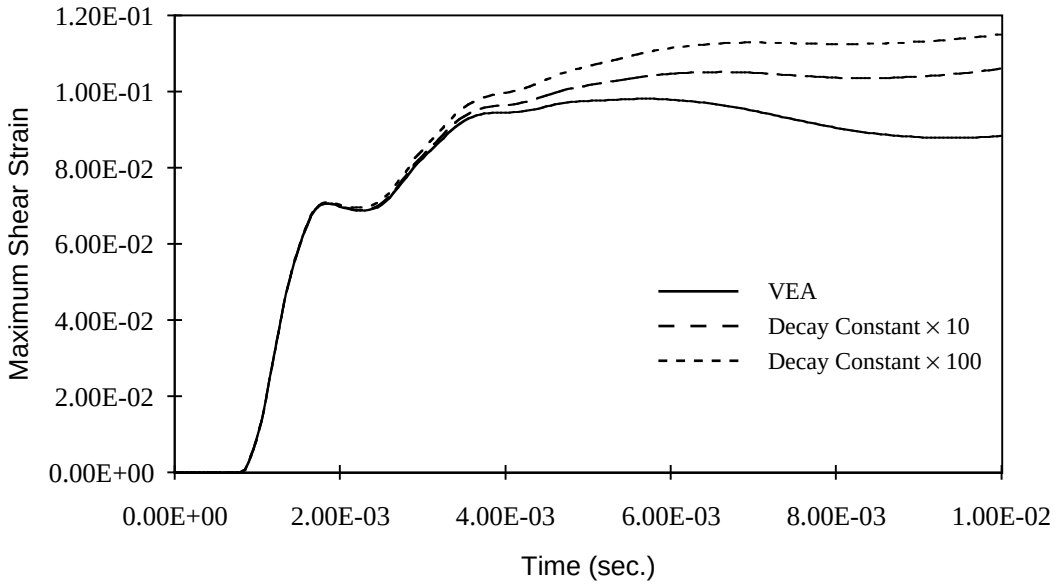

Figure 4.20 Maximum Shear Strain History at Contracoup Site, Model VEA with Varying Decay Constant

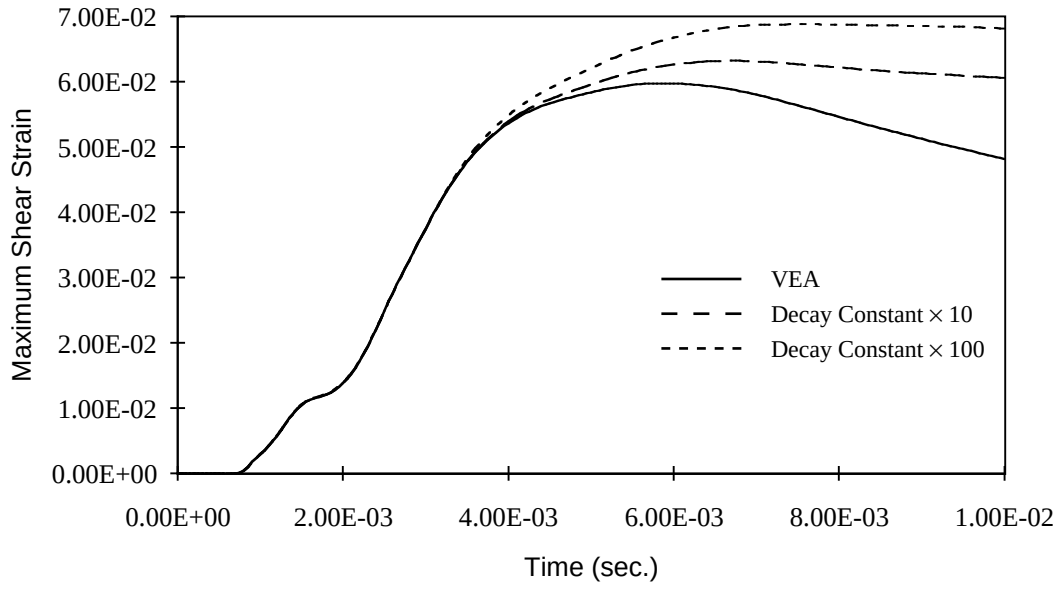

Figure 4.21 Maximum Shear Strain History at Middle of Brain, Model VEA with Varying Decay Constant

A high decay constant means there is more viscous effect in a shorter time scale. In this scenario, this viscous effect separates a viscoelastic model from a linear elastic model. As it can be seen from the Figures above, the more viscous effect is present (*i.e.* the higher the decay constant), the less pronounced the unloading phase is; which is what is observed in the VE5/EA5 case. Therefore, from this point on the focus is concentrated on viscoelastic models, and linear elastic models are, for the most part, dismissed.

As discovered in the previous phase, the bulk modulus controls pressure response. Therefore, VE1, VE3, VE4 and VE5, that share the same bulk modulus, yield an identical coup and contracoup pressure history. On the other hand, VE2, whose bulk modulus is less than those from the other models, produces a different pressure response (see Figures 4.22 and 4.23) than those from other model (response from VE1 is superimposed to show the difference). In general, the softer the bulk modulus is, the less the peak pressure value at either location. This trend is verified in a parametric study using VEA where its bulk modulus is changed (Figures 4.24 and 4.25)

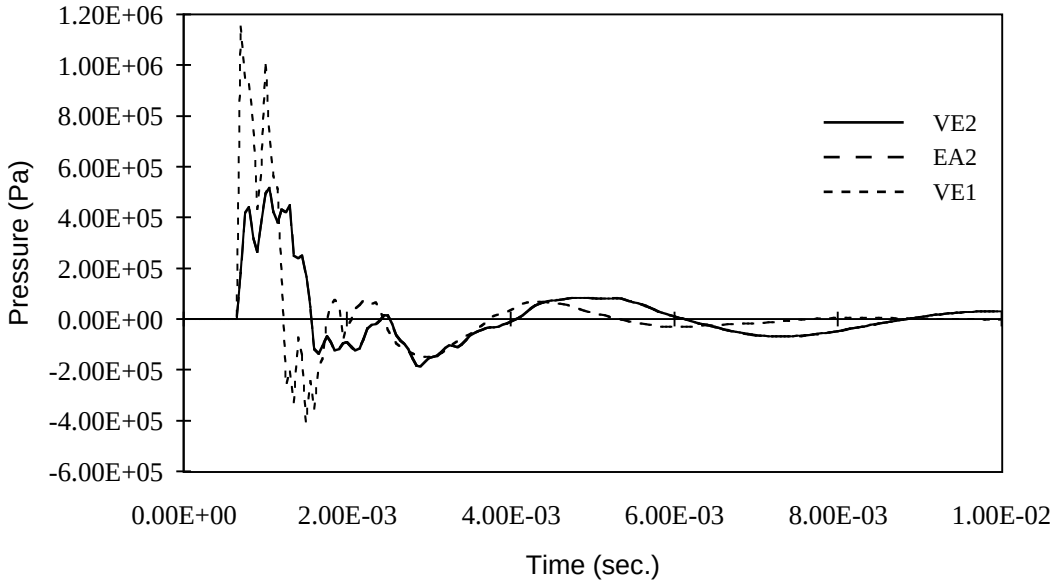

Figure 4.22 Pressure History at Coup Site, Models VE2 and EA2 Compared with VE1, at 15 mph

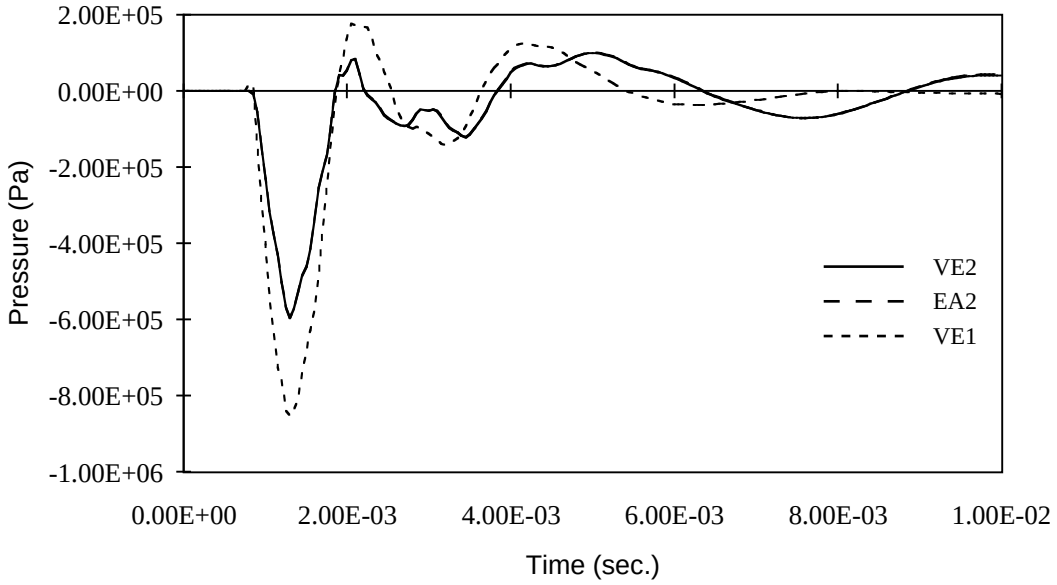

Figure 4.23 Pressure History at Contracoup Site, Models VE2 and EA2 Compared with VE1, at 15 mph

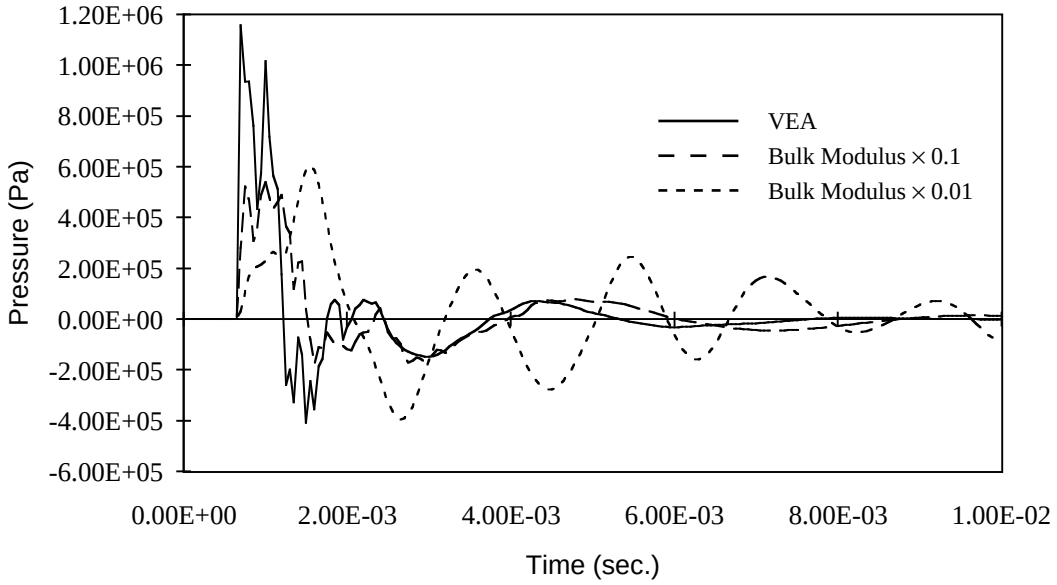

Figure 4.24 Pressure History at Coup Site, Model VEA with Varying Bulk Modulus

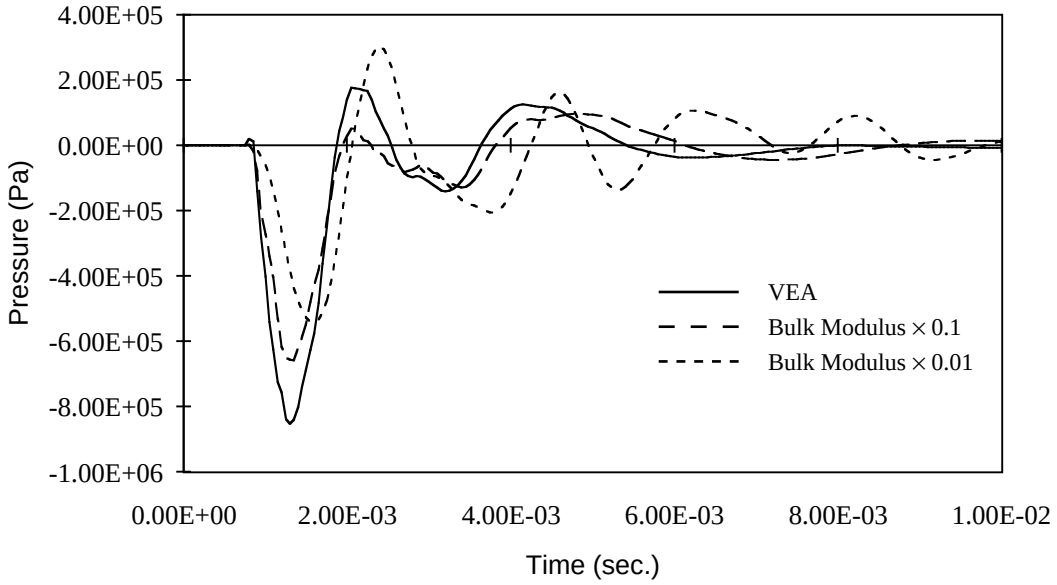

Figure 4.25 Pressure History at Contracoup Site, Model VEA with Varying Bulk Modulus

The most intriguing finding from all the models analyzed in study is shown in Table 4.2.

Table 4.2 HIC from Examined Cases, at Head CG

15 mph	*HIC from VE*	*HIC from EA*	*7.5 mph*	*HIC from VE*	*HIC from EA*
1	3894.8	3894.8		248.8	248.8
2	8733.8	8769.2		481.5	483.6
3	3885.8	3885.9		248.0	248.0
4	3896.9	3896.7		249.0	249.0
5	3864.6	3864.2		246.0	246.0

As seen in this table, HIC values calculated at head CG from all models, except for the VE2/EA2 pair, are nearly identical. Excluding VE2, all HICs are within less than 1% of one another for the 15 mph cases, and roughly 1.2% for 7.5 mph cases. Excluding VE2, it appears that HIC is inversely proportional to the apparent stiffness of the viscoelastic model. The softest viscoelastic model, VE4, gives the highest HIC while the firmest (VE5), the lowest HIC. This seems to be true from a parametric study at 15 mph where both short term and long term moduli are varied together, another where the short term modulus is varied independently, and another where the decay constant is varied (Table 4.3).

Table 4.3 HIC Under Varying Parameters of Viscoelastic Model

Parametres changed	*HIC*
VEA	3885.4
Decay constant x 10	3885.8
Decay constant x 100	3889.4
Short term modulus x 10	3782.0
Short term modulus x 100	3860.0
Short term/long term moduli x 10	3781.8
Short term/long term moduli x 100	3865.3

It is clear that the decay constant has little effect on HIC. Multiplying either short term modulus only or both short term and long term moduli together by 10, it is observed that HIC decreases, albeit slightly (2.7%). However, when the moduli are multiplied by 100, HIC shows an increase from the preceding case, even though the magnitude is still less than the original. Therefore, it appears that the relation between HIC and short term modulus or combination of short term and long term moduli is nonlinear. Nonetheless, the overall variation in HIC is so minute (the discrepancy between the highest HIC measured from VE4 and the lowest from the parametric study is 3%) that the effect of the change in deviatoric

material constitutive models on HIC is considered insignificant.

The only unique feature about VE2 is its bulk modulus which is lower than the rest. The disparity exhibited by VE2 can be explained, once again, by decreasing the bulk modulus in VEA to show the effect on HIC as the bulk modulus is reduced by 10 and 100 at 15 mph. The results of this parametric study is shown in Table 4.4.

Table 4.4 HIC Under Varying Bulk Modulus, at Head CG

Parameters changed	*HIC*
VEA	3885.4
Bulk Modulus x 0.1	6495.9
Bulk Modulus x 0.01	72938.4

The HIC value increases by 67% with one tenth of the original bulk modulus, and when the bulk modulus by reduced by 100, HIC increases 19 times. Therefore, two major conclusions are drawn from this part of the exercise. One is that HIC is highly sensitive to the bulk modulus of the brain, and the other is that it is nearly insusceptible to the change in the brain's deviatoric constitutive characteristics.

It must be mentioned that the brain is normally considered just as incompressible as water [33, 46, 50], and reducing the bulk modulus was done by Ruan *et al.* [69] to match their finite element model's results to those from experiments. This is undoubtedly implemented to accommodate internal structures or functions that are not modeled, such as the ventricles or the communication of the cerebrospinal fluid between surrounding structures. In other words, alteration in the bulk modulus of the brain may be based on the degree of simplification of the finite element model, and caution must be exercised when such a change is incorporated.

The fact that they produce similar HICs does not mean that the internal dynamics are the same for all models. As shown in Figures 4.26 through 4.31, in terms of maximum shear strain, these viscoelastic models behave drastically differently from one another.

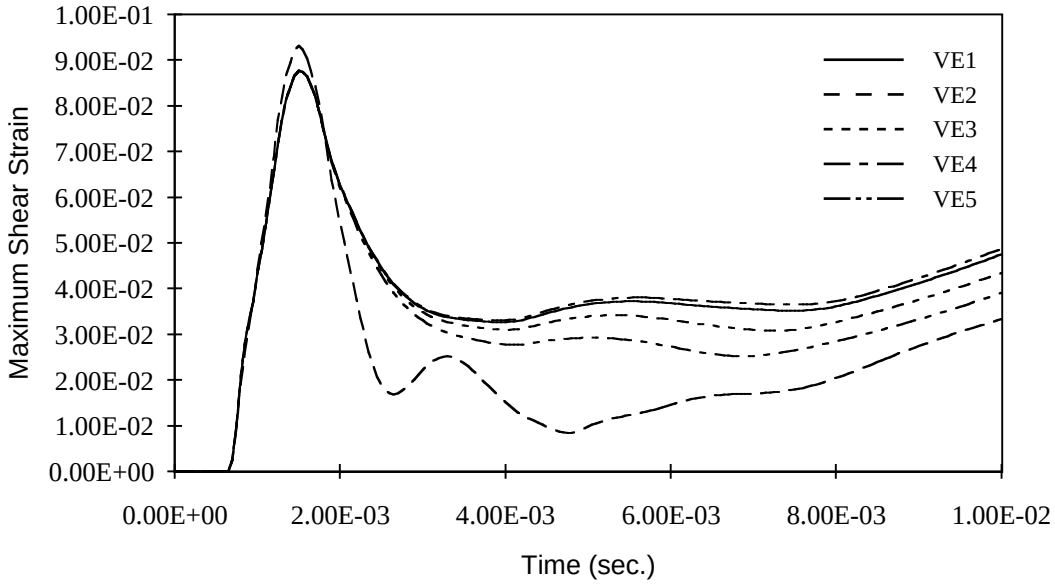

Figure 4.26 Maximum Shear Strain History at Coup Site, Viscoelastic Models at 15 mph

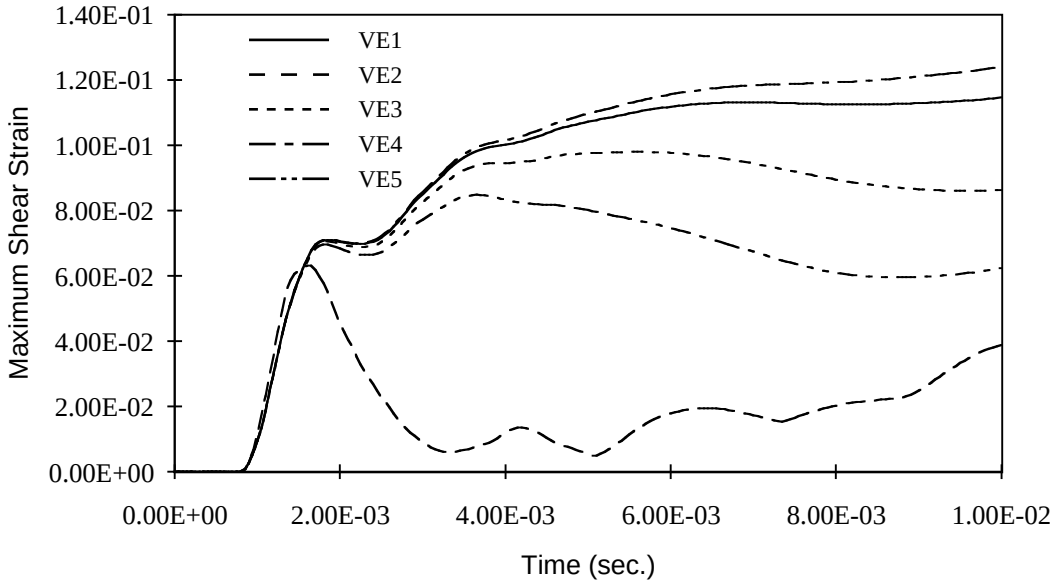

Figure 4.27 Maximum Shear Strain History at Contracoup Site, Viscoelastic Models at 15 mph

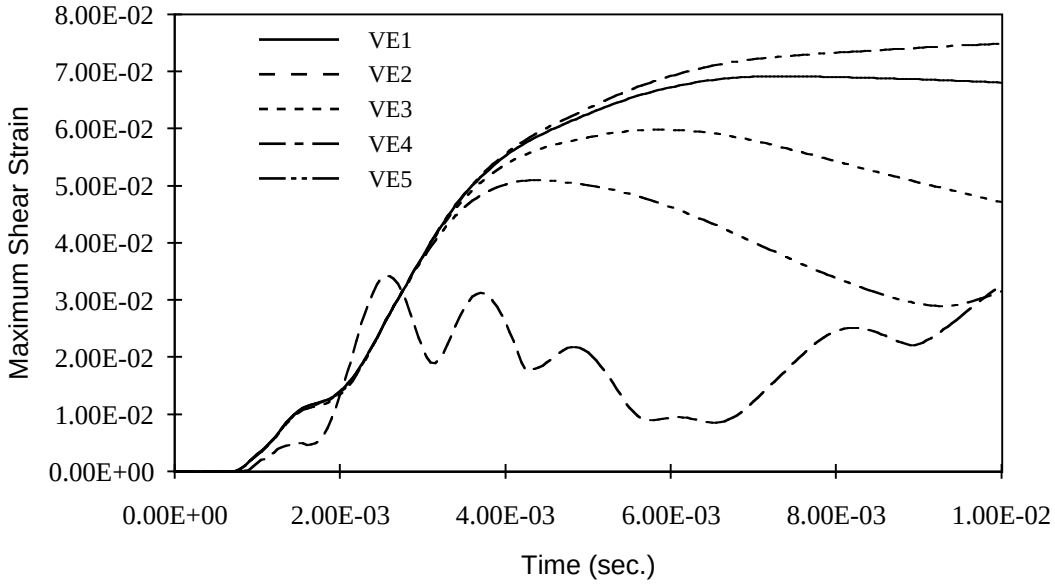

Figure 4.28 Maximum Shear Strain History at Middle of Brain, Viscoelastic Models at 15 mph

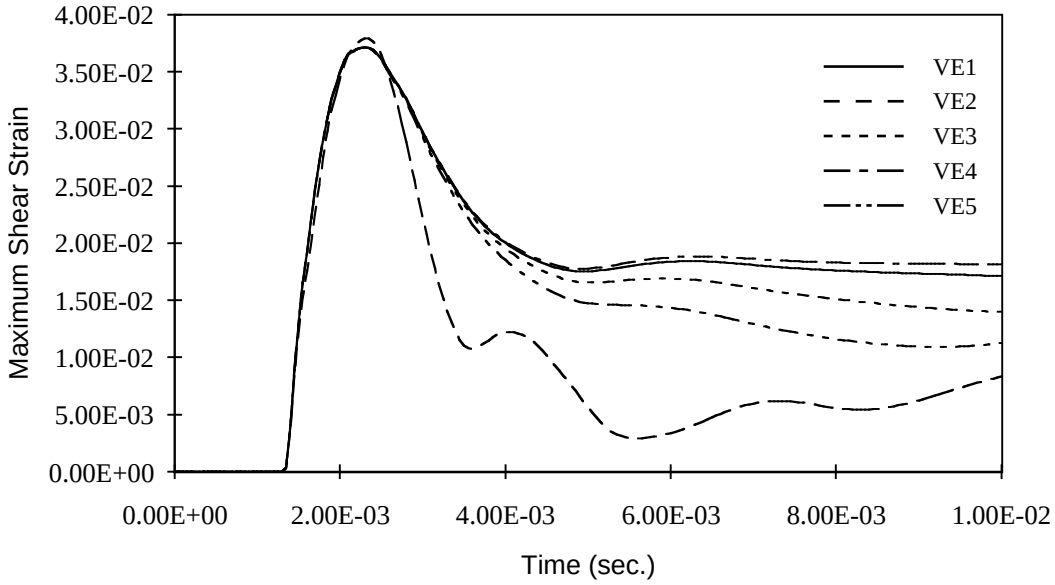

Figure 4.29 Maximum Shear Strain History at Coup Site, Viscoelastic Models at 7.5 mph

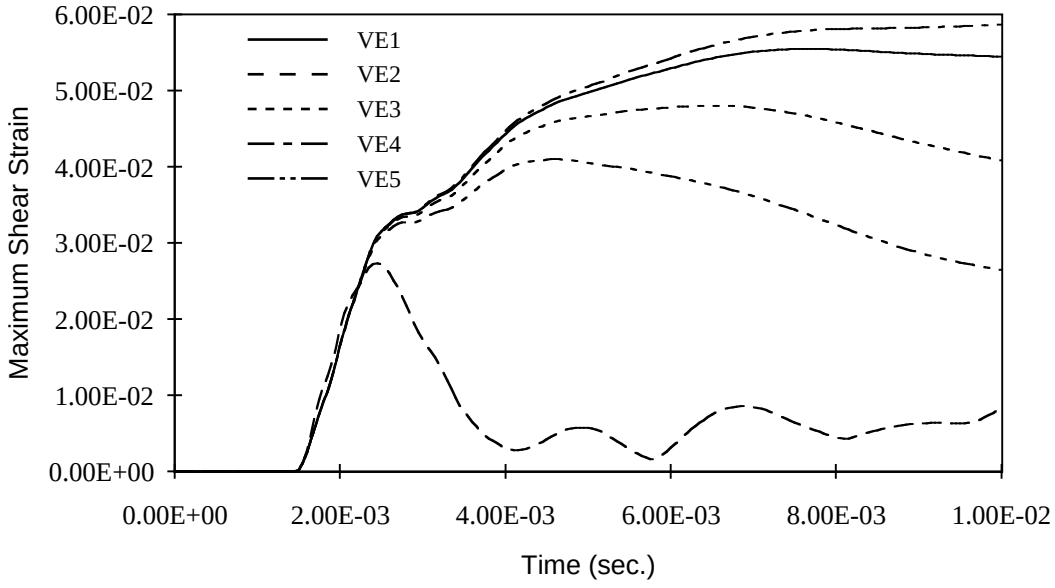

Figure 4.30 Maximum Shear Strain History at Contracoup Site, Viscoelastic Models at 7.5 mph

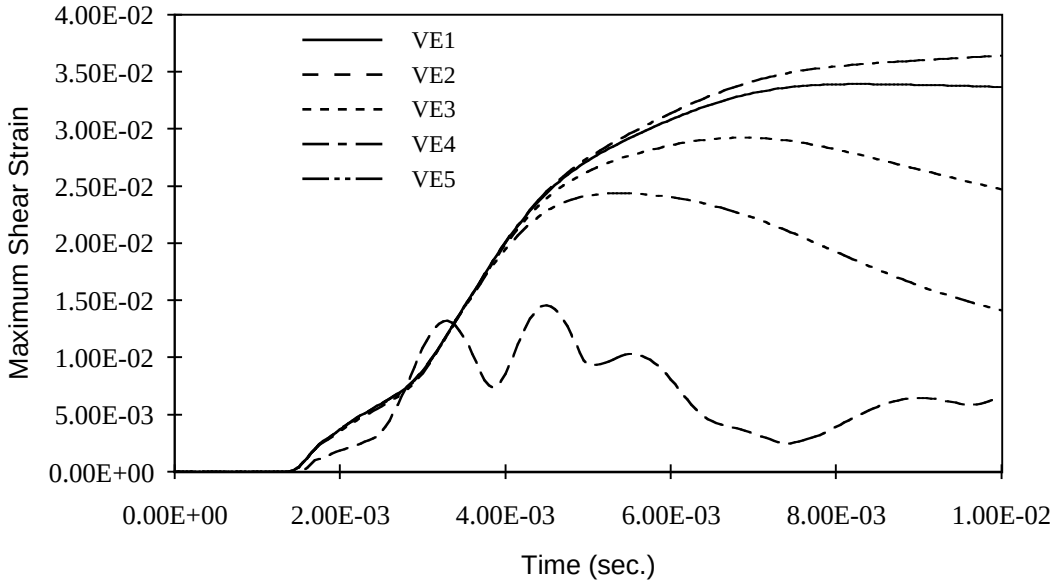

Figure 4.31 Maximum Shear Strain History at Middle of Brain, Viscoelastic Models at 7.5 mph

In Figures above, after following similar initial loading patterns, some models (VE1, VE4) continue to be loaded, while others (VE3, VE5) either roughly maintain their strain values or unload. This is significant since these models differ in general response pattern, not just in overall maximum magnitudes. This behavior can be explained by another parametric study

on the short term modulus (Figures 4.32 through 4.34), which shows that the shear strain response decreases as the short term modulus is increased.

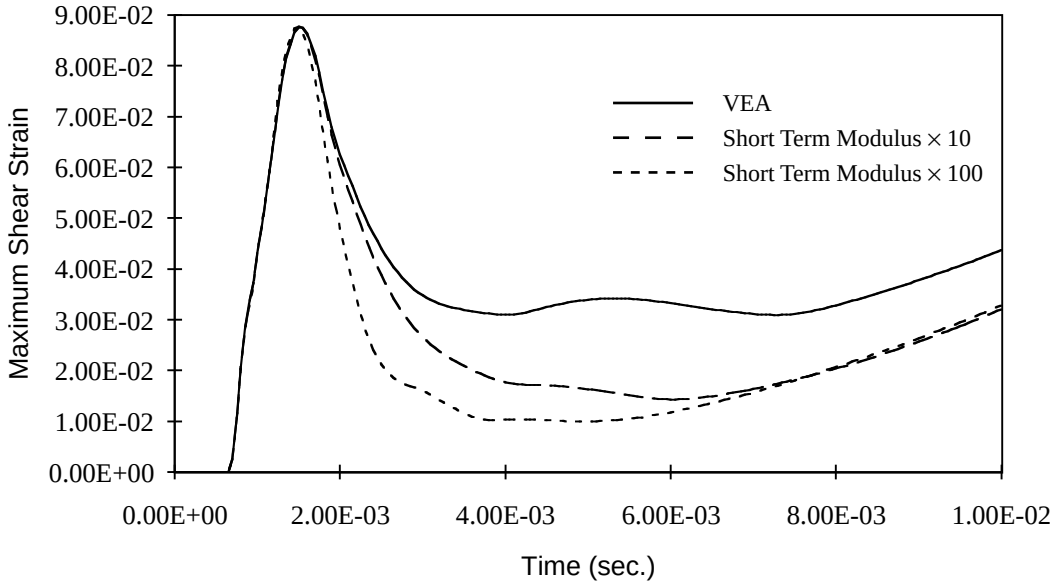

Figure 4.32 Maximum Shear Strain History at Coup Site, Model VEA with Varying Short Term Modulus

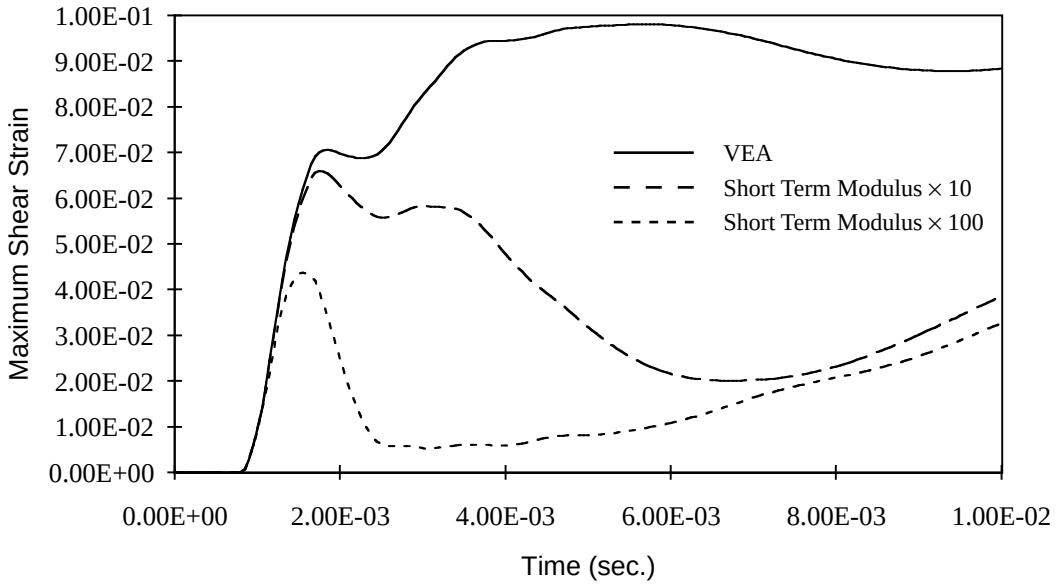

Figure 4.33 Maximum Shear Strain History at Contracoup Site, Model VEA with Varying Short Term Modulus

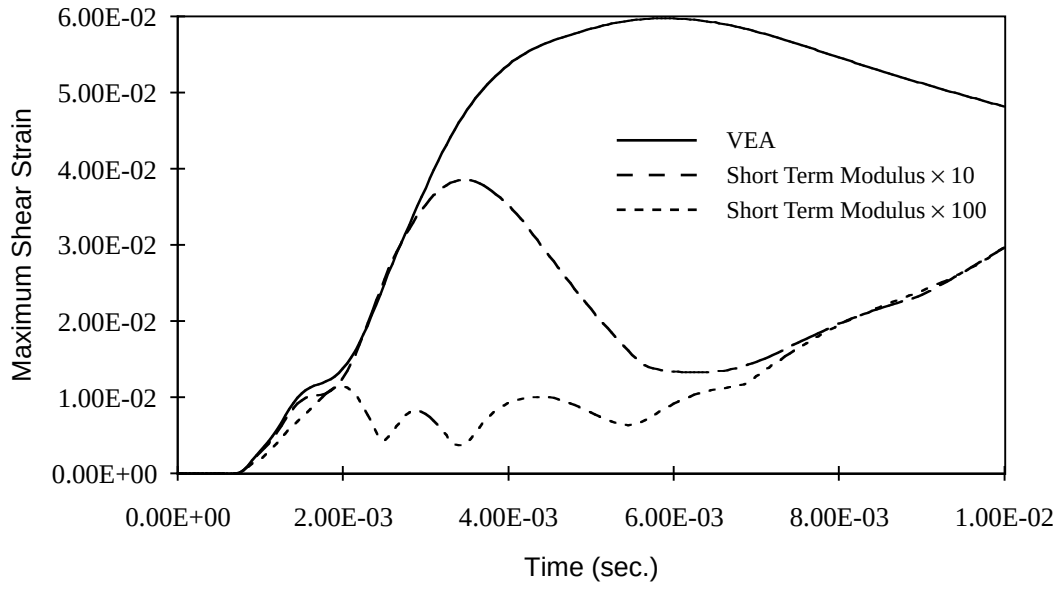

Figure 4.34 Maximum Shear Strain History at Middle of Brain, Model VEA with Varying Short Term Modulus

VE2's idiosyncratic behavior is attributed to the combination of its generally high shear modulus and low bulk modulus. As Figure 4.35 indicates, lowering the bulk modulus causes the loading pattern to shift dramatically, and in general, increases the shear strain response. It is suggested that the particular response exhibited by VE2, which shows higher shear strain around 2.5 msec., is dominated initially by the low bulk modulus (as it produces higher response), then by the higher short term modulus (which suppresses shear responses).

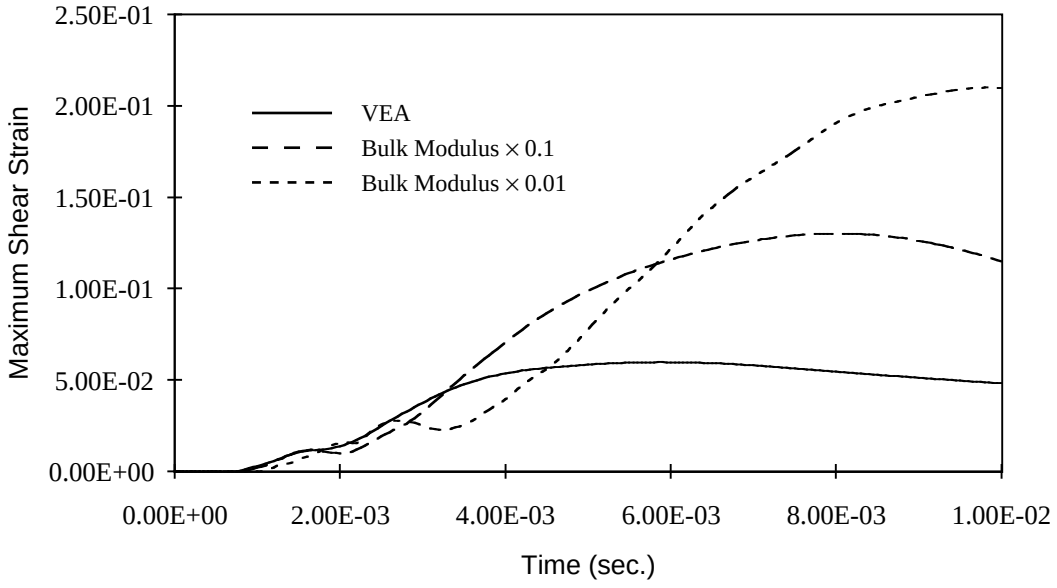

Figure 4.35 Maximum Shear Strain History at Contracoup Site, Model VEA with Varying Bulk Modulus

More dramatic effect is shown in Table 4.5, which shows the percentage of elements within the brain that supposedly "failed" during the dynamic event. Since there is no established general failure criterion for the brain tissue, a threshold shear strain value is arbitrarily assigned as 0.101. This value is taken from Margulies and Thibault [47] who determined this value in a dimensionless analytical model for diffuse axonal injury (DAI). Each element in the brain is checked at each time step for its maximum shear strain. At any time the maximum shear strain exceeds this threshold value, the element is marked as, "failed."

Table 4.5 Failure Percentages for Examined Cases

15 mph	*VE (%)*	*EA (%)*	*7.5 mph*	*VE (%)*	*EA (%)*
1	21.8	21.8		0.68	0.68
2	0.78	0.78		0.03	0.03
3	14.4	14.4		0.24	0.24
4	26.6	26.2		1.39	1.25
5	9.23	8.96		0.20	0.20

As seen in this table, the failure rates range from less than 1% (VE2) to around 27% (VE4) at 15 mph. The rates are, logically, inversely proportional to the apparent stuffiness of the models, with stiffer materials producing less failure, and softer materials producing more.

This is significant since if only the absolute maximum shear strain values are examined (Table 4.6), it can be seen that the differences among the models are not dramatic. Those maximum values are observed at the bottom of the frontal lobe, with the exception of VE4, whose maximum shear strain value is found a point towards the rear of the brain.

Table 4.6 Absolute Maximum Shear Strain for Examined Cases

15 mph	*VE*	*EA*	*7.5 mph*	*VE*	*EA*
1	2.76×10^{-1}	2.76×10^{-1}		1.53×10^{-1}	1.53×10^{-1}
2	2.25×10^{-1}	2.24×10^{-1}		1.33×10^{-1}	1.32×10^{-1}
3	2.75×10^{-1}	2.75×10^{-1}		1.53×10^{-1}	1.53×10^{-1}
4	3.05×10^{-1}*	3.02×10^{-1}*		1.53×10^{-1}	1.53×10^{-1}
5	2.71×10^{-1}	2.71×10^{-1}		1.51×10^{-1}	1.51×10^{-1}

* Different location

The bulk modulus, which is lower for VE2 than others, does make a significant difference in failure rates as shown in Table 4.7.

Table 4.7 Failure Percentages for VEA with Varying Bulk Modulus

Parameters changed	*Failure (%)*
VEA	14.4
Bulk Modulus x 0.1	72.8
Bulk Modulus x 0.01	96.0

As the bulk modulus is lowered, there is a drastic increase in failure rates. However, VE2, whose shear short term modulus is considerably higher than those of others, does not appear to be affected by its lower-than-others bulk modulus. In other words, while the choice of bulk modulus makes a difference in failure rates, it appears that the shear characteristics play a larger role, even though absolute numbers do not reflect it (see Table 4.8). As it can be seen, in general the failure rate follows the same trend; the stiffer the material, the less failure occurs. The decay constant is a measure of how quickly the material shifts from the short term modulus to long term modulus (see the relaxation curve in Chapter 2). A higher decay constant indicates that the material reaches its long term modulus more quickly, therefore it is effectively “softer.”

Table 4.8 Failure Percentages for VEA with Varying Short Term and Short/Long Term Moduli

Parameters changed	*Failure (%)*
VEA	14.4
Decay constant x 10	17.0
Decay constant x 100	21.8
Short term modulus x 10	3.07
Short term modulus x 100	0.47
Short term/long term moduli x 10	3.08
Short term/long term moduli x 100	0.47

Even though this model is not intended to produce realistic HIC to make assessment on head injuries, it is possible to examine the consequence of measuring HIC at different locations on the head. Table 4.9 shows the HIC values calculated from the acceleration histories measured at points on the sides of the head, at the lateral projections of the head CG. As it was done by Nahum and Smith [56], only the acceleration histories in the sagittal plane (Y-Z plane in this case) are taken at those two points thus selected. The Y accelerations from those locations are averaged, and the same is done to the Z acceleration histories. These two averaged acceleration histories are used to determine the resultant acceleration history of the head, and to calculate HIC.

Table 4.9 HIC from Examined Cases, at Side of Head

15 mph	*HIC from VE*	*HIC from EA*	*7.5 mph*	*HIC from VE*	*HIC from EA*
1	2045.5	2045.5		219.8	219.8
2	1657.5	1657.7		180.1	180.1
3	2045.9	2045.9		219.9	219.9
4	2045.5	2045.4		219.8	219.8
5	2046.8	2046.8		219.6	219.6

Those values show a significant reduction (roughly 47%) in HIC from those measured at the head CG. Contrary to the HIC measured at the head CG, VE2 produces a lower HIC value than the others, owing to its low bulk modulus (see Table 4.10), while the HICs from the rest of the viscoelastic models are nearly identical, falling within less than 0.1% of each other.

Table 4.10 HIC Under Varying Bulk Modulus, at Side of Head

Parameters changed	*HIC*
VEA	2045.9
Bulk Modulus x 0.1	1712.6
Bulk Modulus x 0.01	1782.5

The difference between these HIC values at the sides of the head and those from the head CG are not simply a matter of locations. Table 4.10 shows the results of the parametric studies using VEA to demonstrate that the internal (brain) constitutive models influence HIC values. Similarly to the HIC measured at the head CG, the bulk modulus of the brain has a noticeable effect on HIC, but in the opposite direction, as it decreases by nearly 16% as the brain bulk modulus is decreased by 10. The correlation appears to be non-linear, as it shows a slight increase when the bulk modulus is reduced by 100. Resembling the HIC at the head CG, the effect is more subtle (up to 2.3%) when the brain deviatoric parameters are varied (Table 4.11).

Table 4.11 HIC Under Varying Short Term Modulus, at Side of Head

Parameters changed	*HIC*
VEA	2045.9
Short Term Modulus x 10	2050.3
Short Term Modulus x 100	2092.0

This poses a question as to how HIC should be measured and treated. As mentioned earlier, occupant safety in a passenger vehicle is assessed by HIC measured at the CG of a dummy's head. If the biofidelity of the dummy's head is sound, this HIC value should be the same as the one that would be measured at the CG of a real human head. However, physical experiments using cadavers, which can be used to validate mathematical models and mechanical surrogates, often measure acceleration history on the skull, at the lateral projection of the head CG. As suggested by this model, HIC values are different depending on where they are measured, and although it may be unrealistic to change the bulk modulus

of the brain, this series of simulations shows that the difference in internal material constitutive models indeed affect not only the HIC measured at the head CG, but also that measured at the outside of the head.

One exercise is intentionally omitted in this study; a validation of this model is not performed. The reason for this omission is that this study deals with the comparison of yet unknown aspect of the finite element model of a human brain—namely the constitutive characteristics. There have been studies where "validations" of finite element models were made [8, 56, 70] against cadaver experiments performed by Nahum et al. [57]. However, without conclusive evidence of the accuracy and truthfulness of the brain rheological characterization, and the lack of certain information in Nahum et al.'s experiments such as the type and thickness of padding used between the cadaver heads and the impactor, it is doubtful that any level of validation can be performed satisfactorily.

Therefore, the model is only certified to be as "accurate" as the geometry and available material models allow it to be. It must be noted that the model used in this study lacks many features that have been suggested to play large roles in affecting dynamics of the brain under impact or impulsive loading—such as the falx and tentorium. Without those features the model is expected to exhibit different dynamic characteristics from those observed in a real head. However, the purpose of this model is not to predict actual head injury potential, type or severity. Rather, it is being employed to assess the effects of material model selection on certain parameters used as indicators for head injury, such as HIC, shear strain and pressure.

Chapter 5
Conclusions and Recommendations

5.1 Conclusions

In this study the effects of brain material constitutive relations on head injury criteria are analyzed. The brain tissue is generally considered viscoelastic, even though many finite element models in the literature employ simple linear elastic models for the brain. Therefore, in order to clarify those models, a review on viscoelasticity is conducted first. A three-parameter viscoelastic solid model in the transient dynamics finite element code, DYNA3D, is validated against the theoretical derivations in terms of stress wave propagation.

Next, a simple spherical model simulating a human head is analyzed to examine the adequacy of linear elastic models and differences in viscoelastic models for the brain. From this phase of the study, it is concluded that different viscoelastic models do produce different results in the shear response, and a certain linear elastic model can be substituted for a three-parameter viscoelastic solid model under specific conditions: the Young's modulus of such a model must be equal to the short term modulus of the three-parameter viscoelastic solid model, and shear strain rate is high enough in the scenario under consideration.

Finally, a slightly more realistic head model in terms of geometry is examined to scrutinize head injury criteria. Five viscoelastic models found in the literature, four of which are based on published experiments, are studied. The finding in the previous phase, which suggests a possibility of replacing a three-parameter viscoelastic model with a linear elastic one, is proven to be inapplicable for viscoelastic brain models with high decay constants.

The most revealing finding in this second phase of the study is that regardless of the material constitutive relations used for the brain, HIC is shown to be insusceptible. HIC is found to be

sensitive to the change in bulk modulus of the brain, with a lower bulk modulus producing higher HIC. A further comment on this phenomenon is made later.

As expected, different viscoelastic brain models produce different shear outcomes, even though HIC values are nearly identical for all models. They are different not only in absolute magnitudes at peaks, but also in general patterns; some models continue to be loaded when others start to be unloaded. The short term moduli of the viscoelastic models have a strong effect on the shear response, with “stiffer” models producing less strain and “softer” models, more strain. It is also found that, though a parametric study, the bulk modulus of the brain has a noticeable influence on the shear response as well.

Instead of focusing on particular locations in the brain, the entire brain is examined with an arbitrary shear strain value as a threshold for injury. When such a threshold is assigned and it is assumed that any elements that exceed that value are deemed “failed,” the percentages of “failed” elements also differ greatly from model to model.

Pressure responses, as discovered in the previous phase with the spherical model, are dominated by the bulk modulus of the brain. It is shown by a parametric study that lower bulk modulus produces lower peak pressure values at both coup and contracoup sites.

As seen above, the bulk modulus of the brain has a profound effect on pressure, HIC and even shear strain responses. However, modifying the bulk modulus of the brain appears to contradict with a widely-accepted notion that the brain is just as incompressible as water. It is recommended that such a change should only be done to accommodate internal structures such as the ventricles which make the brain as a whole appear compressible. Therefore, depending of the degree of simplification of the finite element model, any response sensitivity, including the coup and contracoup pressure, to this property may simply be theoretical.

Another finding regarding HIC is that hypothetical HIC values taken at different locations, namely the center of gravity of the head and lateral projection of the center of gravity at the side of the head, are different. The former location is normally used for dummies and mathematical models, and the latter, for physical surrogates such as cadavers. Their effect is undoubtedly caused by the differences in their physical locations, but it is shown that even the internal constitutive properties, particularly the bulk modulus of the brain, have effects on

their values. Even though, once again, alteration of the bulk modulus of the brain may be fictitious, it still has a place in finite element analysis when simple head models are called for. In such cases, its consequences should not be ignored altogether.

In short, if the bulk modulus of the brain is kept constant and different shear characteristics are assigned, shear responses in the brain are dramatically affected while HIC values calculated from those models are nearly identical. This appears to indicate that HIC may not be strongly correlated to the shear strain injury theory. As the bulk modulus of the brain is reduced in a parametric study, HIC is increased while the pressure peaks at coup and contracoup are decreased; thus suggesting that HIC is not a good indicator of the pressure theory, either.

This exposes the limitation of HIC as a general criterion for head injuries: it does not account for the internal dynamics of the brain. In order to compensate for this deficiency, analysis methods such as the finite element method must be used to gain better insights of the dynamic events that take place within the brain.

5.2 Recommendations

The three-parameter viscoelastic solids examined in this study are derived from experiments that span a wide range of strain rates, from a near-static experiments [19] to a relatively high-rate experiments [11]. There is a good reason to believe that each of those models is correct in its own domain, and probably only applicable in that particular realm of experiments from which it is derived. A natural tendency is to assume that models derived from experiments performed at higher strain rates are more suitable for analyses like the ones conducted in this study, but it is obvious that more experiments are needed in order to gain confidence.

The arithmetic average of those viscoelastic models introduced in the previous Chapter is probably purely academic, and it is definitely not recommended to be used as the brain tissue model for real simulations. The true brain tissue’s rheological behavior is most likely to resemble a relaxation spectrum chart shown in Fung [17]. This chart indicates that there are multiple peaks in an internal friction versus frequency plot for a metal, instead of one in the

case for a three-parameter viscoelastic solid. Those multiple peaks correspond to internal friction associated with internal structures of various scales. If brain tissue is assumed to exhibit such characteristics, it may be represented by a chart shown in Figure 5.1.

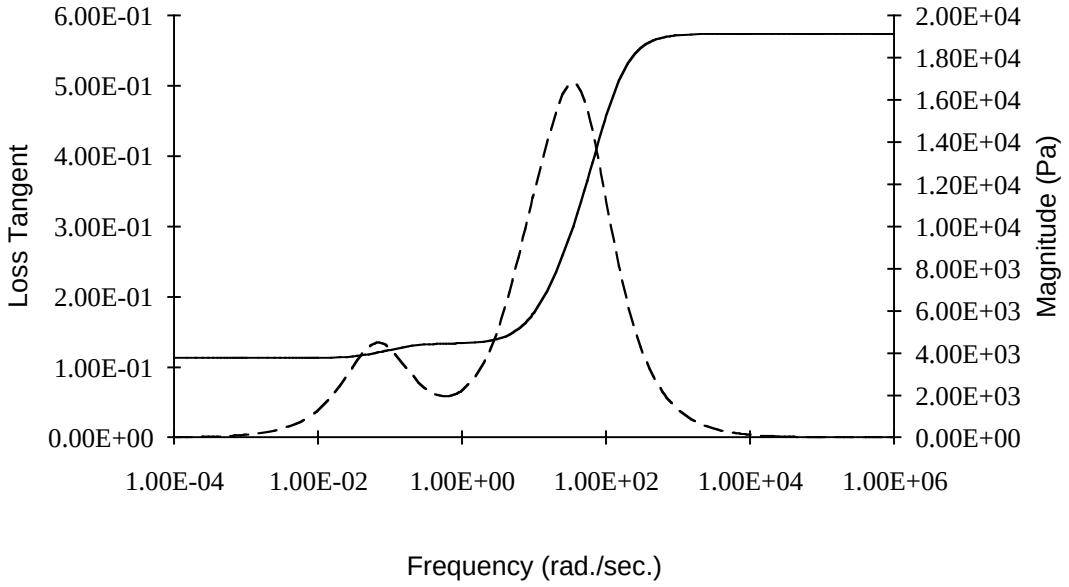

Figure 5.1 Superposition of Viscoelastic Models, Internal Friction and Magnitude of Complex Modulus Versus Frequency

This figure is generated by taking arithmetic averages of loss tangents and magnitudes of complex moduli from four of the viscoelastic models which have actual experimental basis. Two peaks of internal friction that are supposed to be present between 10 and 100 rad./sec. are overshadowed by one large peak due to VE5, but it is clear that this curve has a similar characteristic to the one seen in Fung's book. The magnitude of complex modulus also goes through a transformation and now has multiple transition stages, instead of one for the case of a three-parameter viscoelastic solid. In the Figure above, the first transition, albeit slight, is seen around 0.1 rad./sec. followed by a large shift in magnitude around 10 rad./sec. If the brain tissue is indeed such a material, those peaks should correspond to internal structures of various scales such as cells, groups of cells or tissues. Mathematically, a material that produces such characteristics can be constructed by a combination of three-parameter viscoelastic solids, and perhaps it is more appropriate for the brain tissue than a single linear three-parameter viscoelastic solid. It is suggested that such a material model for the brain be constructed.

Even though this study is mainly focused on the material constitutive relation of the brain tissue, the geometry of the model is still expected to play a large role in influencing the dynamics responses of the head. This model lacks such internal structures as the falx and tentorium, which may exaggerate the internal movement of the head thus affecting the discrepancy between HIC values measured at the center of gravity or even the side of the head. It is desirable that, in conjunction with research on brain material characterization, more effort should be placed in this area as well.

Finally, the limitation of HIC as a head injury indicator should be made clear. First, it is suggested that the measuring methods of HIC be reviewed. This study shows that there are differences between HIC values measured at the center of gravity of the head and its side. The former location is used for a dummy and (frequently) mathematical models such as finite element models, and the latter, even though it is hypothetical, for other physical surrogates such as cadavers. The Federal Motor Vehicle Safety Standard 208 only specifies HIC measured from the Hybrid III dummy, a protocol must be established when other types of surrogates, either physical or mathematical, are used. Once such a protocol is instituted, then a more objective comparison among all those types of subjects (dummies, cadavers and mathematical models of both), and a more thorough examination of HIC and its relevance to other injury criteria can be performed.

In addition, it is suggested that HIC is limited in terms of representing the internal dynamics of the head. The finite element method can provide the information on dynamic events within the brain since it appears that it is the only viable technique that is readily available and capable in doing so. However, once again, firm knowledge the brain properties is crucial in analyzing the engineering parameters that constitute various head injury criteria including HIC.

When these recommendations are implemented, they eventually can lead to an improved HIC or entirely new and better head injury criteria which are then used to design safer passenger vehicles and protection devices.

Bibliography

1 Adams, J. H., D. Doyle, D. I. Graham, A. E. Lawrence and D. R. McLellan, "Gliding Contusions in Nonmissile Head Injury in Humans," *Archives of Pathology & Laboratory Medicine*, **110**, pp. 485–488, 1986.

2 Arbogast, Kristy B. and Susan S. Margulies, "Material Characterization of the Brainstem from Oscillatory Shear Tests," *Journal of Biomechanics*, **31**, pp. 801–807, 1998.

3 Barber, Ted W., Judith A. Brockway and Lawrence S. Higgens, "The Density of Tissues in and About the Head," *Acta Neurolologica Scandinavica*, **46**, pp. 85–92, 1970.

4 Bilston, Lynne E. and Lawrence E. Thibault, "The Mechanical Properties of the Human Cervical Spinal Cord *In Vitro*," *Annals of Biomedical Engineering*, **24**, pp. 67–74, 1996.

5 Bilston, Lynne E., Zizhen Liu and Nhan Phan-Thien, "Linear Viscoealstic Properties of Bovine Brain Tissue in Shear," *Biorheology*, **34** (6), pp. 377–385, 1997.

6 Biomechanics Laboratories of the Department of Theoretical and Applied Mechanics, College of Engineering, West Virginia University, *Determination of the Physical Properties of Tissues of the Human Head: Final Report*, Morgantown, West Virginia, 1970.

7 Chan, Han Sun and Y. King Liu, "The Asymmetric Response of A Fluid-Filled Spherical Shell—A Mathematical Simulation of A Glancing Blow to the Head," *Journal of Biomechanics*, **7**, pp. 43–59, 1974.

8 Chu, Chung-Sheng, Mish-Shayan Lin, Haw-Ming Huang and Maw-Chang Lee, "Finite Element Analysis of Cerebral Contusion," *Journal of Biomechanics*, **27** (2), pp. 187–194, 1994.

9 Dawson, Stuart L., Charles S. Hirsch, Fred V. Lucas and Bruce A. Sebek, "The Contrecoup Phenomenon: Reappraisal of a Classic Problem," *Human Pathology*, **11** (2), pp. 155–166, 1980.

10 Denny-Brown, D. and W. Ritchie Russell, "Experimental Cerebral Concussion," *Brain*, **64**, pp. 95–164, 1941.

11 Donnely, B. R. and J. Medige, "Shear Properties of Human Brain Tissue," *Journal of Biomechanical Engineering—Transaction of the ASME*, **119**, pp. 423–432, 1997.

12 Duck, Francis A., *Physical Properties of Tissue: A Comprehensive Reference Book*, Academic Press, London, 1990.

13 Engin, Ali E., "The Axisymmetric Response of A Fluid-Filled Spherical Shell to A Local Radial Impulse—A Model for Head Injury," *Journal of Biomechanics*, **2**, pp. 325–341, 1969.

14 Estes, Michael Summer, *Mechanical Response of Brain in Free Standing Compression*, Master's Thesis, West Virginia University, Morgantown WV, 1969.

15 Flügge, Wilhelm, *Viscoelasticity*, Blaisdell Publishing Company, Waltham, Massachusetts, 1967.

16 Fung, Y. C., "Stress-Strain-History Relations of Soft Tissues in Simple Elongation," Y. C. Fung, N. Perrone and M. Anliker (ed.), *Biomechanics: Its Foundations and Objectives*, pp. 181–208, Prentice-Hall, Englewood Cliffs, NJ, 1972.

17 Fung, Y. C., *Biomechanics: Mechanical Properties of Living Tissues*, Springer-Verlag, New York, 1981.

18 Fung, Y. C., *Biomechanics: Motion, Flow, Stress, and Growth*, Springer-Verlag, New York, 1990.

19 Galford, James E. and James H. McElhaney, "A Viscoelastic Study of Scalp, Brain, and Dura," *Journal of Biomechanics*, **3**, pp. 211–221, 1970.

20 Gennarelli, Thomas A., “Mechanistic Approach to the Head Injuries: Clinical and Experimental Studies of the Important Types of Injury,” Ommaya, A. K. (ed.), *Head Injury Criteria: A Consensus Workshop*, U. S. Department of Transportation, National Highway Traffic Safety Administration, Washington D. C., 1981.

21 Gennarelli, Thomas A., “Head Injury Mechanism,” Joseph S. Torg (ed.), *Athletic Injuries to the Head, Neck and Face*, pp. 65–72, Lea & Febiger, Philadelphia, PA, 1982.

22 Gennarelli, Thomas A. and Lawrence E. Thibault, “Biomechanics of Acute Subdural Hematoma,” *Journal of Trauma*, **22** (8), pp. 680–686, 1982.

23 Goldsmith, Werner, “Biomechanics of Head Injuries,” Y. C. Fung, N. Perrone and M. Anliker (ed.), *Biomechanics: Its Foundations and Objectives*, pp. 585–634, Prentice-Hall, Englewood Cliffs, NJ, 1972.

24 Goldsmith, Werner and Ayub K. Ommaya, “Head and Neck Injury Criteria and Tolerance Level,” B. Aldman and A. Chapon (ed.), *The Biomechanics of Impact Trauma*, pp. 149–187, Elsevier Science Publishers B.V., Amsterdam, 1984.

25 Gray, Henry, *Gray’s Anatomy (30th American Edition)*, Carmine D. Clemente (ed.), Lea & Febiger, Philadelphia, 1985.

26 Gross, G. Arthur, “A New Theory on the Dynamics of Brain Concussion and Brain Injury,” *Journal of Neurosurgery*, **15**, pp. 548–561, 1958.

27 Gurdjian, E. S. and H. R. Lissner, “Photoelastic Confirmation of the Presence of Shear Strains at the Craniospinal Junction in Closed Head Injury,” *Journal of Neurosurgery*, **18**, pp. 58–60, 1961.

28 Gurdjian, E. S., J. E. Webster and H. R. Lissner, “Observations on the Mechanism of Brain Concussion, Contusion and Laceration,” *Surgery Gynecology & Obstetrics*, **101**, pp. 680–690, 1955.

29 Gurdjian, E. S., H. R. Lissner, F. G. Evans, L. M. Patrick and W. G. Hardy, “Intracranial Pressure and Acceleration Accompanying Head Impacts in Human Cadavers,” *Surgery, Gynecology & Obstetrics*, **107**, pp. 185–190, 1961.

30 Guyton, Arthor C., *Textbook of Medical Physiology (Eighth Edition)*, W. B. Saunders Company, Philadelphia, 1991.

31 Hardy, Warren N., Tawfik B. Khalil and Albert I. King, "Literature Review of Head-Injury Biomechanics," *International Journal of Impact Engineering*, **15** (4), pp. 561–586, 1994.

32 Hess, Robert L., Kathleen Weber and John M. Melvin, "A Review on Head Impact and Injury Criteria Related to Occupant Protection," National Highway Traffic Safety Administration, *Head & Neck Injury Criteria: A Consensus Workshop*, pp. 183–194, Washington D.C., 1981.

33 Holbourn, A. H. S., "Mechanics of Head Injuries," *Lancet*, **245**, pp. 438–441, 1943.

34 Hosey, Ronald R. and Y. King Liu, "A Homeomorphic Finite Element Model of the Human Head and Neck," R. H. Gallagher, B. R. Simon, P. C. Johnson, J. F. Gross (ed.), *Finite Elements in Biomechanics*, pp. 379–401, John Wiley & Sons, Chichster (West Sussex), NY, 1982.

35 Hunter, S. C., "Viscoelastic Waves," I. N. Sneddon and R. Hill (ed.), *Progress in Solid Mechanics: Volume 1*, pp. 1–57, North-Holland Publishing Company, Amsterdam, 1960.

36 Kenner, V. H. and W. Goldsmith, "Dynamics Loading of a Fluid-Filled Spherical Shell," *International Journal of Mechanical Sciences*, **14**, pp. 557–568, 1972.

37 Key, Samuel W. and Raymond D. Krieg, "On the Numerical Implementation of Inelastic Time Dependent and Time Independent, Finite Strain Constitutive Equations in Structural Mechanics," *Computer Methods in Applied Mechanics and Engineering*, **33**, pp. 439–452, 1982.

38 Khalil, T. B., W. Goldsmith and J. L. Sackman, "Impact on a Model Head-Helmet System," *International Journal of Mechanical Science*, **16**, pp. 609–625, 1974.

39 Khalil, Tawfik B. and Robert P. Hubbard, "Parametric Study of Head Response by Finite Element Modeling," *Journal of Biomechanics*, **10**, pp. 119–132, 1977.

40 Khalil, Tawfik B. and David C. Viano, “Critical Issues in Finite Element Modeling of Human Head Impact,” SAE Paper Number 821150, 1982.

41 King, A. I. and C. C. Chou, “Mathematical Modeling Simulation and Experimental Testing of Biomechanical System Crash Response,” *Journal of Biomechanics*, **9**, pp. 301–317, 1976.

42 Kolsky, H., *Stress Waves in Solids*, Dover Publications, New York, 1963.

43 Kopecky, J. A. and E. A. Ripperger, “Closed Brain Injuries: An Engineering Analysis,” *Journal of Biomechanics*, **2**, pp. 29–34, 1969.

44 Lee, Maw-Chang, John W. Melvin and Kazunari Ueno, “Finite Element Analysis of Traumatic Subdural Hematoma,” SAE Paper Number 872201, 1987.

45 Lindburg, Richard and Ella Freytag, “The Mechanism of Cerebral Contusions,” *Archives of Pathology*, **69**, pp. 440–469, 1960.

46 Margulies, S. S. and L. E. Thibault, “An Analytical Model of Traumatic Diffuse Brain Injury,” *Journal of Biomechanics—Transaction of the ASME*, **111**, pp. 241–249, 1989.

47 Margulies, Susan Sheps and Lawrence E. Thibault, “A Proposed Tolerance Criterion for Diffuse Axonal Injury in Man,” *Journal of Biomechanics*, **25** (8), pp. 917–923, 1992.

48 Margulies, Susan Sheps, Lawrence E. Thibault and Thomas A. Gennarelli, “Physical Model Simulation of Brain Injury in the Primate,” *Journal of Biomechanics*, **23** (8), pp. 823–836, 1990.

49 McElhaney, James H., John L. Fogle, John W. Melvin, Russel R. Haynes, Verne L. Roberts and Nabih M. Alem, “Mechanical Properties of Cranial Bone,” *Journal of Biomechanics*, **3**, pp. 495–511, 1970.

50 McElhaney, James H., John Melvin, Verne L. Roberts and Harold D. Portnoy, “Dynamic Characteristics of the Tissues of the Head,” R. M. Kenedi (ed.), *Perspectives in Biomedical Engineering*, pp. 215–222, University Park Press, Baltimore, 1973.

51 Melvin, John W., James W. Lighthall and Kazunari Ueno, “Brain Injury Biomechanics,” Robert S. Levine (ed.), *Head and Neck Injury,* Special Publication P-276, Society of Automotive Engineers, Inc., 1994.

52 Mendis, K. K., R. L. Stalnaker and S. H. Advani, “A Constitutive Relationship for Large Deformation Finite Element Modeling of Brain Tissue,” *Journal of Biomechanical Engineering—Transaction of the ASME*, **117**, pp. 279–285, 1995.

53 Mertz, H. J., P. Prasad and G. Nusholtz, “Head Injury Risk Assessment For Forehead Impacts,” SAE Paper Number 960099, 1996.

54 Miller, Karol and Kiyoyuki Chinzei, “Constitutive Modelling of Brain Tissue: Experiment and Theory,” *Journal of Biomechanics*, **30**, pp 1115–1121, 1997.

55 Motor Vehicle Safety Systems Testing Committee, Society of Automotive Engineers, *Human Tolerance to Impact Conditions as Related to Motor Vehicle Design—SAE J885 APR80*, Society of Automotive Engineers, Inc., Warrendale, PA, Apr. 1980.

56 Nahum, Alan M. and Randall W. Smith, “An Experimental Model for Closed Head Impact Injury,” SAE Paper Number 760825, 1976.

57 Nahum, Alan M., Randall Smith and Carley C. Ward, “Intracranial Pressure Dynamics During Head Impact,” SAE Paper Number 770922, 1977.

58 Netter, H. Frank, *The CIBA Collection of Medical Illustrations Volume 1: Nervous System*, CIBA Pharmaceutical Company, Summit, NJ 1974.

59 Netter, H. Frank, *The CIBA Collection of Medical Illustrations Volume 1: Nervous System Part II: Neurologic and Neuromuscular Disorders*, CIBA Pharmaceutical Company, Summit, NJ 1986.

60 Nusholtz, Guy S. and Yibing Shi, “Physical Reality in FE Models: Rotation and Strain,” SAE Paper Number 980355, 1998.

61 Office of the Federal Register, National Archives and Records Administration, The Code of Federal Regulations, Title 49, Subtitle B, Chapter V, Part 571, Subpart B, Section 571.208.

62 Office of the Federal Register, National Archives and Records Administration, The Code of Federal Regulations, Title 49, Subtitle B, Chapter V, Part 571, Subpart B, Section 571.216.

63 Ommaya, Ayub K. and T. A. Gennarelli, "Cerebral Concussion and Traumatic Unconsciousness," *Brain*, **97**, pp. 633–654, 1974.

64 Ommaya, A. K., "Biomechanics of Head Injury: Experimental Aspects," A. M. Nahum and J. W. Melvin (ed.), *The Biomechanics of Trauma*, pp. 245–279, Appleton-Century-Crofts, Norwalk, CT. 1985.

65 Ommaya, Ayub K., Lawrence Thibault and Faris A. Bandak, "Mechanisms of Impact Head Injury," *International Journal of Impact Engineering*, **15** (4), pp. 535–560, 1994.

66 Pamidi, M. R. and S. H. Advani, "Nonlinear Constitutive Relations for Human Brain Tissue," *Journal of Biomechanical Engineering—Transaction of the ASME*, **100**, pp. 44–48, 1978.

67 Phen, R. L., M. W. Dowdy, D. H. Ebbeler, E-H. Kim, N. R. Moore and T. R. VanZandt, *Advanced Air Bag Technology Assessment: Final Report*, Jet Propulsion Laboratory and California Institute of Technology, April 1998.

68 Prasad, Priya and Harold J. Mertz, "The Position of the United States Delegation to the ISO Working Group 6 on the Use of HIC in the Automotive Environment," SAE Paper Number 851246, 1985.

69 Ruan, J. S., Khalil, T. and A. I. King, "Human Head Dynamic Response to Side Impact by Finite Element Modeling" *Journal of Biomechanical Engineering—Transaction of the ASME*, **113**, pp. 276–283, 1991.

70 Ruan, J. S., T. Khalil and A. I. King, "Finite Element Modeling of Direct Head Impact," SAE Paper Number 933114, 1993.

71 Ruan, J. S., T. Khalil and A. I. King, "On the Impact of a 3-D Viscoelastic Human Head Model," *1993 Bioengineering Conference—ASME*, pp. 530–533, 1993.

72 Ruan, J. S., T. Khalil and A. I. King, "Dynamics Response of the Human Head to Impact by Three-Dimensional Finite Element Analysis," *Journal of Biomechanical Engineering—Transaction of the ASME*, **116**, pp. 44–50, 1994.

73 Sahay, K. B., R. Mehrotra, U. Sachdeva and A. K. Banerji, "Elastomechanical Characterization of Brain Tissue," *Journal of Biomechanics*, **25** (3), pp. 319–326, 1992.

74 Shigley, Joseph Edward and Charles R. Mischke, *Mechanical Engineering Design (Fifth Edition)*, McGraw-Hill, New York, 1989.

75 Shuck, L. Z., *Determination of the Dynamic Shear Modulus of Human Brain Tissue*, Ph.D. Dissertation, West Virginia University, Morgantown WV, 1970.

76 Shuck, L. Z. and S. H. Advani, "Rheological Response of Human Brain Tissue in Shear," *Journal of Basic Engineering—Transaction of the ASME*, pp. 905–911, Dec. 1972.

77 Shugar, Theodore A. and Michael G. Katona, "Development of Finite Element Head Injury Model," *Journal of ASCE*, **101**, pp. 223–239, 1975.

78 Shugar, T. A., "A Finite Element Head Injury Model," Final Report, DOT HS 289-3-550-IA, 1977.

79 Spitzer, Victor, Michael J. Ackerman, Ann L. Scherzinger and David Whitlock, "The Visible Human Male: A Technical Report," *Journal of the American Medical Informatics Association*, **3** (2), pp. 118–130, 1996.

80 Spraycar, Majory (ed.), *Stedman's Medical Dictionary: 26th edition*, Williams & Wilkins, Baltimore, 1995.

81 Stalnaker, Richard L., John L. Fogle and James H. McElhaney, "Driving Point Impedance Characteristics of the Head," *Journal of Biomechanics*, **4** pp. 127–139, 1971.

82 Talhouni, O. and F. DiMaggio, "Dynamic Response of a Fluid-Filled Spheroidal Shell—An Improved Model for Studying Head Injury," *Journal of Biomechanics*, **8**, pp. 219–228, 1975.

83 Thibault, Kirk L. and Susan S. Margulies, “Age-Dependent Material Properties of the Porcine Cerebrum: Effect on Pediatric Inertial Head Injury Criteria,” *Journal of Biomechanics,* **31**, pp. 1119–1126, 1998.

84 Timoshenko, S. P. and J. N. Goodier, *Theory of Elasticity,* McGraw-Hill, New York, 1934.

85 Viano, David C., Albert I. King, John W. Melvin and Kathleen Weber, “Injury Biomechanics Research: An Essential Element in the Prevention of Trauma,” *Journal of Biomechanics,* **22**, (5), pp. 403–417, 1989.

86 Walker, L. B., E. H. Harris and U. R. Pontius, “Mass, Volume, Centre of Mass, and Mass Moment of Inertia of Head and Neck of the Human Body,” *Proceedings of Seventeenth Annual Stapp Car Crash Conference,* 1973.

87 Ward, Carley, Marian Chan and Alan Nahum, “Intracranial Pressure—A Brain Injury Criterion,” SAE Paper Number 801304, 1980.

88 Ward, Carley Conrad and Robert B. Thompson, “The Development of A Detailed Finite Element Brain Model,” SAE Paper Number 751163, 1975.

Appendix
VHD to I-DEAS Model

The images in the dataset were generated by placing the body in a mold into which a blue-colored gelatin solution was injected and frozen to provide a supporting medium during the cryomacrotome procedure. Cryomacrotoming is a system developed at the University of Colorado Medical School, which is designed to mill the surface of a frozen specimen at a precisely controlled increment. This system was capable of milling a frozen specimen containing tissues at a 0.1 mm increment. For the Visible Human Male an increment of 1 mm was selected. After each slice the newly-exposed surface was cleaned and retouched, and digital and film images were captured. The resulting digital images were 2048 by 1216 pixels (lateral and anterior-posterior directions, respectively) in 24-bit color. Each pixel corresponds to 0.33 mm in the transverse plane, and each image is separated by the milling increment of 1 mm in the axial direction.

With a formal agreement with the National Library of Medicine, the images corresponding to the head/neck region (approximately 230 images) are obtained.

The images are processed using Adobe Photoshop®, which can convert the raw image format used in the original VHD images into its native graphics format. Since none of the software packages available can distinguish different anatomical components without being overwhelmed by details in the images, it is decided to trace the contours of major anatomical components manually by erasing parts of the images, thus establishing clear boundaries between various components.

Care is taken to ensure that the erased parts have no relevant internal structure (for example, sinus cavities), and that no two juxtaposed components are erased unless they can be considered one component. Some components, such as the subarachnoidal space, are artificially enhanced by erasing or leaving slightly more area than what they appear to occupy on the images. Specifically, the subarachnoidal space which surrounds the brain, is

erased but the thinnest portions are expanded to at least 2 pixels wide even though they do not appear clearly on the images (the brain appeared firmly pressed against the interior surface of the cranium). Other sources such as CT scan images are referred to when certain boundaries are not clear on the cross sectional images.

The converted images are traced using Adobe Streamline®, which scans bit-mapped images such as ones produced by Photoshop, detects contours at a specified tolerance in terms of colors and/or gray levels (darkness) and size (it can ignore features of certain size) and generates vector images for Adobe Illustrator® where editing and final touching of contour lines is performed. Photoshop images used to trace contours of anatomical components are used as templates for adjustments. Using the templates vector lines and curves are edited to faithfully represent the outlines of the anatomical components.

Completed vector images are imported into another graphics application Canvas from Deneva, whose sole purpose here is to convert the vector images into IGES format. The IGES (Initial Graphics Exchange Standard) is a file format developed for the interchange of two-dimensional and three-dimensional drawings, widely used in various computer-aided design programs.

Finally, those IGES files are imported into I-DEAS from Structural Dynamics Research Corporation, a general-purpose computer-aided design software for three-dimensional model and finite element mesh generation. After the files are read in, the alignment markers are used to adjust the locations of the each cross section. After numerous image conversions, the size of the alignment marker turns out to be 2.96 mm by 2.96 mm, which is approximately 10 % smaller than the original. However, it is decided to make a final judgment as to whether or not the model should be scaled when the final volumetric and finite element models are created.

From those cross sectional images, now represented as collections of curves in I-DEAS, five major volumes are generated. Those are: Soft Tissues (exterior boundary of soft tissues), Outer Skull (exterior boundary of the skull), Inner Skull (any interior cavities, including the cranial cavity, in the skull), Brain (exterior boundary of the brain) and Brain Cavities (mainly the ventricles).

Vita

Toru Aida

Toru Aida was born in Tokyo, Japan on July 9, 1968. He graduated from Kunitachi High School in Tokyo in March 1987. In September 1987 he entered West Virginia University and graduated *cum laude* with the Bachelor of Science in Mechanical Engineering (B.S.M.E.) degree in May 1991. He subsequently received the Master of Science in Mechanical Engineering (M.S.M.E.) from the same institution in August of 1993. In January of 1996 he started working as a Graduate Research Assistant at Los Alamos National Laboratory, New Mexico, and is currently a candidate for the Doctor of Philosophy degree in Mechanical Engineering at West Virginia University.